UNIVERSITÉ DE FRIBOURG
UNIVERSITÄT FREIBURG

Simulation of Abramov glacier energy balance and firn properties

Master Thesis

by

Warren Dering Stainbank

Supervised by Dr. Horst Machguth
Co-supervised by Marlene Kronenberg

Submitted: December 2018

Department of Geosciences, Geography.

University of Fribourg

Abstract

It is predicted that the majority of glaciers world-wide will continue to experience mass loss. This can have dire consequences for regions (e.g. Central Asia) that rely heavily on meltwater from snow and glaciers for agriculture, energy, and domestic consumption. Thus, mass balance studies are important for studying the relationship between glaciers and climate; yet need to account for both surface and subsurface processes to be accurate. This study reports for the first time a coupled distributed energy balance and snow model for Abramov glacier, Kyrgyzstan for the period 2013-2017. Such models are imperative as they add to our understanding of the potential responses of glaciers in the context of global warming trends.

In order to run the model, input variables were acquired from various sources; including automatic weather station data, modelled and ERA-Interim reanalysis data. Calibration was accomplished using literature and *in-situ* measurements from ablation stakes for 2014-2017. Furthermore, the reliability and accuracy of the modelled outputs was assessed through comparison with ice core data and literature.

The model simulated a positive mass balance (+0.94 m w.e. a^{-1}) in contradiction to previous study estimates. This discrepancy was mainly attributed to spatial and temporal differences in precipitation events. By better representing and accounting for this variability in the initial input and calibration could result in a more realistic modelled output. However, as the overall mass balance relied on both surface (i.e. energy balance) and subsurface models each were assessed individually to identify parameters adding further inaccuracies into the coupled model output. Relative humidity and cloud cover were identified as the most problematic parameters within the energy budget. Whereas, the main issue identified with the subsurface model was its inability to simulate densification with depth.

Notwithstanding the identified shortfalls, the coupled model still has significant potential. Through slight modification it is foreseen that problematic areas can be overcome and it successfully applied in the future to model surface and subsurface processes of Abramov glacier.

Declaration

I declare that this thesis was composed by myself, that the work contained herein is my own except where explicitly stated otherwise in the text, and that this work has not been submitted for any other degree or processional qualification except as specified.

Signed:

…….

Warren Dering Stainbank

Date:

Contents

Abstract ii

Declaration iii

Acknowledgements vi

List of figures vii

List of tables viii

Chapter 1 Introduction 1

1.1 Context of study 1

1.2 Aims and objectives 2

1.3 Structure of thesis 2

Chapter 2 Glacier mass and energy balance 3

2.1 Introduction 3

2.2 Transformation of snow to ice 5

2.3 Glacier zones and stratigraphy 6

2.4 Surface mass balance 7

2.4.1 Surface accumulation processes 8

2.4.2 Surface ablation processes 9

2.4.3 Seasonal cycle of annual mass balance 10

2.4.4 Variation of surface balance with altitude 11

2.4.5 Generalised relation between surface mass balance to temperature and precipitation 11

2.5 Englacial mass balance 12

2.6 Energy budget 12

Chapter 3 Materials and methods 14

3.1 Study area 14

3.1.1 Past and present monitoring 15

3.2 Meteorological data 17

3.2.1 Processing of Abramov automatic weather station (AWS) data 17

3.2.2 Vertical lapse rates 21

3.2.3 Cloud cover simulation 21

3.2.4 Potential temperature lapse rate 22

3.2.5 Precipitation from ERA-Interim reanalysis 24

3.3 Digital terrain model and glacier outline 24

3.4 The coupled surface mass and energy balance model 26

3.4.1 Surface energy balance model 26
3.4.2 Subsurface model 31
3.5 Numerical setup 33
3.6 Calibration 34
3.7 Initialisation 37
Chapter 4 Results from the model run 38
4.1 Mass balance 38
4.2 Energy budget 42
4.3 Subsurface variables 44
Chapter 5 Discussion and conclusion 47
5.1 Mass balance 47
5.2 Energy budget 49
5.3 Subsurface 52
5.4 Limitations and recommendations 53
5.5 Conclusion 55
References 56
Appendix A Meteorological data processing 60
Appendix B Calibration results 64
Appendix C Results from the model run 67
Appendix D Historical measurements for Abramov 75

Acknowledgements

Firstly, I would like to thank my supervisor Dr. Horst Machguth. Being new to the University of Fribourg and the topic of cryosphere, his guidance and friendliness made the transition a lot easier. He willingly took me on as a student and always made time for me. I really value the extensive discussions we have had and his wealth of knowledge has helped me throughout my masters.

I would also like to acknowledge my co-supervisor and PhD candidate Marlene Kronenberg, whom was also present for many of the discussions, and provided valuable insight about the themes discussed in this master's thesis.

Furthermore, I would like to thank Ward van Pelt (Uppsala University), whom always made time to respond to my emails regarding any question I might have had about the model and its code.

A special thanks goes to my wife, Stephanie Stainbank. Her constant love, reassurance and support have helped me not only during my masters but also through life; I only hope that I can do the same for her. I cannot thank her enough and look forward to our life together.

Finally, I would like to thank my family. They have always been there for me and provided a loving home. Their support, especially when we (Stephanie and I) decided to move abroad, has been overwhelming. I miss you and look forward to my next trip home.

List of figures

2.1 Cross section of a typical valley glacier... 3
2.2 Generalised factors describing the relationship between climate and glacier mass balance... 4
2.3 Variation of zones and their underlying properties for an idealised glacier... 6
2.4 Illustration of mass exchange processes... 8
2.5 An idealised seasonal cycle (one-year) of accumulation and ablation for a glacier... 10
2.6 Conceptual relationship between the surface mass balance and its regulating processes... 11
3.1 Location of Abramov glacier and contour plot (25 m) of surface topography... 14
3.2 Schematic overview of the past monitoring infrastructure.. 16
3.3 Workflow for the processing and preparation of automatic weather station (AWS) data for model input... 19
3.4 A comparison between the filtered dataset (black) and outliers (red) (a); and the 3-hourly dataset (black) and interpolated intervals (blue) (b)... 20
3.5 Time series of climate input variables... 23
3.6 Comparison between the unfiltered (a) and filtered (b) DTM grid (25 m) for the Southern region of Abramov glacier... 35
3.7 Scatter plot of modelled and measured mass balance estimates from stake readings... 36
4.1 Spatial distribution of mean annual mass balance... 39
4.2 Spatial distribution of mean annual refreezing (a) and runoff (b)... 39
4.3 Glacier-wide mean monthly mass balance contribution of solid precipitation, refreezing and melt... 40
4.4 Glacier-wide comparison between the monthly fraction of snowfall and rainfall, and mean monthly air temperature... 41
4.5 Spatial distribution of the melt energy... 43
4.6 Glacier-wide mean monthly surface energy components... 44
4.7 Subsurface densities and temperature evolution... 45
4.8 Comparison between ice core density profiles at C1 and C2... 46
5.1 Time-series of snowfall, rainfall and albedo for the summer... 48
5.2 Spatial distribution of the sensible plus latent heat flux... 51
5.3 Time series glacier-wide simulated daily mean fluxes... 51
A1 Time series of the original dataset (a), filtered dataset (b), and final dataset (c) for temperature... 62
A2 Time series of the original dataset (a), filtered dataset (b), and final dataset (c) for barometric air pressure... 62
A3 Time series of the original dataset (a), and final dataset (b) for relative humidity... 63

A4 Time series of the original dataset (a), and final dataset (b) for incoming shortwave radiation used for simulating the cloud fraction... 63
C1 Time-series of glacier-wide simulated surface temperature (a), air temperature (b), air pressure (c), relative humidity (d), cloud cover (e), rainfall (f), snowfall (g), albedo (h), incoming shortwave radiation (i), reflected shortwave radiation (j), incoming longwave radiation (k), outgoing longwave radiation (l), sensible heat flux (m), latent heat flux (n), and subsurface heat flux... 72
C2 Spatial distribution of surface temperature (a), air temperature (b), air pressure (c), relative humidity (d), cloud cover (e), rainfall (f), snowfall (g), albedo (h), incoming shortwave radiation (i), reflected shortwave radiation (j), incoming longwave radiation (k), and outgoing longwave radiation (l)... 74
D1 Time series of relative humidity and cloud cover for 1995-1998... 76

List of tables

3.1 List of parameters used as input for the coupled model... 17
3.2 Details of grids used in the calibration and numerical experiments of the model... 33
3.3 Summary of model parameters used for the calibration of the coupled model... 34
5.1 Summary of characteristics for Abramov, Morteratsch, and Zhadang glacier... 50
5.2 Comparison of equations used by Van Pelt et al.(2012), Ligtenberg et al. (2011) and this study... 53
A1 Summary of original dataset, identification and removal of outliers, final dataset, and interpolated intervals for the meteorological data... 61
B1 Parameter settings and statistical results for the calibration process... 65
C1 Glacier-wide means of selected coupled model outputs... 68

Chapter 1

Introduction

1.1 Context of study

Glaciers are reliable indicators of climate change, as they respond to fluctuations in atmospheric conditions (IPCC 2013). As such, they provide important insights into the effects of climate change; such as approximating sea-level rise, regional variations in runoff, and impacts of natural hazards (Hoelzle et al. 2017). These insights are particularly important in regions where glaciers provide a valuable source of water for agricultural practices, energy production, and domestic consumption (Cuffey & Paterson 2010; Hoelzle et al. 2017). According to IPCC (2013), glaciers are currently considered to be in a state of disequilibrium with the global warming trend; and will continue to experience mass loss.

Central Asia's arid climate results in a heavy reliance on water from snow and glacier melt. This melt feeds transboundary rivers in the region (Farinotti et al. 2015; Siegfried et al. 2012; Sorg et al. 2012). Since the collapse of the Soviet Union, water allocation conflicts have arisen, and their potential to increase is only exacerbated by political instability and climate change (Bernauer & Siegfried 2012; Siegfried et al. 2012). There is a consensus that most glaciers in the region are retreating, with the rate of mass loss increasing since the 1970s (Farinotti et al. 2015; Huintjes et al. 2015). This result in a shift in the seasonal runoff maxima, with predictions indicating an overall reduction in summer runoff (Bernauer & Siegfried 2012; Sorg et al. 2012). However, there are regional differences between catchments, due to spatial and temporal heterogeneity of climate and climate variability on glaciers (Huintjes et al. 2015). These impacts need to be studied in order to better understand how climate change affects these locations (Siegfried et al. 2012).

Within the context of climate change, mass balance studies are imperative in understanding the relationship between glaciers and climate (Cuffey & Paterson 2010). The mass balance of a glacier is governed by accumulation and ablation processes that occur at the surface and within the glacier. These processes can be simulated using distributed mass balance models, which can vary in complexity but are important to constrain the impact of climate change on glacier mass balance (Bougamont et al. 2005; Huintjes et al. 2015; Klok & Oerlemans 2002; Reijmer & Hock 2008; Van Pelt et al. 2012). Overall, these models account for the spatial variability of incoming shortwave radiation and surface albedo (Reijmer & Hock 2008); two factors that significantly affect melt. However, in order to accurately study and calculate the mass balance of a glacier, it is important to understand and account for both the surface and subsurface processes, both of which determine whether mass is gained or lost over a period of time (Cuffey & Paterson 2010; Pfeffer & Humphrey 1996; Van Pelt et al. 2012). This can be done by using coupled models which calculate the specific mass balance, taking into account accumulation processes such as precipitation, riming, and refreezing of melt and/or rain water in the snow or firn pack; as well as ablation processes such as runoff and sublimation (Van Pelt et al. 2012).

1.2 Aims and objectives

This master's thesis aims to take a coupled energy balance and snow model, that has been setup and extensively applied in mass balance studies of glaciers in Svalbard (Van Pelt et al. 2012; Van Pelt & Kohler 2015; Van Pelt et al. 2016), and adapt the model for use with Abramov glacier. This requires the collection and processing of input data (i.e. meteorological data) to run the model, and the use of *in-situ* measurements and literature to calibrate and determine its reliability. To accomplish this, the following questions were addressed:

1. Can sufficient data be compiled in order to run the coupled model?

2. How do the mass balance results compare with the *in-situ* ablation stake measurements, and published glacier wide mass balance?

3. How do the modelled energy balance parameters compare with literature from similar studies?

4. How does the simulated stratigraphy of subsurface density compare with two ice cores collected in 2018?

1.3 Structure of thesis

This thesis is presented in five Chapters; introduction (Chapter 1), glacier mass and energy balance (Chapter 2), material and methods (Chapter 3), results (Chapter 4), and lastly, discussion and conclusion (Chapter 5).

Chapter 1 gives context to the dissertation, broadly explaining the importance of glaciers in climate studies and Central Asia. A brief summary is given as to why accurate mass balance calculations are vital in understanding glacier evolution. The projects aims and objectives are also outlined in this chapter. Chapter 2 presents the literature on glacier mass and energy balance, and explains the process of how glaciers form and how they gain and lose mass. The energy budget and its impact on melt are also discussed. Chapter 3 contains the material and methods where the study site and input data are presented. Here, the coupled model is also described thoroughly, including its setup, initialisation, and calibration. Chapter 4 presents the results from the model run in three parts; namely mass balance, energy budget, and subsurface variables. Finally, Chapter 5 discusses the results in the context of published literature and *in-situ* measurements, as well as, limitations and recommendations. Lastly, a final conclusion about the results obtained in this study is formed.

Chapter 2

Glacier mass and energy balance

This thesis and chapter is concerned with glacier mass and energy processes for valley or alpine glaciers. Generally, alpine glaciers form at high elevations in mountain cirques from where they flow to lower elevations in the valley.

2.1 Introduction

The formation of glaciers depends on snowfall; and it usually occurs in areas of high elevation or polar latitudes, where winter snowfall exceeds summer melt (Hooke 2005). This process results in a positive specific net budget for an area, otherwise known as the accumulation area (Fig. 2.1). As past snow layers are buried, compaction and snow metamorphism occurs; a process that is generally gradual and complex (Cuffey & Paterson 2010). Snow that has been transformed by these processes and is older than a year is subsequently known as firn, with the process of firnification denoting the formation of solid ice from snow. This usually takes several years to form and depends primarily on temperature; therefore it occurs more readily in temperate regions (Cuffey & Paterson 2010). In the case of valley glaciers, gravitational forces cause the ice to flow to lower elevations (Fig. 2.1). Here ice melt exceeds snowfall which results in a negative specific net budget; known as the ablation area. The equilibrium line separates the accumulation and ablation areas or zones. Traditionally, this line defines the altitude where melt at the end of summer is equal to the net snow accumulation from the previous winter; however, the altitude varies across the glacier due to patterns of snow accumulation, shading, and other factors (Benn et al. 2005; Hooke 2005).

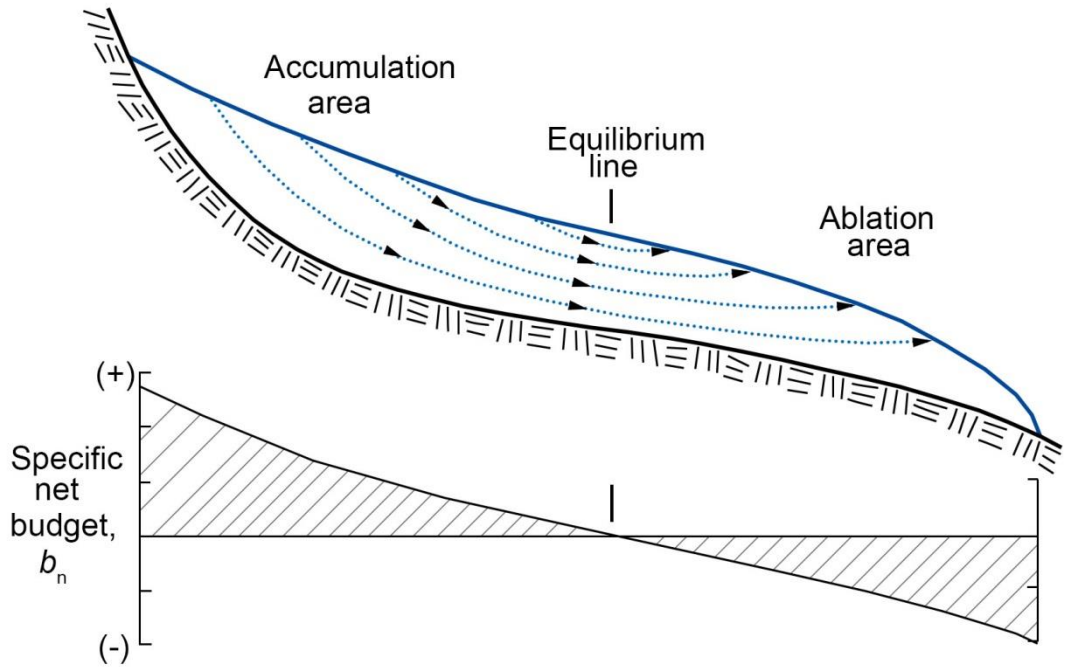


Figure 2.1: Cross section of a typical valley glacier, showing the accumulation and ablation areas, and the relationship between the equilibrium line and flow lines. Modified after Hooke (2005).

The mass balance is the combination of accumulation and ablation processes for the entire glacier over time. This fluctuates over a yearly cycle, whereby mass is acquired in the winter and lost in the summer (Klok & Oerlemans 2002). Accumulation processes results in the addition of glacier ice and can occur at the surface of a glacier through solid precipitation, rime ice, wind drift and avalanches; or within the glacier due to the refreezing of melt and rain water (Van Pelt et al. 2012). In contrast, ablation processes result in ice loss due to melting, sublimation, calving or ice avalanches, as well as wind drift. The net balance over an annual hydrological cycle determines whether a glacier gains or losses mass from one year to the next (Cuffey & Paterson 2010).

Climate plays a significant role in the accumulation and ablation processes, and by studying the mass balance, a better understanding of the complex relationship between glaciers and the climate can be formed. Figure 2.2 helps to generalise this relationship between climate and mass balance using several important factors for a better understanding. The "regional climate" represents weather patterns that affect an area much larger than the local climate but smaller than the global climate. While the "local climate" refers to the conditions directly adjacent to the glacier as well as on the glacier itself, which govern the supply and removal of mass and heat (i.e. accumulation and ablation), and ultimately determines glacier-wide gain or loss of mass. This mass change varies per a unit area over the glacier and is represented by specific balances. The specific balances affect glacier slope and thickness which in turn alters the surface altitude and glacier mass, and whether it will advance or retreat. The dashed lines denote important feedbacks into the system as the glacier reacts to the climate. These feedbacks directly affect mass gain or loss, and in turn can influence the local and regional climates.

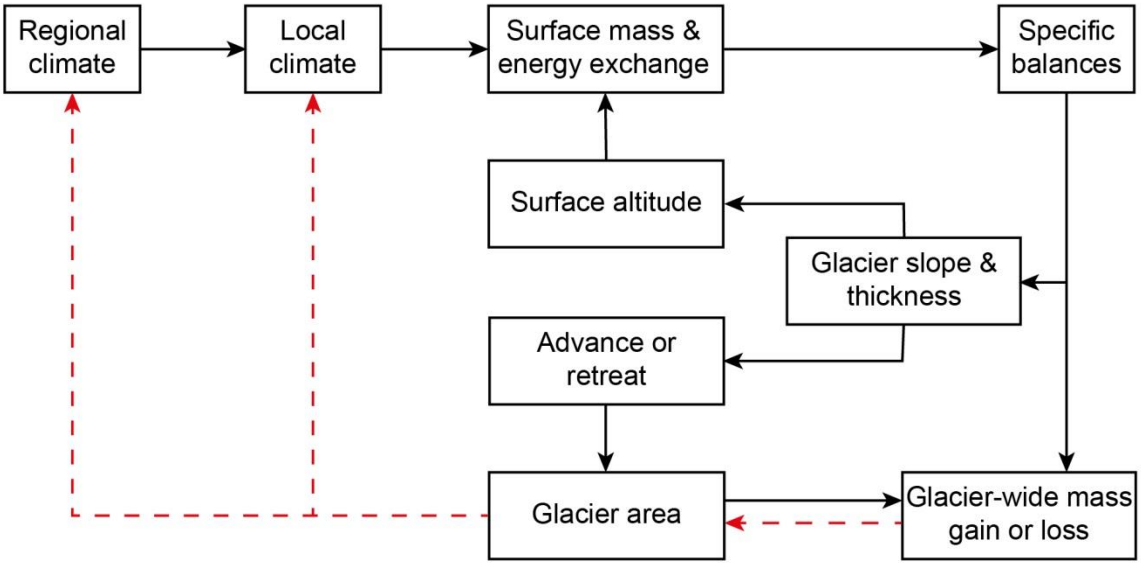


Figure 2.2: Generalised factors describing the relationship between climate and glacier mass balance. Feedback mechanisms are indicated by red dashed lines. Modified after Cuffey & Paterson (2010).

This chapter focusses on the firnification and mass exchange processes pertinent to this dissertation, which include the surface and englacial mass balance. Additionally, the relationship between surface ablation and the climate is discussed in order to better understand the causes of melt through the transfer of heat at the glacier surface. As this process is complex and requires numerous variables,

theory is applied to calculate heat exchange at the glacier surface. The theory is outlined in this chapter, in addition to the factors controlling each variable in the energy budget.

2.2 Transformation of snow to ice

The transformation of snow into glacial ice is considered as one of the most important processes in glaciology (Herron & Langway 1980). This process can be separated into three stages of densification. The initial stage is generally the most rapid, and involves the densification of snow to the "critical density" of roughly 550 kg m^{-3} (Herron & Langway 1980). As snow is the term associated with material that has hardly changed since it fell and usually has a density less than 400 kg m^{-3}; its transformation into ice entails the diffusion of water molecules towards the centre of the snowflakes; causing their surface area to decrease and become rounded (Hooke 2005). Thereby, the principal mechanism during the first stage is grain settling and packing (Herron & Langway 1980). This rounding process tends to occur more rapidly at higher temperatures. According to Hooke (2005), the packing of natural aggregates of spheres of uniform diameter, results in a porosity of roughly 40%, which equates to a firn density of about 550 kg m^{-3}. However, as noted by Cuffey and Paterson (2010), there is no abrupt or clear change in the physical properties when snow becomes firn, thereby reflecting the continuous nature of the transformation process.

Densities continue to increase with depth during the second stage but at a much slower rate up until the interconnecting pores between grains become closed off (pore close off zone); forming individual bubbles at densities of 820-840 kg m^{-3} (Cuffey & Paterson 2010; Herron & Langway 1980). Densification during this stage involves sintering, a process whereby material is transferred by sublimation and molecular diffusion inside grains, growth and nucleation of added grains (Hooke 2005). Other processes include internal or plastic deformation of the grains and recrystallization (Cogley et al. 2011). Initially, the transformation process is influenced by sublimation when pore spaces are still substantial; whereas internal deformation becomes more important as depth and pressure increases. Warm temperatures accelerate the densification process, as water in firn increases the surface tension between grains, and percolating melt water can fill pore spaces and refreeze (Hooke 2005). However, unlike the transition between snow and firn, the transition where firn becomes glacier ice is obvious, and the depth of occurrence depends mainly on temperature (Cuffey & Paterson 2010).

Below the pore close off zone, air is trapped within the ice and the final stage of densification results in the compression of these air bubbles (Herron & Langway 1980). According to Herron and Langway (1980), temperature and accumulation rates govern the form of depth-density profiles; with low accumulation rates and higher temperatures significantly affecting the change of density with depth. Depending on accumulation rates, glacier ice may form in a period of a few years to centuries as a result of loading; whilst refreezing of melt water can produce densities near that of pure ice in less than a day (Cogley et al. 2011).

2.3 Glacier zones and stratigraphy

A glacier can be characterised by a sequence of several zones, starting at the highest elevation and moving down to its terminus. These zones and their underlying properties for a conventional year are displayed in figure 2.3; although, very few glaciers display the entire classification, and in addition the boundaries zones vary between glaciers (Cuffey & Paterson 2010).

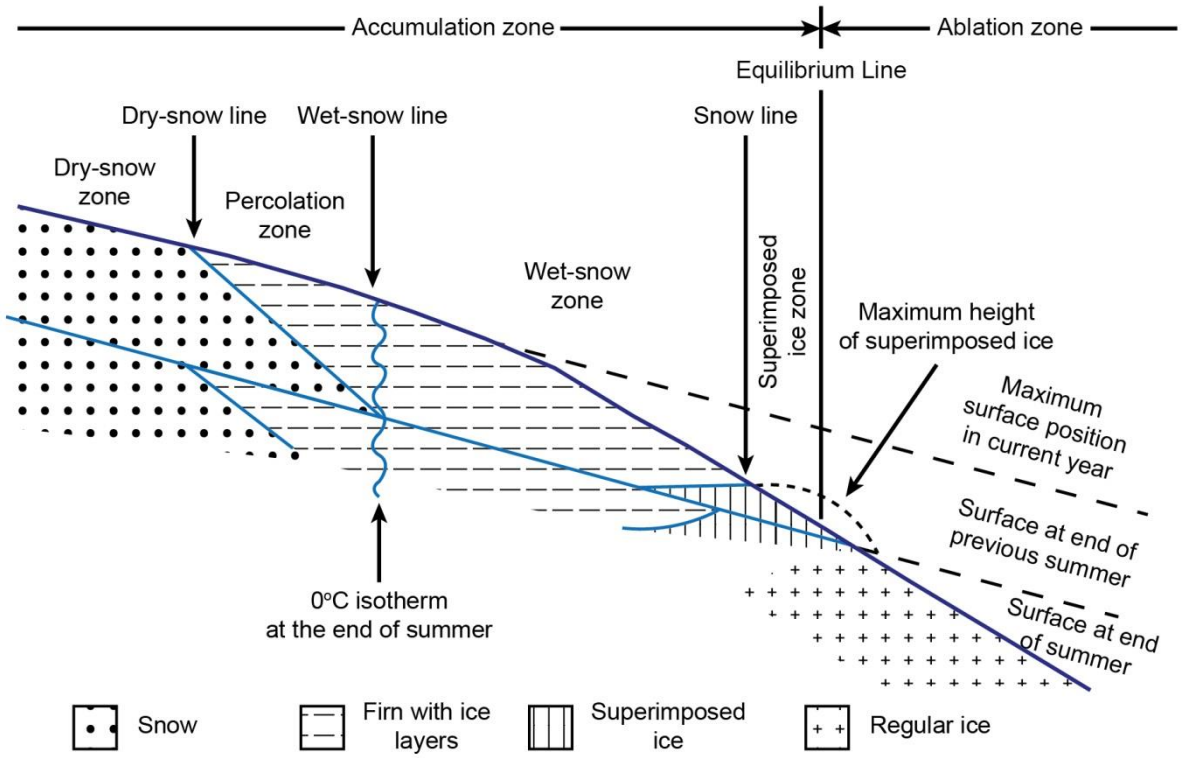


Figure 2.3: Variation of zones and their underlying properties for an idealised glacier. Modified after Cuffey and Paterson (2010).

The dry-snow zone is characterised by an area where no melting occurs, even in summer; and is usually associated with high elevation on polar glaciers (Hooke 2005). At lower elevations, the percolation zone is defined by small amounts of melt, which cause the formation of ice lenses (i.e. horizontal structures) or glands (i.e. vertical channels) as a result of meltwater percolating downwards and refreezing (Cuffey & Paterson 2010). The refreezing process is the most significant element in warming the snow, especially in alpine environments, as the latent heat released from refreezing 1 g of water is enough to raise the temperature of 160 g of snow by 1 °C (Hooke 2005). This process progressively warms the snow to melting point at deeper depths as summer advances. The dry-snow line marks the boundary between these two zones. As mentioned, these zones are associated with polar glaciers and do not usually apply to temperate glaciers where ice is at melting point throughout the subsurface, with the exception of the upper surface where temperature can temporarily fall below 0 °C during the winter months (Cuffey & Paterson 2010).

At lower elevations, there is the wet-snow zone; where melting during the summer is sufficient enough to wet the entire snowpack that has been deposited since the pervious summer, and raise it to melting temperature (Cuffey & Paterson 2010). The subsurface material in this zone is characterised by ice lenses and glands with layers or patches of snow and firn. As the amount of melt water increases with lower elevations, the ice layers merge to form a continuous mass, known as

superimposed ice (Cuffey & Paterson 2010). At the end of the melt season, this superimposed ice is exposed, forming the superimposed ice zone, which is delineated by the snow line at its upper boundary and the equilibrium line at its lower boundary (Cogley et al. 2011). The formation of superimposed ice requires firn temperatures to be negative (i.e. below 0 °C); however, on temperate glaciers, heat conduction downward into the glacier is minimal and does not penetrate much lower than the snowpack, and so the firn stays at 0 °C (Cuffey & Paterson 2010). The equilibrium line is a significant characteristic for mass balance and glacier dynamic studies, and usually coincides with the snow line on temperate glaciers (Cogley et al. 2011). Finally, situated below the equilibrium line is the ablation zone which is characterised by ice and a net loss in glacier mass over the year.

2.4 Surface mass balance

When calving does not play an important role, the net balance is dominated by mass exchange processes at the surface. Over a time period, the surface balance rate, $\dot{b}_s$, at a point can be expressed using the equation from Cuffey and Paterson (2010):

$$\dot{b}_s = \dot{a}_s + \dot{a}_a - \dot{m}_s + \dot{a}_r - \dot{s} + \dot{a}_w, \tag{2.1}$$

where $\dot{a}_s$ is solid precipitation, $\dot{a}_a$ represents avalanche deposition, $\dot{m}_s$ is melt, $\dot{a}_r$ denotes the refreezing of water, $\dot{s}$ is sublimation, and $\dot{a}_w$ signifies wind deposition. Figure 2.4 aids in visually describing these variables. Positive variables represent processes of accumulation; conversely negative variables represent ablation processes. However, wind deposition can either be negative (scour) or positive (deposition); and sublimation can be positive (re-sublimation) or negative. Additionally, avalanches can also be positive or negative, but overall generally add to the glaciers mass. For the majority of points on a glacier, the two dominant processes comprise of snowfall and melt (Hooke 2005). In most cases, refreezing of water refers to melt water but can include precipitation and runoff from the adjacent valley slopes (Van Pelt et al. 2012). Refreezing is an important process and can be defined as internal accumulation, reducing the net runoff of melt water. Figure 2.4 illustrates the mass exchange processes that occur at the glacier surface; where melt is determined by the energy budget from net shortwave radiation (S_{in}, S_{out}), net longwave radiation (L_{in}, L_{out}), turbulent heat fluxes (Q_{sens}, Q_{lat}), sensible heat flux by rain (Q_{rain}), and glacier heat flux (Q_{ghf}).

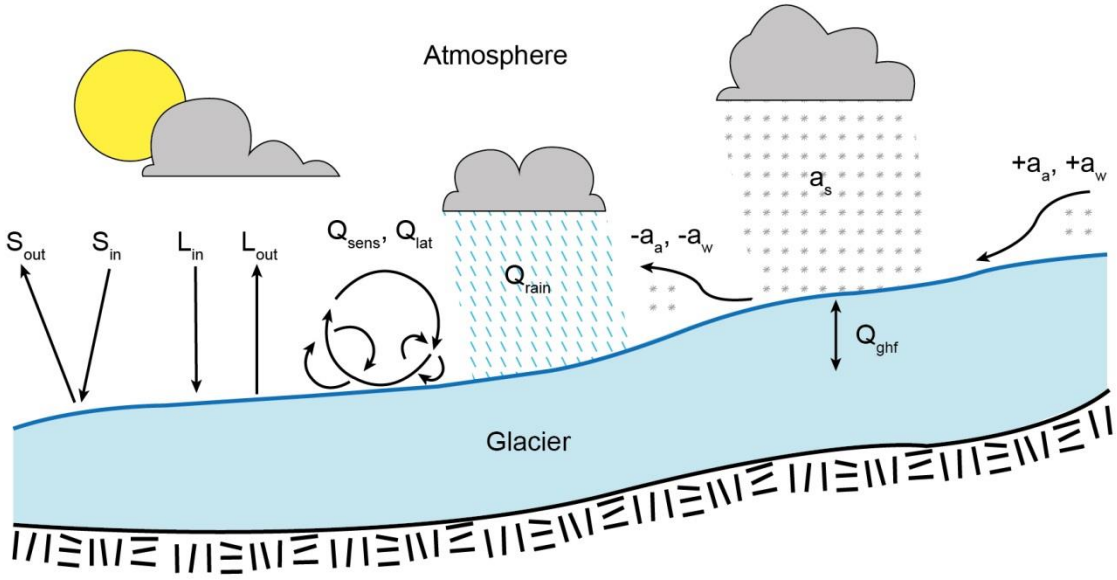


Figure 2.4: Illustration of mass exchange processes at the surface of a glacier where S_{in} represents the incoming shortwave radiation, S_{out} is reflected shortwave radiation, L_{in} denotes the incoming longwave radiation, L_{out} is emitted longwave radiation, Q_{sens} signifies the sensible heat flux, Q_{lat} is the sensible heat flux, Q_{ghf} represents glacier heat flux, a_s is solid precipitation, a_a denotes deposition by avalanching, and a_w is wind deposition.

2.4.1 Surface accumulation processes

Solid precipitation or snowfall governs accumulation and thus formation of glaciers (Hooke 2005). Therefore it is important to understand factors which affect snowfall rates, such as temperature and water vapour content of the atmosphere. Additionally, other elements such as topography, altitude, redistribution by wind and avalanches, and refreezing of melt water affect accumulation.

There is a positive relationship between snowfall and the amount of water vapour content in the atmosphere (Cuffey & Paterson 2010). As the air temperature rises, the saturation vapour pressure (i.e. the pressure at which fluid passes from liquid to gas for a given temperature) increases exponentially; potentially raising the vapour content of saturated air. The cooling of saturated air causes condensation and the formation of cloud droplets or ice particles, which if continue to grow will cause precipitation. This process reveals that the cooling of a given warm air mass produces more precipitation than an equivalent cold air mass; and explains the general trend between the high accumulation rates at warm temperate locations in contrast to the low accumulation rates at cold polar sites (Cuffey & Paterson 2010). Additionally, variations in humidity affect the formation of clouds in the scenario of a cooling dry air mass. For snowfall to reach the ground or glacier surface, subfreezing temperatures are required in the lower atmosphere, and its relative abundance is determined by the rain-snow partitioning (Klok & Oerlemans 2002). Orographic lifting aids in the rapid cooling of air masses and is associated with higher snowfall rates. Additionally, temperature plays a significant role in snowfall, with the highest snowfall rates being associated with intermediate temperatures that correspond with persistent atmospheric uplift (Cuffey & Paterson 2010). However, in environments that are either too cold or warm, temperature can limit snowfall.

Mountain ranges are not only associated with orographic lifting but also create a snowfall gradient whereby snowfall and accumulation increases with altitude (Cuffey & Paterson 2010). The reason being, at high altitudes, the chance of precipitation in the form of snowfall rather than rain is much greater. However, a limit is reached once the water saturation content begins to decline, as water is lost to precipitation and as such snowfall starts to decrease at high altitudes (Cuffey & Paterson 2010).

Accumulation rates are not always uniform across a glacier because wind has the capacity to redistribute snow along the surface (Cuffey & Paterson 2010). The wind interacts with the surface topography to remove snow (i.e. scour) in some areas and deposit it in others. The effects of this process can drastically change the distribution of snow in the accumulation area (Hooke 2005). Similarly, avalanching from steep valley slopes or headwalls can be a key source of accumulation for some mountain glaciers (Hooke 2005). This process can lead to areas of abnormally large accumulation for the given altitude. Deposition of rain, water vapour, and super cooled droplets on the surface produce frost and rime ice. These processes are common on glaciers; however, their contribution to accumulation is usually negligible (Cuffey & Paterson 2010).

Refreezing of melt and rain water is an important process that causes the formation of superimposed ice on the surface or ice layers or lenses in the firn (Hooke 2005). The refreezing of melt water does not contribute to the mass balance but adds mass to the firn and reduces or delays the overall melt leaving the glacier (Reijmer & Hock 2008; Schneider & Jansson 2004). This discrepancy is not always taken into account with models and observations that calculate total surface melt at a point because the process of refreezing often occurs in a different place on the glacier (Schneider & Jansson 2004). In order to calculate the net loss, the refreezing of melt water needs to be calculated separately and subtracted from the overall melt (Cuffey & Paterson 2010). This refreezing predominantly occurs in the accumulation zone due to the presence of a firn layer, while its presence in the ablation zone is negligible.

2.4.2 Surface ablation processes

Surface ablation is dominated by melt and sublimation processes, which are in turn determined by the net flux of energy from the atmosphere (Cogley et al. 2011; Cuffey & Paterson 2010). The net flux of energy is more comprehensively outlined in Section 2.5; while a detailed description of the energy balance model is presented in Section 3.4.

Generally, mass loss is caused by sublimation and melt during the summer, with the latter being followed by runoff; a process that is forced by the net flux of energy from the atmosphere to the surface of the glacier (Fig. 2.4). The two most important fluxes that drive melt are solar radiation (i.e. net shortwave radiation) and the turbulent mixing of heat and vapour directly above the glacier surface (i.e. sensible and latent heat flux). If the surface is at melting point, as is the case with temperate glaciers, melt increases proportionally to the net energy flux (Van Pelt et al. 2012). However, melt can also occur when subfreezing air is present over the surface and turbulent mixing is marginal. Sublimation can occur at any temperature, and is intensified by a warm surface, dry air and strong winds. Although, it is possible for sublimation to alter radiant and sensible heat fluxes to latent heat; reducing the amount of energy and suppressing melting (Cuffey & Paterson 2010). Incoming longwave radiation is also usually offset by outgoing longwave radiation; therefore, net longwave radiation can be described as an energy sink whereby energy available for melt is reduced.

The accumulation of snow plays a significant role in the ablation process; with its high albedo it reduces the amount of incoming solar radiation, thereby reducing melt (Cuffey & Paterson 2010). If there is not a sufficient amount of snow in the accumulation season, firn and ice are more readily exposed in the summer; due to their lower albedo, more solar radiation is absorbed and melt increases. However, snowfall in the ablation season can significantly reduce melt by simultaneously adding mass to the glacier and raising the surface albedo.

2.4.3 Seasonal cycle of annual mass balance

The surface mass balance of temperate glaciers fluctuates substantially over the seasons and may not conform to long-term trends but is generally characterised by winter accumulation and summer ablation (Van Pelt & Kohler 2015). Figure 2.5 illustrates a simplified seasonal cycle in the accumulation zone, where mass is added during the winter; reaching a maximum in late spring, and melting removes mass in the summer; attaining a minimum in late summer. In reality, accumulation increases mass in a stepwise manner corresponding to snowfall events, likewise ablation removes mass with the changing weather conditions (Cuffey & Paterson 2010). At the end of the ablation season, the final surface (known as the summer surface) forms the base for the subsequent accumulation season; and can usually be identified as a dirty layer on temperate glaciers (Cogley et al. 2011). It is important to note, that the length of the balance year varies within the glacier boundary as other factors such as altitude and shading significantly influence local conditions; resulting in a highly variable spatial distribution of accumulation (Cuffey & Paterson 2010). The annual balance can be defined by the specific mass balance at the end of the balance year.

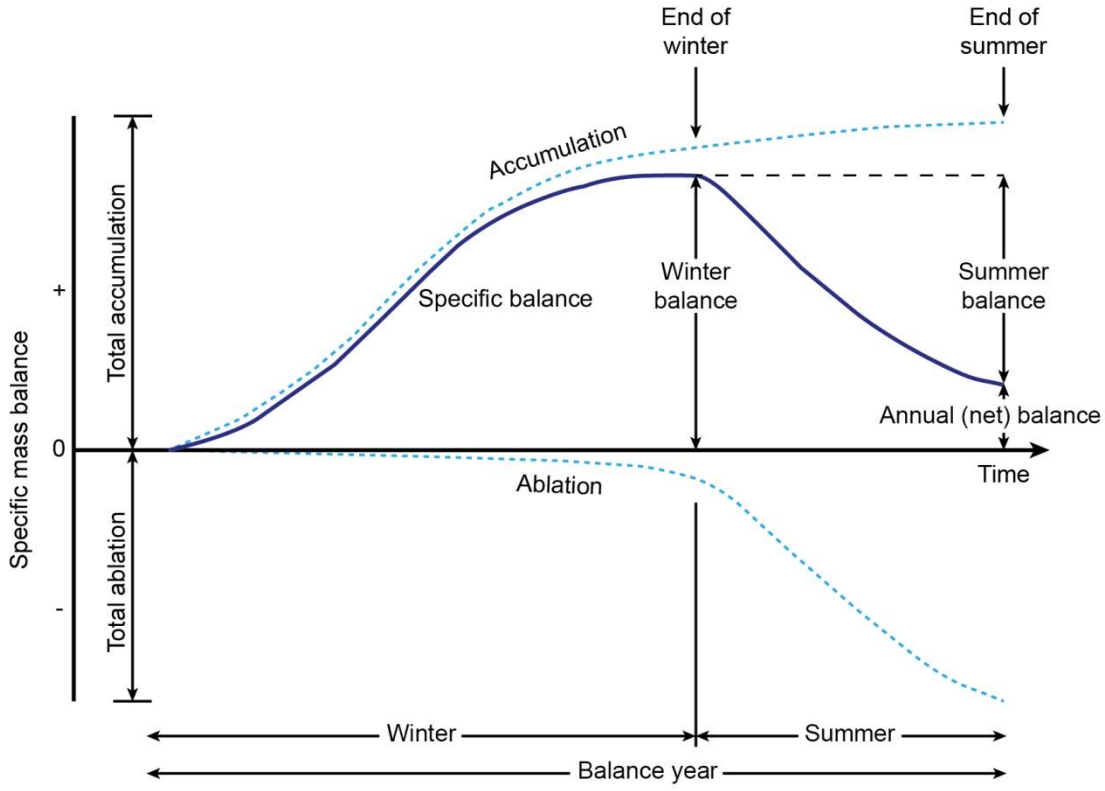


Figure 2.5: An idealised seasonal cycle (one-year) of accumulation and ablation for a glacier. Modified after Cuffey and Paterson (2010).

2.4.4 Variation of surface balance with altitude

The specific balance differs considerably with altitude on a glacier, characterised by an upper region of net accumulation (i.e. accumulation area) and a lower region of net ablation (i.e. ablation area) (Cuffey & Paterson 2010). At the end of the balance year, the surface in the ablation area consists predominantly of bare ice, while the accumulation zone is covered by snow. The equilibrium line marks the boundary between the two zones and its altitude delineates the Equilibrium Line Altitude (ELA). On temperate glaciers, the ELA and end-of-summer snowline are in close proximity; however, it there are not a well-defined 'line' but a transition zone (Cogley et al. 2011). As the equilibrium line represents a transition zone, the glacier surface transforms from snow in the accumulation zone, to snow patches, to bare ice in the ablation zone.

2.4.5 Generalised relation between surface mass balance to temperature and precipitation

Air temperature plays a significant role in the altitudinal gradients of annual surface balances because it determines the amount of snowfall that reaches the ground, directly affects the melt rate, and the duration that the glacier surface is at melting point (Herron & Langway 1980; Hooke 2005). Figure 2.6 shows a simplistic understanding of the relationship. At low temperatures, melt is negligible and surface balance depends on snowfall. As temperatures increase, there is an increase in water content in the air and consequently the rate of snowfall, thereby increasing surface balance. However, at higher temperatures surface balance decreases abruptly as melt and liquid precipitation increase, and snowfall decreases. It should be noted that other factors influence melt rate and not just mean annual temperature, these include the mean summer temperature, the length of the melt season, and the occurrence of summer snowfall (Cuffey & Paterson 2010).

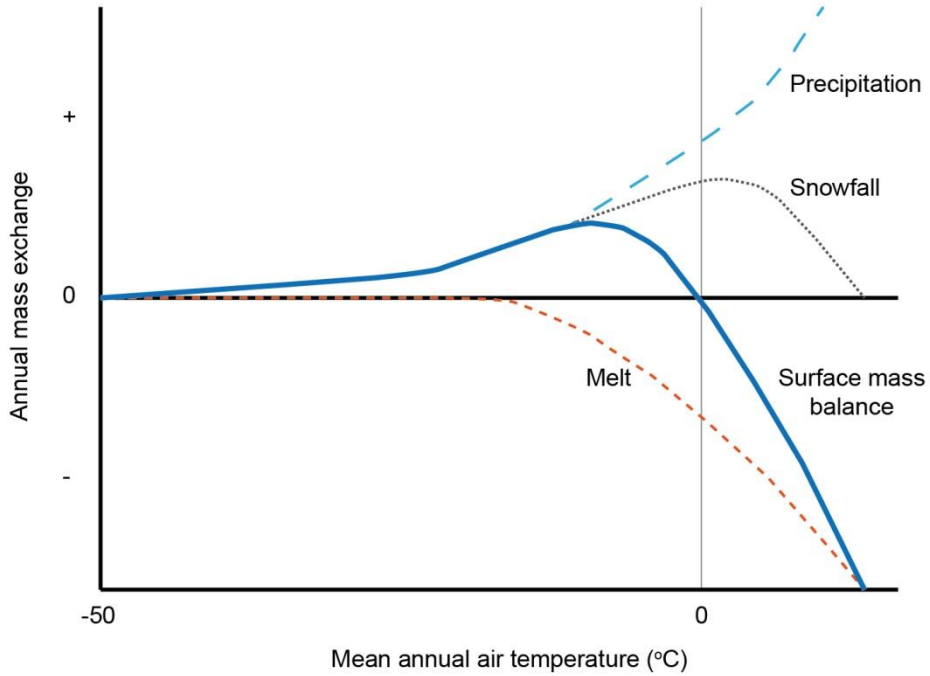


Figure 2.6: Conceptual relationship between the surface mass balance and its regulating processes (i.e. snowfall and melt) to mean annual air temperature. Modified after Cuffey and Paterson (2010).

2.5 Englacial mass balance

Accumulation and ablation process do not only occur at the surface but also within the glacier. Mass from the surface is redistributed downwards into the porous snow or firn in the form of melt water or rain; this water then freezes to form ice lenses or glands (Hooke 2005). This process can be defined as internal accumulation and occurs due to the freezing of percolating water or water trapped by capillary action in the snow and firn (Schneider & Jansson 2004). The physical structure and temperature of the snow are the two defining factors that determine if infiltrating water refreezes or is discharged as runoff (Pfeffer & Humphrey 1996). It is possible to measure refrozen water in the snowpack, however, its distribution and scale is highly variable due to complex percolation and drainage processes (Pfeffer & Humphrey 1996). The processes of melt and refreezing persist and vary over time, thereby complicating mass balance and runoff calculations of glaciers.

2.6 Energy budget

Melt of snow and ice is the most significant process in the relationship between glaciers and climate. It dominates the ablation area at lower elevations and is enhanced by warmer temperatures; although, temperature is not the only component that determines melt (Cuffey & Paterson 2010). Other factors include humidity, air pressure, snowfall, cloud cover, albedo and wind speed. Melt, $\dot{m}_s$, can be determined by calculating the surface energy budget over a time period using the equation:

$$\dot{m}_s = \dot{Q}_{sw} + \dot{Q}_{lw} + \dot{Q}_{sens} + \dot{Q}_{lat} + \dot{Q}_{rain} + \dot{Q}_{ghf} \tag{2.2}$$

where $\dot{Q}_{sw}$ is the net shortwave radiation, $\dot{Q}_{lw}$ represents the net longwave radiation, $\dot{Q}_{sens}$ is the sensible heat flux, $\dot{Q}_{lat}$ signifies the latent heat flux, $\dot{Q}_{rain}$ is the heat supplied by precipitation, and $\dot{Q}_{ghf}$ denotes the conductive ground heat flux. The physics of how these variables are calculated is discussed more thoroughly when describing the coupled model in Section 3.4. Instead, Section 2.5 aims to focus more on the general relationship between the variables, atmosphere and melt.

If the sum of Eq. 2.2 is positive and the glacier surface is at melting point; thus melting will occur. Factors that favour melting include, clear skies during midday (increase in incoming shortwave radiation), low albedo (more absorption of shortwave radiation), warmer air temperatures (sensible heat transfer to the surface), and higher humidity (reduces latent heat loss and increase in greenhouse gasses) (Cuffey & Paterson 2010; Klok & Oerlemans 2002). The latter can also result in increased cloud cover, thereby reducing incoming shortwave radiation.

The most dominant variables that cause melt are incoming shortwave radiation, incoming longwave radiation and sensible heat flux, with the last two being heavily dependent on the heat content of the atmosphere (Cuffey & Paterson 2010). However, the properties of the glacier surface can reduce melt, as albedo determines the reflected shortwave radiation and temperature determines the emitted longwave radiation. The atmosphere also removes heat from the glacier through evaporation, sublimation, and the sensible heat transfer into cold air (Klok & Oerlemans 2002). The surface temperature is continuously trying to find an equilibrium between the air temperature and subsurface, resulting in heat flow by conduction, either to or from the surface. Cold temperatures can penetrate the snowpack during winter which delays summer melt as the surface needs to ware to melting point before melting can begin (Cuffey & Paterson 2010). With the onset of melt, outgoing longwave radiation cannot increase since it is governed by the surface temperature, which cannot warm beyond

0 °C. Overall, the net shortwave radiation is the most dominant in flux of energy, while the net longwave radiation acts as the largest sink.

The turbulent fluxes represent the sensible and latent heat flux, which account for vertical mixing of air by turbulent eddies adjacent to the surface (Klok & Oerlemans 2002). During summer, the air adjacent to the surface (the skin layer) has an equal temperature to the surface, whereas the overlying air (the lower boundary layer) is warmer. As the air mixes, sensible heat is transferred to the surface. The saturation vapour pressure and skin layer temperature determine the moisture content of the air at the surface; in the case of drier air (negative vapour pressure gradient), evaporation or sublimation occurs, transferring moisture away from the surface which consumes latent heat (Cuffey & Paterson 2010). This reduces the amount of energy available for melting. Alternatively, if there is a positive vapour pressure gradient, condensation or re-sublimation occurs; increasing energy available for melting (Cuffey & Paterson 2010). Both these fluxes can be negative or positive depending on the scenario.

Chapter 3

Materials and methods

3.1 Study area

Abramov glacier (39°38’55"N, 71°35'09"E) is a valley-type glacier that is situated in Kyrgyzstan on the southern border with Tajikistan. It is orientated predominantly north on the slopes of the Pamir-Alay mountain system. The glaciers melt water supplies the Koksu River and forms part of the Vakhsh river basin; which is one of the largest tributaries of the Amu Darya river basin that ultimately drains into the Aral Sea. According to Hoelzle et al. (2017), the surface area of Abramov is approximately 24 km^2 with a volume of 2.54 km^3.

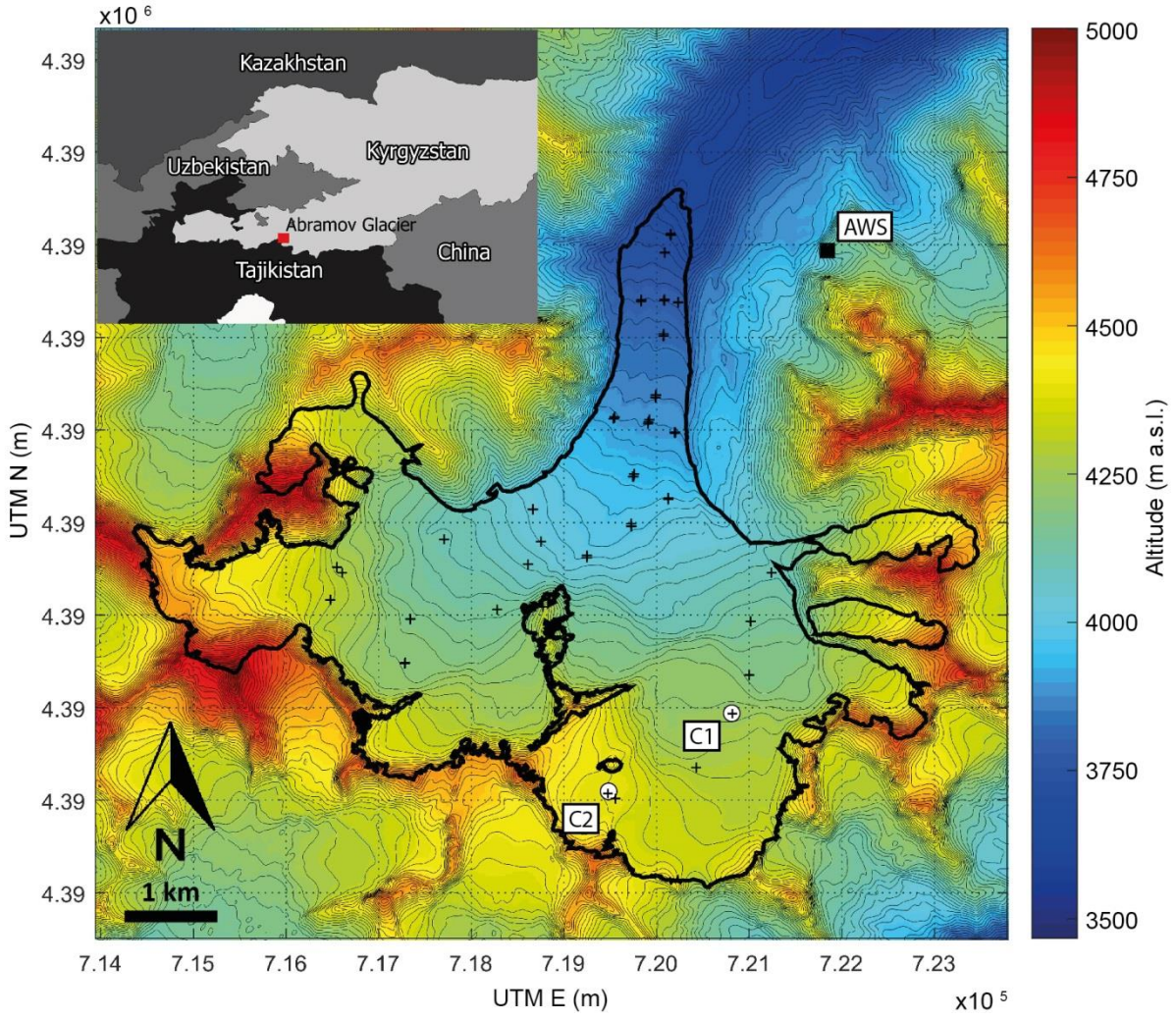


Figure 3.1: Location of Abramov glacier and contour plot (25 m) of surface topography. The glacier is delineated by the black line. White circles represent the position of the ice core drilling sites (C1 & C2), crosses denote the ablation stake network (2014-2017), and the black square signifies the position of the Automatic Weather Station (AWS). Projection: Universal Transverse Mercator (UTM); Zone: 42N; Datum: WGS84; DTM: Pléiades.

The Abramov glacier surface extends from roughly 3600 to 5000 m a.s.l. and is considered to have a temperate accumulation zone (Hoelzle et al. 2017; WGMS 1996). The glacier has a continental type climate with a mean annual air temperature of -6.5 to -8 °C at its equilibrium line (around 4260 m a.s.l.), and an average annual precipitation of approximately 750 mm at 3837 m a.s.l. (Glazirin et al. 1993; Kamnyansky 2001). According to Kislov (1982), Abramov has a temperature gradient of -5 °C km^{-1}. Additionally, there is an exceptionally steep precipitation gradient, with a mean precipitation of 340 mm at the glacier terminus (3600 m a.s.l.) and 1800 mm above 4200 m a.s.l. from October to May (Kislov 1982). However, this gradient becomes smaller, with a mean precipitation of 153 mm at 3600 m a.s.l. and 310 mm at 4200 m a.s.l. during the summer. This equates to a precipitation gradient of 2.4 mm m^{-1} in the winter and 0.26 mm m^{-1} in the summer. Winter accumulation accounts for 80 % of the annual precipitation, and predominantly occurs between October to December and February and April (Kislov 1982; Pertziger 1996)

3.1.1 Past and present monitoring

Abramov glacier has been extensively studied since the construction of a research station in 1967 by the Central Asian Hydrometeorological Research Institute (SANIGMI). From here, continuous glaciological and meteorological observations were performed up until the destruction of the research station in August of 1999 (Hoelzle et al. 2017). Figure 3.2a illustrates how the detailed monitoring programme was established; comprising 165 stakes, they were utilised to measure snow depth at the end of the accumulation season (May), as well as cumulative melt and snow depth at the end of the ablation season (September) (Barandun et al. 2015). In addition, eight snow pits were used to measure snow density and depth on a monthly basis (Pertziger 1996). From 1972 to 1975, extensive firn density, layer stratigraphy and temperature profiles were conducted (Barandun et al. 2015).

After ±20 years, monitoring was re-established in 2011 (Fig. 3.2b), with a network of 16 ablation stakes with snow pits added the following year. The snow pits are located in separate accumulation basins to the stakes and are used to measure snow depth and density in order to determine annual accumulation (Barandun et al. 2015). These measurements have been carried out annually in August since 2011.

Additionally, in 2011 a Remotely Operated Multi-Parameter Station (ROMPS), more commonly known as an Automatic Weather Station (AWS) was installed as part of the Central Asian Water (CAWa) and Global Change Observatory Central Asia (GCO-CA) networks (Schöne et al. 2013). The AWS is situated near the glacier front (39°39'N, 71°35'E) at an altitude of 4100 m a.s.l. (Schöne et al. 2013). Furthermore, in the framework of Capacity Building and Twinning for Climate Observing Systems (CATCOS) project, two terrestrial cameras were installed to monitor the snow line (Hoelzle et al. 2017).

More recently, an expedition was conducted in the January of 2018, during which two ice cores were collected and analysed (M Kronenberg 2018, pers. comm.). The locations of the cores are plotted in Figure 3.1. For further information, in Section 4.3, the density profiles from the cores are presented in and compared to the modelled cores at the same locations.

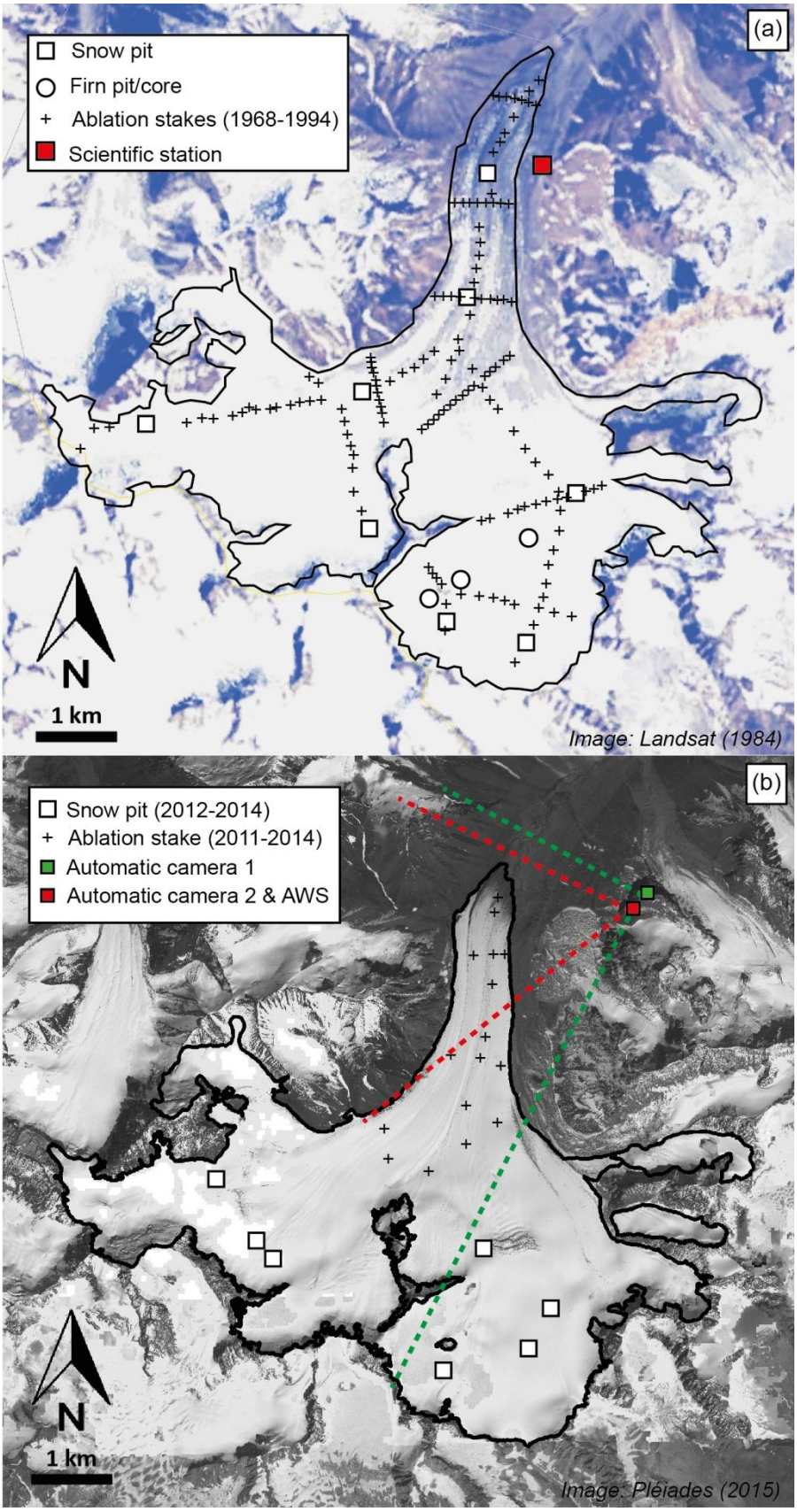


Figure 3.2: Schematic overview of the past monitoring infrastructure from 1967-1994 (a), and the renewed monitoring from 2011-2014 (b). Modified after Barandun et al. (2015).

3.2 Meteorological data

The coupled model that was applied in this study required several meteorological input parameters, namely air temperature, barometric air pressure, relative humidity, cloud cover, potential temperature lapse rate, and precipitation (Table 3.1). The sources of these parameters varied from *in-situ* measurements, modelled data and reanalysis data. The AWS provided measurements for air temperature, barometric air pressure, and relative humidity. Cloud cover was simulated from measured incoming shortwave radiation at the AWS, while the potential temperature lapse rate was determined by calculating the potential temperature at a specified elevation. Additionally, precipitation was extracted from ERA-Interim reanalysis as it was not recorded by the station.

Table 3.1: List of parameters used as input for the coupled model.

Parameter	Unit	Source
Air temperature	K	Measured (AWS)
Air pressure	Pa	Measured (AWS)
Relative humidity	%	Measured (AWS)
Cloud cover	Fraction	Simulated (Section 3.2.3)
Potential temperature lapse rate	K m^{-1}	Simulated (Section 3.2.4)
Precipitation	mm w.e. s^{-1}	ERA-Interim reanalysis

3.2.1 Processing of Abramov automatic weather station (AWS) data

The AWS registers several parameters at 5 minute intervals; however, since its installation, there have been frequent instances where parameters have failed to be recorded at such precise intervals. The time period of missing data can vary from a few missing intervals (i.e. minutes to hours) which are the most common cases, to periods of days or months which are infrequent and represent the most extreme cases. Instances of incorrect sensor measurements or malfunction were also noted for shorter time periods. Further details regarding the raw dataset can be found in Appendix A.

Before input into the model, the AWS data was processed; in order to create a continuous dataset, fix known clock errors, filter outliers, summarise dataset into 3-hourly intervals, adjust for time zone differences, and fill data gaps. Temperature, barometric air pressure, and relative humidity all required processing using an iterative manner in MATLAB® (Appendix A). Figure 3.3 illustrates the workflow used for the processing and preparation of the AWS data for input into the energy balance model.

Firstly, using the initial dataset that consisted of all measurements from 28 August 2011 to 1 December 2017 (i.e. raw data), a continuous dataset was created that filled in all missing measurements with a time stamp and a corresponding Not-a-Number (NaN) value in place of a recording. The entire time series was then analysed, with the identification and removal of outliers using a three-step approach; namely the inter quartile range (IQR) approach, 3-hourly moving mean method, and manual filtering (Fig. 3.4a). This three-step approach was applied only to air temperature and barometric air pressure.

The first step (IQR approach) involves the calculation of empirical quantiles to identify outliers for the entire dataset (Eischeid et al. 1995; Wilks 2011). The median,$q_{0.5}$, or 50th percentile is calculated using the formula:

$$q_{0.5} = \begin{cases} x_{([n+1]/2)} & , n \text{ odd} \\ \dfrac{x_{(n/2)} + x_{([n/2]+1)}}{2} & , n \text{ even} \end{cases} \quad (3.1)$$

The upper quartile or $q_{0.75}$ and lower quartile or $q_{0.25}$ are the medians between $q_{0.5}$ and the extremes, x_1 and x_n. The IQR is the difference between $q_{0.75}$ and $q_{0.25}$. The quartiles and IQR are used to calculate the upper and lower outer fences using the expressions:

$$\begin{aligned} Upper\ outer\ fence &= q_{0.75} + 3 * IQR \\ Lower\ outer\ fence &= q_{0.25} - 3 * IQR \end{aligned} \quad (3.2)$$

Measurements that fell outside of these fences were removed from the dataset and given a NaN value. This robust method performed well to remove outliers that were caused by incorrect sensor recordings or malfunctions. The extreme nature of these outliers ensured that this filtering did not compromise the integrity of the dataset and would allow better results in the next step of filtering.

In the second step, outliers were identified and removed using a moving mean method which is more sensitive to the spread of the measurements (Wilks 2011). This was done by calculating the 3-hourly mean and standard deviation for the entire time series. Outliers that were more than 3 standard deviations from the 3-hourly mean were removed.

Further analysis of the time series indicated short periods where data did not conform to what is physically acceptable after the moving mean method was applied. The presence of these values was a limitation of the moving mean method, and their identification and classification were required to be done manually in a third step. Manual editing was applied to the continuous 5 minute interval dataset; which was then run through step one and two of the filtering process. Figure 3.4a provides one example of manual filtering for a three day period in June 2014.

After the filtering process, the data were summarised into 3-hourly intervals (Fig. 3.4b). For a 3-hourly period a minimum of 6 measurements were required to make the mean valid, otherwise a NaN sign was assigned to the interval. The time stamps were recorded in Central European Summer Time (CEST) and were therefore corrected by adding 5 hours for Kyrgyzstan Time (KGT)..

Following the filtering process, the AWS data for the period from 1 October 2013 to 1 December 2017 was identified as the most suitable for the model. The defining reason was that large data gaps occurred in the dataset prior to 1 October 2013; which were too large to be interpolated and would require reanalysis data to fill them. The chosen period does however have varying degrees of missing data; from 1 up to 24 consecutive missing intervals. These gaps were filled using a MATLAB® autoregressive modelling function (*fillgaps*) that estimates each NaN value using all previous points for forward estimation and all future points for backward estimation (Fig. 3.4b) (Appendix A).

The final dataset used for input into the coupled model was from the 1 November 2013 to 30 September 2017. Although the AWS extended to 1 December 2017, the end date was restricted by the availability of ERA-Interim reanalysis data used for precipitation. The processing of incoming shortwave radiation was also done using this method (Fig. 3.3) and was used to simulate cloud cover. The final dataset was then combined with cloud cover, precipitation, and potential temperature lapse rates for input into the energy balance model.

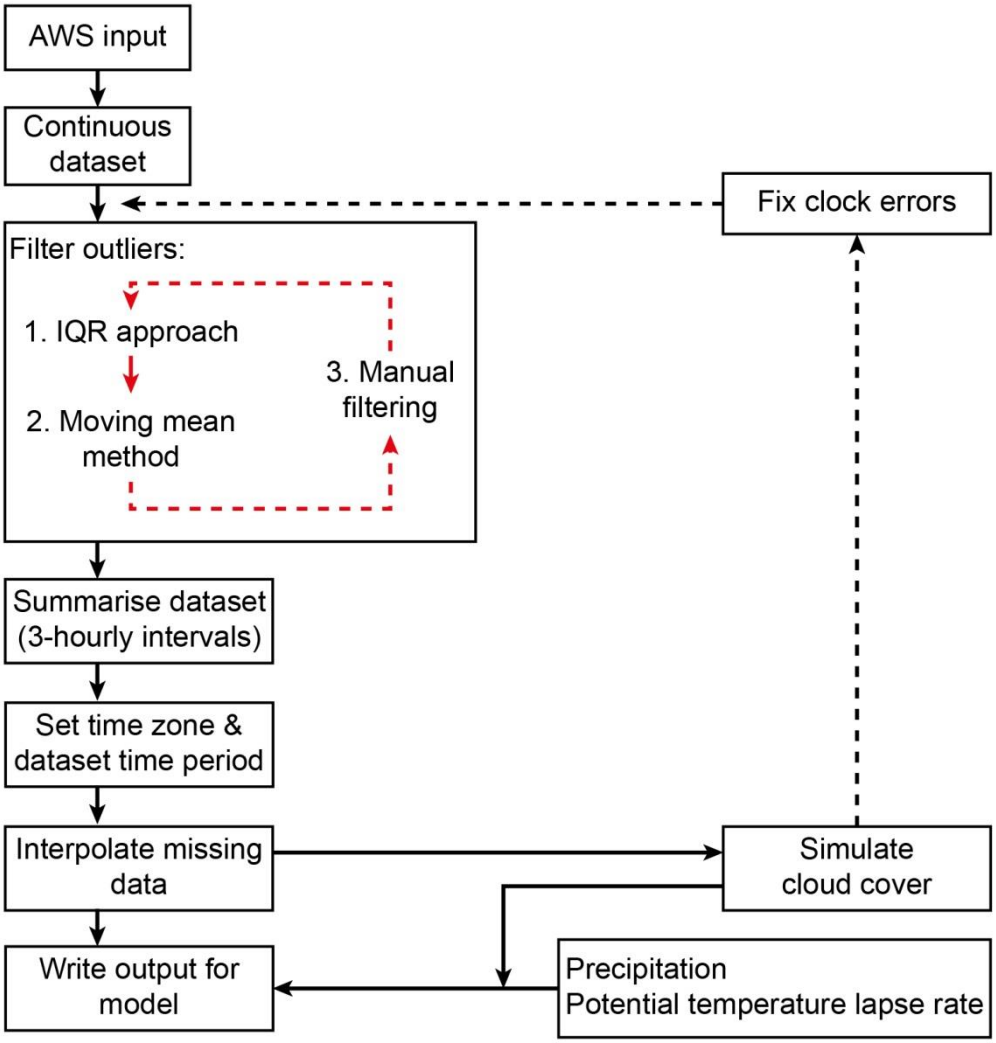


Figure 3.3: Workflow for the processing and preparation of automatic weather station (AWS) data for model input. The dashed lines represent a step only required after further analysis of the data.

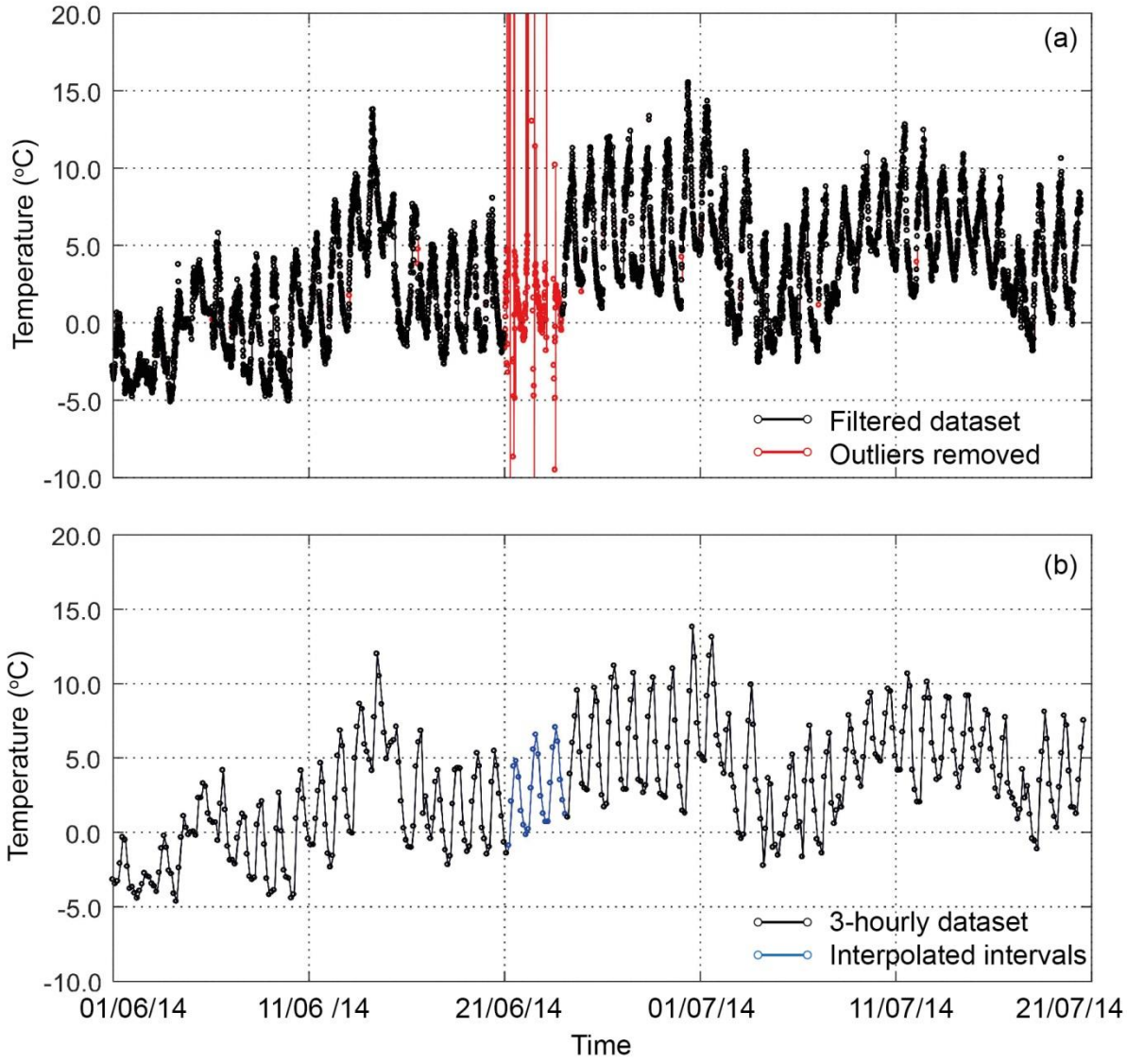


Figure 3.4: A comparison between the filtered dataset (black) and outliers (red) (a); and the 3-hourly dataset (black) and interpolated intervals (blue) (b) for the processing of temperature (°C) for the period 1 June to 21 July 2014.

3.2.1.1 Air temperature

The processing of the recorded AWS air temperature data followed the workflow illustrated in Figure 3.3 and described above. The AWS data was recorded in degrees Celsius (°C) and was converted to Kelvin (K) as required for the model. The initial 5 minute interval dataset consisted of 445943 measured intervals from August 2011 to December 2017; which translates to roughly 47% of missing intervals. The filtering of outliers removed a further 1100 recordings. From this, a 3-hourly dataset was created that consisted of 18297 measurements and 1230 NaN values. The final dataset (Fig. 3.5a) comprised of 11433 intervals of which 60 were interpolated; for the period November 2013 to September 2017 (Appendix A).

3.2.1.2 Barometric air pressure

The AWS air pressure data was processed using the same workflow displayed in Figure 3.3 and described in Section 3.2.1. The data was recorded in hectopascals (hPa) and was converted to Pascals (Pa) as required for the model. The initial 5 minute interval dataset consisted of 446141 measured intervals from August 2011 to December 2017; which indicates that about 47% of timesteps were missing. The filtering of outliers removed a further 4689 recordings with the majority being removed manually (79 %). From this, a 3-hourly dataset was created that consisted of 18297 measurements and 1364 NaN values. The final dataset (Fig. 3.5b) comprised of 11433 intervals of which 156 were interpolated; for the period November 2013 to September 2017 (Appendix A).

3.2.1.3 Relative humidity

The processing of relative humidity followed the same method as in Figure 3.3; however, the filtering of outliers was not applied. Due to the nature and fluctuation of relative humidity, the three step filtering process was insufficient for identifying outliers. Instead an upper threshold of 100 % and a lower threshold of 0 % were applied; any value above the upper threshold was set to 100 % and any value below the lower threshold was set to 0 %. Additionally, it was measured at the AWS as a percentage and thus no conversion was required. The final dataset (Fig 3.5c) comprised of 11433 intervals of which 42 were interpolated; for the period November 2013 to September 2017 (Appendix A).

3.2.2 Vertical lapse rates

For the energy balance calculations the coupled model requires the vertical lapse rates of air temperature, air pressure and relative humidity in order to linearly extrapolate these variables over the glacier grid. In past studies (Klok & Oerlemans 2002; Van Pelt et al. 2012) altitudinal gradients were linearly interpolated between two Regional Atmospheric Climate Model (RAMCO) grid points or weather stations at every model time-step. However, due to the remoteness of Abramov it was not possible to apply such a process; instead, a constant gradient was applied for each parameter. For air temperature, a reported lapse rate of -0.005 K m^{-1} was applied (Kislov 1982); but there was no information regarding relative humidity and air pressure. As an alternative, the mean altitudinal gradient for relative humidity (0.01 % m^{-1}) and air pressure (-1.242 x 10-4 Pa m^{-1}) from Nordenskiöldbreen, Svalbard were utilised (Van Pelt et al. 2012). Due to the climatic difference between Svalbard and Abramov, these values present a source of uncertainty.

3.2.3 Cloud cover simulation

Cloud cover was simulated using the 3 hourly AWS data (i.e. air temperature, air pressure, and relative humidity) combined with measured incoming shortwave radiation that was recorded at the AWS in W m^{-2}. For the incoming shortwave radiation no filtering of outliers was performed; however, a lower threshold of 0 was set as some values were negative. Cloud cover or cloudiness, n, is derived from the transmission coefficient, T_{cl}, that is applied to the clear sky shortwave radiation using the ratio from Machguth et al. (2008):

$$T_{cl} = {S_{in_{meas}}}/{S_{in_{cs}}} \tag{3.3}$$

where $S_{in_{meas}}$ is the measured incoming solar radiation and $S_{in_{cs}}$ represents the potential global radiation under clear-sky conditions. T_{cl} is used as a reduction factor to simulate incoming shortwave radiation and to estimate n according to the work presented by Greuell et al. (1997):

$$T_{cl} = 1.0 - 0.233n - 0.415n^2 \tag{3.4}$$

During the night, cloudiness was linearly interpolated from n before sunset and after sunrise. The initial cloud cover estimates indicated large delta values for the period of 23 April 2014 to 08 August 2014 when compared with the entire dataset. These large delta values were due to a clock offset that caused a backward shift of $S_{in_{meas}}$. This meant that in the afternoon $S_{in_{meas}}$ was significantly lower than $S_{in_{cs}}$ resulting in a greater T_{cl} and therefore an increase in n; conversely in the mornings $S_{in_{meas}}$ was always higher than $S_{in_{cs}}$. Further analysis indicated a clock error of minus 2 hours that was later confirmed by the AWS operators and subsequently the data was corrected (C Zech 2018, pers. comm.). The results from the simulation of cloud cover are presented in Figure 3.5d.

3.2.4 Potential temperature lapse rate

In previous studies (Van Pelt et al. 2012), the potential temperature lapse rate was calculated between two meteorological stations or between two Regional Atmospheric Climate Model (RACMO) grid points. This study relied on calculating the air temperature and pressure for a pseudo weather station at an altitude of 5120 m a.s.l. using the AWS data. Temperature at the pseudo station, T_p, was calculated by:

$$T_p = T_{aws} - L\left(z_p - z_{aws}\right) \tag{3.5}$$

where T_{AWS} represents the temperature at the AWS (K), L is the temperature lapse rate for Abramov glacier ($-0.005\ K\ m^{-1}$), z_p denotes the altitude of the pseudo station, and z_{AWS} is the altitude of the AWS. The air pressure at the pseudo station, P_p, was determined using the equation:

$$P_p = P_{aws}\left(T_{aws}/T_p\right)^{g_0 * M/R^* * L} \tag{3.6}$$

where P_{aws} is the air pressure measured at the AWS (Pa), g_0 represents the gravitational acceleration ($9.80665\ m\ s^{-1}$), M is the molar mass of air ($0.0289644\ kg\ mol^{-1}$), and R^* denotes the universal gas constant ($8.3144598\ J\ mol^{-1}\ K^{-1}$).

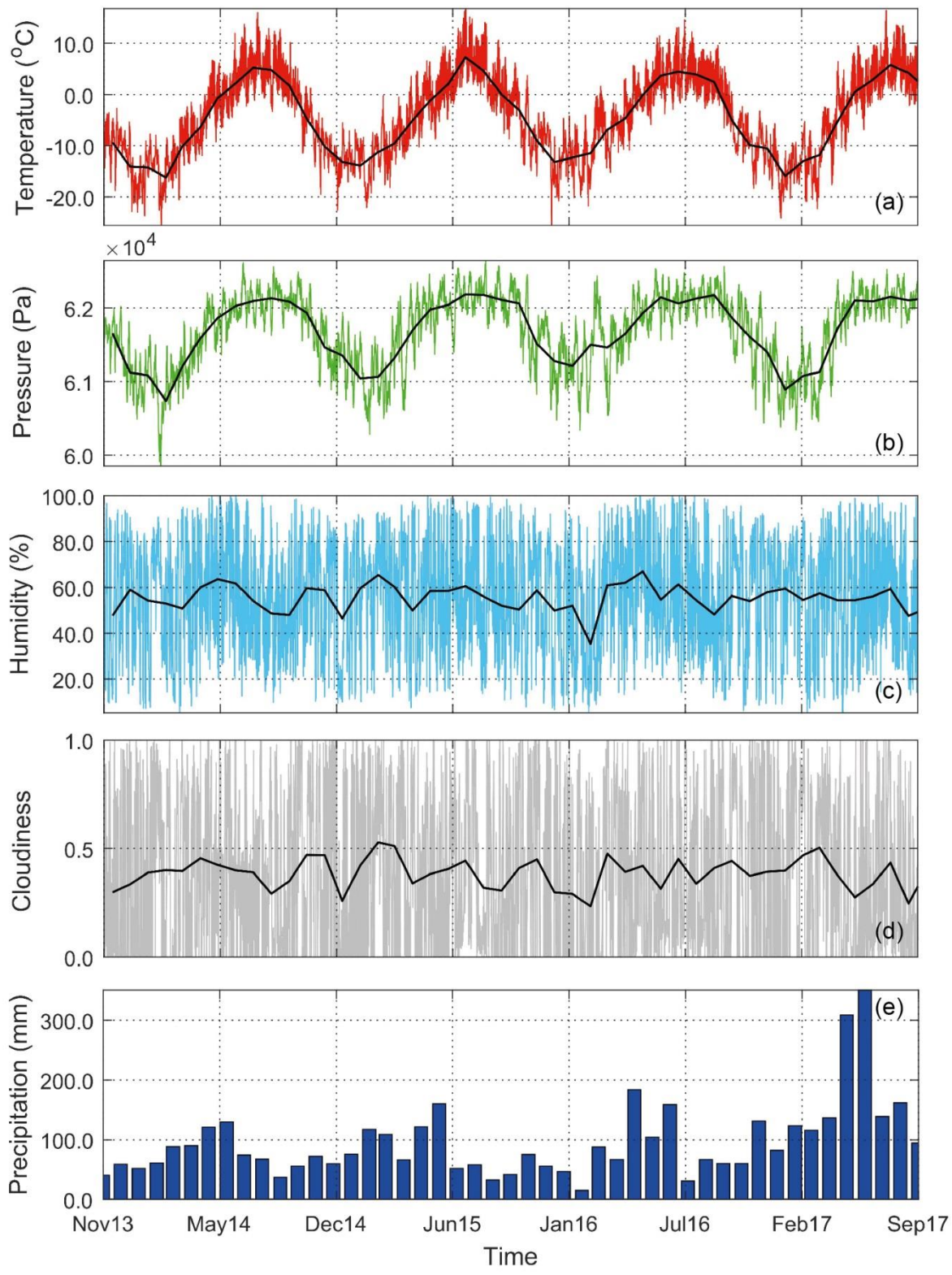


Figure 3.5: Time series of climate input variables air temperature (a), barometric air pressure (b), relative humidity (c), cloud cover (d), and precipitation (e) for the period November 2013 to September 2017. The black lines plotted in (a) to (d) represents monthly means.

3.2.5 Precipitation from ERA-Interim reanalysis

The Abramov AWS does not have an instrument to measure precipitation and with no other weather station nearby, the most suitable option was to use reanalysis data for precipitation. Reanalysis data helps to provide an insight into global circulation for the atmosphere by taking past atmospheric observations and applying modern data quality checks and re-processing using state-of-the-art numerical weather prediction (NWP) analysis and forecast system (Berrisford et al. 2011). There are several reanalyses which provide a system whereby the global circulation of the atmosphere can be viewed. There are two major reanalyses, ERA-15 and ERA-40, which have been produced by the European Centre for Medium-Range Weather Forecasts (ECMWF) and used extensively in the past. The newly generated ERA-Interim is one of the latest reanalysis by ECMWF and aims to address problems associated with ERA-40 (Berrisford et al. 2011; Dee et al. 2011).

ERA-Interim improvements include the application of 4D variational assimilation, variational bias correction of satellite radiances, higher horizontal resolution (i.e. 80 km), a new humidity analysis, improved model physics, and the homogenisation of radiosonde temperature observations (Berrisford et al. 2011). According to Dee et al. (2011), the quality requirements for reanalysis are that global estimates of the general fields of the Earth's atmosphere are consistent with observations given their estimated uncertainties, as well as, physical coherence of estimated parameters (i.e. consistent with the laws of physics and observations). This is achieved with the use of a forecast model to assimilate and compare observations of numerous types and from different sources. With a suitably realistic model it is possible to extrapolate observations to nearby areas which lack observations (Dee et al. 2011). As such, this method allows for the estimation of meaningful precipitation values from a reanalysis of temperature, humidity and wind observations. The ERA-Interim reanalysis data has been used in previous studies of mass balance for Abramov glacier and was consider to yield the most accurate results (Barandun et al. 2015).

Consequently, monthly precipitation data was supplied by ERA-Interim using the nearest grid point to Abramov glacier (Fig. 3.5e). For each month, the sum of precipitation was evenly divided between time intervals with a cloud fraction of 0.70 or greater and converted to mm w.e. s^{-1}.

3.3 Digital terrain model and glacier outline

The original digital terrain model (DTM) had a 4 m resolution and was created from three pairs of stereo images acquired from Pléiades on the 20 August 2015 and 1 September 2015. More detailed information regarding the collection and processing of the Pléiades data can be found in the work presented by Denzinger (2018).

As noted in Denzinger (2018), the accumulation area is plagued with data gaps and artefacts, especially on the western-side; however, the coupled model requires a complete DTM. In order to produce a complete DTM with fewer artefacts required the manual removal of inaccurate elevation points as well as the interpolation of missing elevation points (Fig. 3.6). The removal of inaccurate grid points was done by converting the original DTM into a point cloud for the ease of deleting inaccurate points. With the use of generated surface models at various resolutions and contour lines; inaccurate and duplicate points were manually identified and removed. No-data grid cells were interpolated using neighbouring grid points. The original DTM was down sampled using the triangulation with linear interpolation method to a 100 m resolution grid that was used for the calibration of the coupled model, and a resolution of 25 m that was used for the final coupled model run.

The glacier outline was based on the Pléiades orthographic imagery and was compiled by Denzinger (2018). It serves as a mask to delineate the glacier from the surrounding terrain. The final grid was imported into MATLAB® together with a mask outlining Abramov glacier.

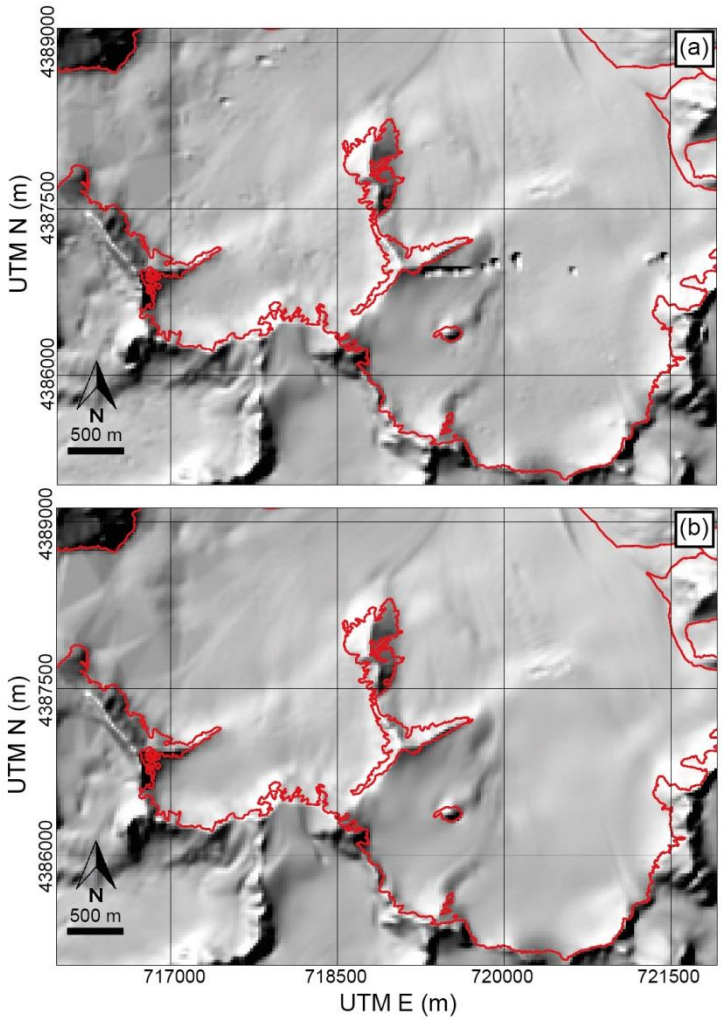


Figure 3.6: Comparison between the unfiltered (a) and filtered (b) DTM grid (25 m) for the Southern region of Abramov glacier. The glacier boundary is represented by the red line.

3.4 The coupled surface mass and energy balance model

This study applied a distributed energy balance model coupled to a multi-layer snow model to the Abramov Glacier. Previously, the coupled model has been utilised to study mass balance and firn evolution in Nordenskiöldbreen in central Svalbard (Van Pelt et al. 2012; 2013; 2014; Vega et al. 2016), Kongsvegen and Holtedahlfonna in western Svalbard (Christianson et al. 2015; Van Pelt & Kohler 2015), and the impact of snow conditions and refreezing on the mass balance of an idealized Svalbard glacier (Van Pelt et al. 2016).

The distributed energy balance model is based on the work untaken by Klok and Oerlemans (2002) and the snow model is based on the SOMARS (Simulation Of glacier surface Mass balance And Related Subsurface processes) model developed by Greuell and Konzelmann (1994). The models are coupled by the melt water production and subsurface heat flux. The melt water production is calculated by the energy balance model that serves as input for the subsurface model, which simulates storage and refreezing of percolating water. The subsurface heat flux required for the surface energy budget is dependent on the vertical profiles of temperature and density.

For a grid cell on the glacier, the specific mass balance is defined as the accumulated exchange of mass per unit area (i.e. accumulation and ablation) over a period of time. Accumulation is the sum of precipitation, riming, and refreezing of melt and rain water within the snow or firn layer, and ablation is the sum of runoff and sublimation. Therefore, accurate mass balance simulations need to address both surface and subsurface mass fluxes.

3.4.1 Surface energy balance model

The model is driven by meteorological input data (i.e. air temperature, relative humidity, air pressure, cloud cover, potential temperature lapse rate and precipitation) from the AWS (Section 3.2) and together with the grid (Section 3.3), the surface energy budget is calculated from the sum of all energy fluxes for each grid cell at every 3 hour interval. The energy required for melting, Q_{melt}, is determined by the sum of all fluxes, and is described by the energy balance equation presented in Van Pelt et al. (2012; 2016) after Klok and Oerlemans (2002):

$$Q_{melt} = Q_{sw} + Q_{lw} + Q_{sens} + Q_{lat} + Q_{rain} + Q_{ghf} \quad (3.7)$$

where Q_{sw} is the net shortwave radiation, Q_{lw} represents the net longwave radiation, Q_{sens} and Q_{lat} are the sensible and latent heat flux (i.e. turbulent fluxes), Q_{rain} denotes the heat transfer by precipitation, and Q_{ghf} is the conductive ground heat flux. Q_{sw} is calculated from the sum of incoming and reflected solar radiation, while Q_{lw} is the sum of incoming and emitted longwave radiation. Fluxes that incident on the surface are positive. Using Eq. 3.7 the model iteratively calculates the energy fluxes with Q_{melt} equal to zero and the surface temperature being the only unknown. If the surface temperature is calculated to be above the melting point, it is then set to 0°C and the energy fluxes are recomputed. In such an event, there is an excess of energy and melting will take place. The surface energy fluxes also supplies energy for Q_{ghf} and together with Q_{melt} determine the warming or cooling of the snow or firn layers. The following subsections explain how the variables making up Eq. 3.7 were calculated.

3.4.1.1 Incoming solar radiation

The most comprehensive function of the model is the calculation for incoming solar radiation where several factors determine the amount of solar radiation impinging on the Earth's surface. These include the top-of-atmosphere radiation; the slope aspect and gradient of the grid cell; the shading, angle of incidence, reflection and obstruction of the sky by the surrounding terrain; and the diffusivity and transmissivity of the sky. The model uses the grid, cloud fraction, air pressure and the time-step to calculate these variables.

Initially, incoming shortwave radiation at the surface without corrections, I, is formulated using the general equation presented by Klok and Oerlemans (2002):

$$I = I_0 (\cos Z) T_R T_g T_w T_{as} T_{cl} \tag{3.8}$$

where I_0 denotes the radiative flux at the top of the atmosphere on a surface normal to the sun's rays (i.e. incident radiation); Z is the solar zenith angle; T_R and T_g are Rayleigh scattering (R) and gaseous absorption (g) transmission coefficients; T_w is water vapour attenuation; T_{as} represents the transmission coefficient for aerosol attenuation; and T_{cl} is the cloud factor.

I_0 and Z are presented in the work done by Iqbal (1983) and Meyers and Dale (1983). In the equation, the changes in distance between the earth and sun throughout the year are taken into account, with the changes in I_0 being computed using the formula from Meyers and Dale (1983):

$$I_0 = 1353\, Wm^{-2}\{1 + 0.034 * \cos[2\pi\,(J_d - 1)/365]\} \tag{3.9}$$

where J_d is the Julian day and Z is calculated by:

$$Z = \cos^{-1}(\sin\gamma \sin\delta + \cos\gamma \cos\delta \cos H) \tag{3.10}$$

where γ is the latitude, δ represents the declination angle, and H the hour angle. Although Eq. 3.10 is valid for monochromatic radiation, by accounting for absorption and scattering within different spectral bands, it can be applied in a broad-band parameterized model (Atwater & Ball 1981; Meyers & Dale 1983).

The transmission coefficients T_R and T_g are calculated using the expression from Atwater and Brown (1974):

$$T_R T_g = 1.021 - 0.084 * [m(949p * 10^{-5} + 0.051)]^{1/2} \tag{3.11}$$

where p is the surface pressure (kPa), and m denotes the optical air mass at given pressure of 101.3 kPa:

$$m = 35(1224cos^2 Z + 1)^{-1/2} \tag{3.12}$$

T_w is used to calculate the broad-band transmission for water vapour attenuation and is expressed by (McDonald 1960):

$$T_w = 1 - 0.077(um)^{0.3} \tag{3.13}$$

where u represents the precipitable water vapour estimated from the surface dew point and is calculated using the equation from Smith (1966):

$$u = exp[0.113 - \ln(\lambda + 1) + 0.0393T_d] \tag{3.14}$$

where λ is a constant derived empirically for latitude and season, and T_d denotes the daily average dew point (°F). Aerosol attenuation, T_{as}, is complex due to the strong influence of other atmospheric components, however, using a simplified term from Houghton (1954) can be represented by:

$$T_{as} = k^m \tag{3.15}$$

where k is the aerosol transmissivity constant (0.97) derived for clear sky conditions, and m represents the optical air mass.

Topographic shading for each grid cell is determined every half hour using a method after Dozier and Frew (1990) to improve the accuracy in the calculation of direct solar radiation, with the final values being averaged to obtain 3-hourly estimates (Van Pelt et al. 2012). The shortwave radiation is then split into a direct and diffuse (i.e. shaded grid cells that only receive diffuse radiation) component. The direct (f_{dir}) and diffuse (f_{dif}) shortwave radiation are solved using the equations from Oerlemans (1992):

$$f_{dir} = 0.2 + 0.65(1 - n) \tag{3.16}$$

$$f_{dif} = 1 - f_{dir} = 0.8 - 0.65(1 - n) \tag{3.17}$$

where n is the fractional cloud cover.

The cloud factor, T_{cl}, which was used to calculate the transmissivity after cloud absorption and/or scattering was expressed as (Greuell et al. 1997):

$$T_{cl} = 1.0 - 0.128n - 0.346n^2 \tag{3.18}$$

Where again n is the fractional cloud cover.

3.4.1.2 Reflected shortwave radiation

The reflected or outgoing shortwave radiation is determined using a parameterisation developed by Oerlemans and Knap (1998) which uses the albedo of each grid cell. The model uses constants for albedo of fresh snow (0.853), firn (0.55), and ice (0.25) which is governed by snow depth and time since the last snowfall event. The glacier albedo, α, at day (i) is a function of snow depth and is expressed as (Oerlemans & Knap 1998):

$$\alpha^{(i)} = \alpha_{snow}^{(i)} + \left(\alpha_{ice} - \alpha_{snow}^{(i)}\right) exp\left(-\frac{d}{d^*}\right) \tag{3.19}$$

where $\alpha_{snow}^{(i)}$ is the albedo of snow, α_{ice} is the albedo of ice, d represents the snow depth (mm w.e.), and d^* is the characteristic scale for snow depth (11 mm w.e.) which was estimated by multiplying the depth scale identified by Oerlemans and Knap (1998) and a snow density of 350 kg m^{-3} (Klok & Oerlemans 2002). The snow albedo is controlled by the time since the last snowfall event and is calculated using the equation (Oerlemans & Knap 1998):

$$\alpha_{snow}^{(i)} = \alpha_{firn} + \left(\alpha_{frsnow} - \alpha_{firn}\right) exp\left(\frac{s-i}{t^*}\right) \tag{3.20}$$

where α_{firn} is the albedo of the firn, α_{frsnow} denotes the fresh snow albedo, s is the time since the last snowfall event (in days), i represents the actual time (in days), and t^* is a time-scale (21.9 days).

3.4.1.3 Longwave radiation

The incoming longwave radiation, L_{in}, is determined by cloud cover, air temperature and specific humidity; and is based on the Stefan-Boltzmann Law:

$$L_{in} = \varepsilon \sigma T_a^4 \tag{3.21}$$

where ε is the emissivity of the sky, σ represents the Stefan-Boltzmann constant (5.67×10^{-8}), and T_a is the air temperature. The cloud cover affects the emissivity of the sky which is computed using a parameterization discovered by Konzelmann et al. (1994) for Greenland:

$$\varepsilon = \varepsilon_{cs}(1 - n^p) + \varepsilon_{cl} n^p \tag{3.22}$$

where ε_{cs} represents the clear-sky emissivity, n is the cloud cover, p denotes an exponent (2), and ε_{cl} is the cloud emissivity constant (0.990). The clear-sky emissivity is determined by the concentration of greenhouse gases, water vapour pressure (e_a) and the air temperature:

$$\varepsilon_{cs} = 0.23 + b\left(\frac{e_a}{T_a}\right)^{1/8} \tag{3.23}$$

where b is a constant (0.447). The constants and exponent were adopted from the work done by Van Pelt et al. (2012). The calculation does not, however, account for longwave radiation emitted or obstructed from the surrounding terrain.

The calculation for outgoing longwave radiation, L_{out}, is also based on the Stefan-Boltzmann Law and assumes snow and ice emit as a black body ($\varepsilon = 1$) in the infrared:

$$L_{out} = \sigma T_{surf}^4 \tag{3.24}$$

where T_{surf} is the calculated surface temperature from surface energy flux (2.4.1.5).

3.4.1.4 Turbulent heat fluxes

The sensible heat flux, Q_{sens}, and the latent heat flux, Q_{lat}, otherwise known as the turbulent heat fluxes, are governed by the temperature and vapour pressure gradients between the atmosphere and glacier surface. The sensible heat flux represents the energy transfer of the atmosphere and is calculated using air temperature; while the latent heat flux expresses the energy released or consumed during a phase change (i.e. condensation, evaporation, sublimation, or re-sublimation) and is determined using the potential temperature lapse rate and vapour pressure. The turbulent heat fluxes are computed using the equations presented in Oerlemans and Grisogono (2002):

$$Q_{sens} = \rho_a c_p \frac{C_{kat} + C_b}{2}\left(T_a + T_{surf}\right) \tag{3.25}$$

$$Q_{lat} = -0.622 \rho L_{v/s} \frac{C_{kat} + C_b}{2}\left(\frac{e_a - e_{surf}}{p}\right) \tag{3.26}$$

where ρ_a represents the air density; c_p is the specific heat of dry air (1005.7 J kg^{-1} K^{-1}); C_b is the background turbulent exchange coefficient (0.0028); $L_{v/s}$ denotes the latent heat of vaporisation ($L_v = 2.5 \times 10^{-6}\, J\, kg^{-1}$) or sublimation ($L_s = 2.83 \times 10^{-6}$) when the surface temperature is below the melting point; C_{kat} signifies the katabatic turbulent exchange coefficient; e_a is the vapour

pressure at a suitable level in the atmosphere; e_{surf} is the saturated vapour pressure of the surface temperature above the ice; and p represents the reference air pressure ($10.15 \times 10^4\ Pa$). The variable e_{surf} is determined using the Clausius-Clapeyron equation to estimate the vapour pressure:

$$e_{surf} = e_0 exp\left(L_s/R/273.15\left(1 - 273.15/T_{surf}\right)\right) \tag{3.27}$$

where e_0 is the vapour pressure at 0°C constant ($610.5\ Pa$) and R represents the specific gas constant of water vapour ($462\ J\ kg^{-1}$). C_{kat} is calculated using the work from Oerlemans and Grisogono (2002):

$$C_{kat} = k\left(T_a - T_{surf}\right)\left(\frac{g_0}{T_0 \gamma Pr}\right)^{1/2} \tag{3.28}$$

where k represents an empirical constant (0.0004); g_0 is gravity; T_0 is the reference temperature ($273.15\ K$); γ denotes the background potential temperature lapse rate; and Pr the turbulent Prandtl number (5). On extremely warm days, γ can be negative resulting in the inability to calculate C_{kat}; in such cases, a lower limit of 0.0015 K m^{-1} is defined for γ. Additionally, warm days result in the largest C_{kat} values as there is a large temperature difference between the atmosphere and the glacier surface and the potential temperature gradient is frequently small (Klok & Oerlemans 2002). This causes glacier winds to develop and the generation of turbulence. Concurrently, turbulence is generated from the large-scale wind field that is explained by the background turbulent exchange coefficient C_b.

3.4.1.5 Sensible heat flux by rain

The heat supplied by rain, Q_{rain}, is dependent on precipitation and air temperature and can be expressed as (Bougamont et al. 2005):

$$Q_{rain} = \rho_w c_p R(T_a - T_0) \tag{3.29}$$

where ρ_w represents the density of water ($1000\ kg\ m^{-3}$), c_p is the specific heat of water ($4187.0\ J\ kg^{-1}\ K^{-1}$), R signifies the rainfall rate, T_a is the air temperature, and T_0 denotes the surface temperature ($273.15\ K$). Within the energy budget, the heat supplied by rain falling onto a surface with a lower temperature is usually a minor contribution and is negligible when compared with net radiation (Van Pelt et al. 2012; Van Pelt et al. 2016).

3.4.1.6 Glacier heat flux and surface temperature

The glacier heat flux is extrapolated from the uppermost snow/ice layers and the surface temperature (Van Pelt et al. 2012). Therefore, this variable represents the conduction between the underlying snow/ice and the surface temperature. Depending on this near-surface temperature gradient, the variable can either be positive or negative (Van Pelt et al. 2012; Van Pelt et al. 2016).

3.4.1.7 Snow accumulation

Snow accumulation is determined by the amount of snowfall, and does not take into account redistribution or accumulation of snow by wind drift or avalanching (Klok & Oerlemans 2002). If

precipitation occurred at a time step (Section 3.2.5), the precipitation rates for each grid cell were calculated by applying a dimensionless altitudinal gradient (0.00313) and correction factor (2.2). Snowfall and rain were differentiated using a threshold temperature of 1.5 ^{0}C; with a linear conversion from rain to snow between air temperatures of 2.5 and 0.5 ^{0}C (Van Pelt et al. 2016).

3.4.2 Subsurface model

The subsurface model simulates the evolution of vertical profiles of temperature, density and water content using the energy and mass exchange at the surface as an upper boundary condition (Van Pelt et al. 2012; Van Pelt et al. 2016). Greuell and Konzelmann's (1994) SOMARS model was coupled to a distributed energy balance model when it was initially developed to study mass balance at the Swiss ETH (Federal Institute of Technology) camp in Greenland (Greuell & Konzelmann 1994). Following this, it was later it was tested in West Greenland (Bougamont et al. 2005), and as well as by Reijmer and Hock (2008) to study internal accumulation on Storglaciären, Sweden. More recently, it has been extensively applied to study mass balance and firn evolution in Svalbard (Christianson et al. 2015; Van Pelt et al. 2012; 2013; 2014; 2016; Van Pelt & Kohler 2015; Vega et al. 2016).

The model solves the subsurface temperature evolution caused by the refreezing of percolating or stored water using the thermodynamic equation presented in Van Pelt et al. (2012; 2016):

$$\rho c_p(T)\frac{\partial T}{\partial t} = \frac{\partial}{\partial z}\left(\kappa(\rho)\frac{\partial T}{\partial z}\right) + \frac{RL}{d} \tag{3.30}$$

where ρ denotes the layer density; $c_p(T)$ is the heat capacity of snow or ice; T denotes the layer temperature; t is time; z is the vertical coordinate; $\kappa(\rho)$ symbolises the effective conductivity; R is the refreezing rate ($kg\ m^{-2}\ s^{-1}$); L serves as the latent heat of melting ($3.34 \times 10^5\ J\ kg^{-1}$); and d is the layer thickness. The initial term on the right hand side of Eq. 3.30 accounts for heating by a vertical diffusive heat flux, while the second term in parenthesis describes heat production by freezing water within a layer (Van Pelt et al. 2016). Effective conductivity, $\kappa(\rho)$, represents the energy exchange through convection, conduction, vapour and radiation diffusion processes (Reijmer & Hock 2008). It is a function of snow properties and density, and can be expressed with a quadratic equation taken from Sturm et al. (1997):

$$\kappa(\rho) = 0.138 - 1.01 * 10^{-3}\rho + 3.233 * 10^{-6}\rho^2 \tag{3.31}$$

The thermal capacity of snow or ice, $c_p(T)$, calculates the heat needed for a unit of mass to rise one unit of temperature at constant pressure, c_p, and can be expressed as (Yen 1981):

$$c_p(T) = 152.2 + 7.122T \tag{3.32}$$

The model neglects any shortwave radiation penetration and subsequently melting within the subsurface. Therefore, percolation of surface melt water and rain water are the only source of water in the snow pack (Van Pelt et al. 2012).

The model solves for the time-evolution of densification ($\frac{\partial \rho}{\partial t}$), taking into consideration refreezing and gravitational densification of the snow ($G(\rho, T)$) using the equation taken from Ligtenberg et al. (2011):

$$\frac{\partial \rho}{\partial t} = G(\rho, T) + \frac{R^*}{d} \tag{3.33}$$

where $G(\rho, T)$ represents the gravitational densification rate, R^* is the universal gas constant, and d is the layer thickness. $G(\rho, T)$, is based on *in-situ* measurements of Antarctic snow compaction and was adjusted by Ligtenberg et al. (2011) after Arthern et al. (2010). It can be expressed as (Arthern et al. 2010):

$$G(\rho, T) = C(b) b g_0 (\rho_{ice} - \rho) exp\left(-\frac{E_c}{R^* T} + \frac{E_g}{R^* T_{avg}}\right) \quad (3.34)$$

where b represents the accumulation rate ($mm\ a^{-1}$), g_0 is the gravitational acceleration, ρ_{ice} denotes the density of ice ($917\ kg\ m^{-3}$), R^* is the universal gas constant, T represents the layer temperature, E_c ($60\ kJ\ mol^{-1}$) and E_g ($42.4\ kJ\ mol^{-1}$) signify the activation energies related to creep by lattice diffusion and grain growth, and T_{avg} is the temporal mean subsurface temperature. T_{avg} is calculated every model time-step by taking the mean subsurface temperature of the previous year (Van Pelt et al. 2012). Ligtenberg et al. (2011) modified the gravitation densification formula to include C which is dependent on the accumulation rate b, and can be expressed depending on the critical density value:

$$C(b) = \begin{cases} 1.415 - 0.147\ log(b),\ if\ \rho\ < 550\ kgm^{-3} \\ 2.335 - 0.228\ log(b),\ if\ \rho\ \geq 550\ kgm^{-3} \end{cases} \quad (3.35)$$

A bucket system is used to simulate the vertical transport and refreezing of water (Greuell & Konzelmann 1994; Reijmer & Hock 2008; Van Pelt et al. 2012; Van Pelt et al. 2016). Initially, the temperature profile is calculated excluding the effects of melt or refreezing, and only then the water content and the consequence of melt and refreezing on the temperature profile are computed (Reijmer & Hock 2008). If a snow or firn layer is present, surface water originating from ice melt and rainfall will be added to the water content and percolate downwards. If the subsurface temperature is below 0°C, refreezing will occur, consequently raising the subsurface temperatures and densities which cannot increase above melting point or exceed the density of ice respectively (Reijmer & Hock 2008; Van Pelt et al. 2012). These constraints, together with the available amount of water content and available pore space in the snow or firn layer limit the amount of refreezing. After the refreezing calculation, a small amount of water is retained while the remaining water continues to percolate downwards into the next layer as a result of gravity. The small amount of water retained is known as irreducible water and is stored by capillary and adhesive forces (Reijmer & Hock 2008).

The irreducible water content in a layer, θ_{mi}, is the fraction of mass of irreducible liquid water to the total mass of the layer, and can be expressed as (Schneider & Jansson 2004):

$$\theta_{mi} = 0.0143 \exp(3.3\Phi) \quad (3.36)$$

where Φ is the porosity which represents the ratio of pore space to the total volume of the snow layer. The remaining water content may continue to percolate downwards through consecutive vertical layers until an impermeable ice layer is reached forming a layer of slush water (Reijmer & Hock 2008; Van Pelt et al. 2012). The available slush water, $S(t)$, fills all the remaining pore spaces before runoff occurs according to a single time-scale where standing slush water decays exponentially, and can be expressed as:

$$S(t) = 1.0 / \left(1.0 + \frac{\Delta t}{t^*}\right) * S \quad (3.37)$$

where Δt represents the model time-step and t^* denotes the time-scale constant that controls runoff (0.001 days) and S is the sum of slush water. The time-scale constant ensures that runoff of slush water is almost instantaneous which would be characteristic of a mountain glacier, where standing water has little chance to accumulate and instead runoff occurs through englacial channels, cracks, moulins, and/or crevasses.

3.5 Numerical setup

The coupled model was forced with 3-hourly climate data and was performed on a grid for the period 1 November 2013 to 30 September 2017. Two separate grids were used for the calibration and numerical experiments and their details are displayed in Table 3.2. For the calibration, a 100 m grid was used to allow for faster model runs which required less computing power. The numerical experiments performed in this dissertation used a higher resolution grid for better visualisation of surface and subsurface process.

Table 3.2: Details of grids used in the calibration and numerical experiments of the model.

Property	Calibration	Numerical experiments
Grid resolution (m)	100	25
Grid cells	107x107	428x428
Glacier grid cells	2428	38950

Prior to the start of the model run, in which the surface energy balance and subsurface profiles were simulated at 3-hourly time intervals, the topographical grid was imported together with the mask that defines the glacier area. The mask was derived from the glacier outline. The glacier geometry did not change over time as this would require further coupling of an ice dynamic model; however, any influence due to mass balance-height feedback will only have an affect over lengthier time periods (Van Pelt et al. 2012). Additionally, no horizontal movement was considered which would translate to a slight potential offset with increasing depth of the vertical profiles, however, this offset was deemed negligible near the surface.

At the start of each 3-hourly time-step, air temperature, relative humidity, and air pressure were extrapolated for the entire glacier by multiplying their respective lapse rates with the height difference between the meteorological station and each grid cell (Section 3.2.2). Cloud cover was considered to be uniform across the entire glacier. For precipitation, a correction factor of 2.2 was used in conjunction with a dimensionless precipitation gradient of 0.00313 which was multiplied with the height difference between the meteorological station and the grid cell. Using these climate parameters, several other climatic fields were then derived; these included the differentiation between snow and/or rainfall, annual snow accumulation, time since the last snowfall event, vapour pressure, specific humidity, air density, and potential temperature lapse rate.

The climate parameters were then used to solve the energy balance equation (Eq. 3.7) by computing the fluxes for incoming shortwave radiation (Eq. 3.8), outgoing shortwave radiation (Eq. 3.19), incoming longwave radiation (Eq. 3.21), sensible heat flux (Eq. 3.25), latent heat flux (Eq. 3.26), heat supplied by rain (Eq. 3.29), and the glacier heat flux. An iterative process was used to solve for the energy budget, and as previously noted, in a case where surface temperature was above the melting point, the surface temperature was set to 237.15 K and any excess energy was used for melting (Section 3.4.1).

The subsurface model utilised a moving grid of 200 vertical layers; which were added or removed at the surface and/or base depending on the surface mass fluxes. The moving grid prevents the averaging of layer properties, and ensures they do not suffer from numerical diffusion as would be the case with a fixed grid (Van Pelt et al. 2016). The top 15 m of the subsurface consisted of 150 layers with a thickness of no more than 10 cm; there after layer thickness doubled after every 20 layers until the 200th layer was reached. Therefore, maximum subsurface depth computed was 20 m. Following an increase in surface height after snowfall and/or riming, layers shift down after the first layer exceeds the maximum thickness (i.e. 10 cm). Consequently, a decrease in surface height after melt and/or sublimation results in the upward shift of layers when the first layer is completely removed. The vertical layers were then updated for gravitational densification, which affected layer density, thickness, and irreducible water storage. The subsurface model then updated the snow and firn temperatures after heat diffusion or conduction. For heat diffusion, time-steps of one hour were used; this assured stability and convergence of heat in the uppermost layers, whilst in the lower boundary, the vertical gradient was zero and no heat transport can occur (Van Pelt et al. 2012).

3.6 Calibration

Calibration of the model was accomplished by using past studies and observations from Abramov glacier. The formulations within the model contain several poorly-constrained variables; therefore literature and observations provided a valuable source of information that can reduce the uncertainty associated with these parameters (Table 3.3).

Table 3.3: Summary of model parameters used for the calibration of the coupled model.

Parameter	Symbol	Value/Expression	Source
Aerosol transmissivity constant (-)	k	0.97	Van Pelt et al. (2012)
Transmission coefficient for cloud cover (Eq. 3.18)	T_{cl}	$1.0 - 0.128n - 0.346n^2$	Van Pelt et al. (2012)
Cloud emissivity constant (-)	ε_{cl}	0.990	Van Pelt et al. (2012)
Constant in the formulation of clear-sky emissivity (Eq. 3.23)	b	0.447	Van Pelt et al. (2012)
Background turbulent exchange coefficient (-)	C_b	0.0028	Van Pelt et al. (2012)
Albedo of ice constant (-)	α_{ice}	0.25	Adapted from Barandun et al. (2015)
Albedo of fresh snow constant (-)	α_{frsnow}	0.835	Van Pelt et al. (2012)
Albedo of firn constant (-)	α_{firn}	0.55	Van Pelt et al. (2012)
Temperature lapse rate constant (°C km^{-1})	L	-5	Kislov (1982)
Snow/rain transition threshold (°C)	-	1.5	Klok and Oerlemans (2002)
Altitudinal precipitation gradient constant (-)	-	0.00313	Calibrated using ablation stakes
Precipitation correction factor constant (-)	-	2.2	Calibrated using ablation stakes

Simulated incoming solar radiation (S_{in}) was one of the parameters which required calibration; this can be accomplished by firstly tuning the aerosol transmissivity under clear-sky conditions (Eq. 3.15) and secondly determining the cloud transmissivity as a function of cloud cover (Eq. 3.18) (Van Pelt et al. 2012). The aerosol transmissivity constant (k) is used to solve for aerosol transmissivity and can range between 0.87-1.00 depending on the geographic location (Davies & McKay 1989). A value for k can be determined by comparing measured incoming shortwave radiation ($S_{in_{meas}}$) under clear-sky conditions to modelled S_{in}; conversely, a value of 0.97 was adopted for k after Van Pelt et al. (2012). The cloud fraction (n) was calculated using Eq. 3.4 by computing the ratio between $S_{in_{meas}}$ and the potential global radiation under clear-sky conditions ($S_{in_{cs}}$) to determine the transmission coefficient for cloud cover (T_{cl}). The expression used for Eq. 3.4 was derived for an Alpine glacier (Greuell et al. 1997). Whilst in the coupled model a similar expression was used (Eq. 3.18) for the calculation of T_{cl} that was adopted from Van Pelt et al. (2012). A comparison between both equations indicated that T_{cl} in Eq. 3.18 was less dependent on n; possibly due to associated optical depth and geographical differences in the predominant cloud type (Van Pelt et al. 2012). Further tuning of T_{cl} may be required to improve the modelled S_{in} at Abramov because Eq. 3.18 is more suited to a glacier in Svalbard. In this study, $S_{in_{meas}}$ from the AWS was used to derive T_{cl} in Eq. 3.4 and estimate n which was then used as an input into the coupled model; furthermore, n was then used to calculate T_{cl} in the model (Eq. 3.18). This process reduces the effectiveness of using $S_{in_{meas}}$ to calibrate the model and instead values and expressions were adopted from Van Pelt et al. (2012).

The modelled incoming longwave radiation (L_{in}) is another parameter that can be calibrated by tuning the values of the constants for cloud emissivity (ε_{cl}) which is used to calculate the emissivity of the sky (ε) in Eq. 3.22, and b which is applied in the formulation of clear-sky emissivity (ε_{cs}) in Eq. 3.23. In Van Pelt et al. (2012), inconsistencies in modelled L_{in} were reduced with the use of measured L_{in} values by studying cloud-free and overcast conditions. By comparing simulated and measured L_{in} for overcast conditions (cloud fraction > 95 %) a value for ε_{cl} was determined; additionally, by comparing modelled and measured L_{in} for clear-sky conditions (cloud fraction < 5 %) a value for b was established. For this study, as the measured incoming L_{in} at Abramov suffers from numerous data gaps a value of 0.990 for ε_{cl} and 0.443 for b were adopted from Van Pelt et al. (2012). These values were similar to the estimated values of 0.984 and 0.433 for ε_{cl} and b for Morteratsch glacier in Switzerland (Klok & Oerlemans 2002).

The calculations for the turbulent heat fluxes include a background exchange coefficient (C_b) that is used to explain the turbulence generated from the large-scale wind field (Klok & Oerlemans 2002). C_b can be calibrated by ensuring an agreement between observed melt and calculated melt at a defined location; and can be done independently of other tuning parameters (Klok & Oerlemans 2002; Van Pelt et al. 2012). A value of 0.0028 was adopted for C_b from Van Pelt et al. (2012). It was estimated by matching observations from a Sonic Ranger site with modelled snow and ice melt

As noted in Barandun et al. (2015), the Abramov glacier carries a high concentration of surface impurities; thus reducing the albedo of the ice exposed in the ablation zone. Consequently, the albedo for ice (α_{ice}) was constrained to 0.25. A fresh snow albedo (α_{frsnow}) of 0.835 and firn albedo (α_{firn}) of 0.55 was adopted from Van Pelt et al. (2012). A constant temperature lapse rate of -5 °C km^{-1} was used as reported by Kislov (1982), however, Barandun et al. (2015) applied a value of -4.8 °C km^{-1} that was established from direct measurements after Glazirin et al. (1993).

The air temperature determines the relative quantity of liquid and solid precipitation in the model. A threshold air temperature ($T_{s/r}$) was used to define the point where precipitation is assumed to be half snow and half rain. A $T_{s/r}$ value of 1.5 °C (274.65 K) was adopted from Klok and Oerlemans (2002). In terms of total precipitation, the relative fraction of rainfall increases linearly around this threshold from 0 % at $T_{s/r} - 1\,K$ to 100 % at $T_{s/r} + 1\,K$; whereas on the contrary the relative fraction of snowfall increases from 0 % at $T_{s/r} + 1\,K$ to 100 % at $T_{s/r} - 1\,K$.

The spatial distribution of precipitation was calibrated using the measurements from the ablation stake network (Fig. 3.1) at Abramov. A linear regression between the modelled mass balance and the stake measurements from 2014 to 2017 was used to determine an altitudinal precipitation gradient of 0.00313 and a precipitation correction factor of 2.2 (Fig. 3.7) (Appendix B). This equates to a mean annual precipitation gradient of 3.41 mm m^{-1} and a mean annual precipitation of 876 mm at 3627 m a.s.l.

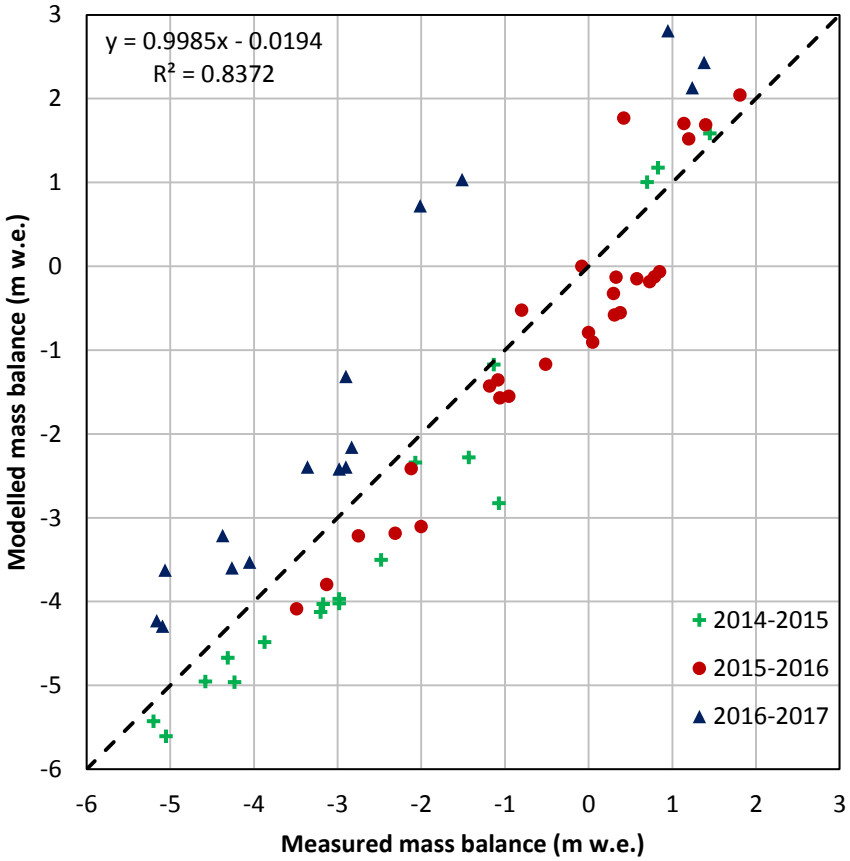


Figure 3.7: Scatter plot of modelled and measured mass balance estimates from stake readings for the period 2014-2017.

3.7 Initialisation

For realistic simulation of subsurface conditions in the beginning years of a model run, initialised subsurface temperature, density, and water content conditions are required (Van Pelt et al. 2012; Van Pelt & Kohler 2015). These subsurface properties are heavily dependent on the history of the subsurface and surface conditions (Van Pelt et al. 2012). Therefore, a spin-up procedure was performed whereby the model was looped eight times over the year 2014 to generate these initial conditions. The spin-up procedure allows for the development of the snow and firn pack; while at the same time enabling density, temperature and liquid water storage to approach a consistent state with the mean surface forcing for the year 2014. The final output of the initialisation process serves as the initial conditions for the model run starting 01 November 2013 to 30 September 2017.

Chapter 4

Results from the model run

A simulation from 01 November 2013 to 30 September 2017 was performed using the initialised subsurface profiles; and encompassed only three hydrological years from October 2014 to September 2017. Results pertaining to the spatial distribution of the mass and energy balance, and the subsurface are presented in this section. Furthermore, comprehensive overviews of modelled parameters are presented in Appendix C.

4.1 Mass balance

Figure 4.1 presents the mean annual mass balance and its evolution for the entire model run. For 2014-2017 (Fig. 4.1a), a mean annual mass balance of +0.94 m w.e. a^{-1} was simulated; consisting of +0.02 m w.e. a^{-1} for 2014-15 (Fig. 4.1b), +0.84 m w.e. a^{-1} for 2015-2016 (Fig. 4.1c), and +1.94 m w.e. a^{-1} for 2016-2017 (Fig. 4.1d) hydrological year respectively. Spatial variations in mass balance are predominantly caused by a combination of altitudinal differences between precipitation and air temperature, and spatial gradients in surface albedo and refreezing. The highest accumulation rates occur at high elevation on north facing slopes (approx. +4 m w.e. a^{-1}), while the highest ablation rates are at low elevations near the glacier terminus (approx. -7 m w.e. a^{-1}). The simulated equilibrium line altitude (ELA) was determined to be 4100 m a.s.l. for the entire period; with the highest annual ELA being roughly 4250 m a.s.l. for 2014-2015, and the lowest being about 3970 m a.s.l. for 2016-2017.

Figure 4.2 illustrates the spatial distribution of refreezing and runoff for Abramov glacier. Refreezing refers to melt and rain water that has infiltrated into the snow and firn pack and consequently refrozen to form ice lenses (Fig. 4.2a). Glacier-wide refreezing of subsurface water contributes +0.84 m w.e. a^{-1} and occurs predominantly above the modelled ELA (i.e. within the accumulation zone) where the presence of snow and firn allow for the downward percolation of water. The presence of refreezing varies with topographical differences and was less influenced by altitudinal differences above the ELA. At high elevation and north facing slopes, refreezing was lowest (+0.3 m w.e. a^{-1}) due to little melt; while refreezing was highest (+1.1 m w.e. a^{-1}) on south facing slopes where melt is the strongest.

Runoff refers to the flux of water from melt and rainfall leaving the glacier (Cogley et al. 2011). Figure 4.2b displays the spatial pattern of runoff that was not only produced by the melting of glacier ice, snow and firn, but also included rainfall. Results from the coupled model indicated that +1.85 m w.e. a^{-1} was removed by runoff through surface and subsurface (i.e. englacial channels) flows. The spatial pattern of runoff was governed predominantly by the altitudinal differences between air temperature and precipitation; and was highest below the ELA where the surface consists of glacier ice.

Figure 4.3 displays the mean monthly contribution that solid precipitation, refreezing, and melt have on the mass balance of Abramov. Solid precipitation positively contributed to the mass balance and was simulated to add +0.19 m w.e. $month^{-1}$ from 2013-2017; with a summer (April to September) mean of +0.20 m w.e. $month^{-1}$ and winter (October to March) mean of +0.19 m w.e. $month^{-1}$. Additionally, refreezing also added to the mass balance and was calculated to be +0.07 m w.e. $month^{-1}$ for the same period; with a summer and winter mean of +0.12 and +0.02 m w.e. $month^{-1}$ respectively. Conversely, melt removed mass from the glacier and was estimated to be -0.18 m w.e. $month^{-1}$; with a

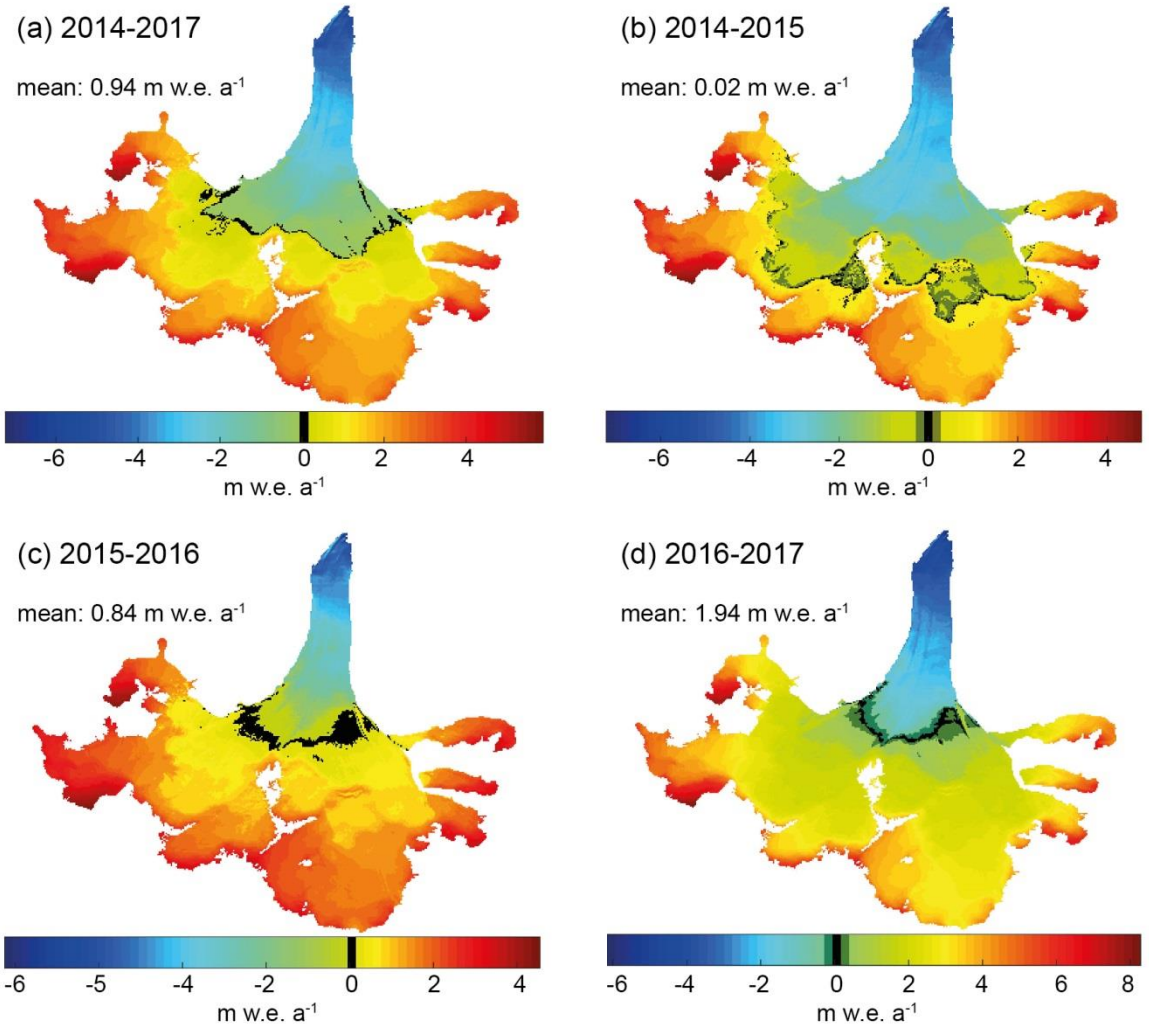


Figure 4.1: Spatial distribution of mean annual mass balance for the hydrological period 2014-2017 (a), 2014-2015 (b), 2015-2016 (c), and 2016 -2017 (d).

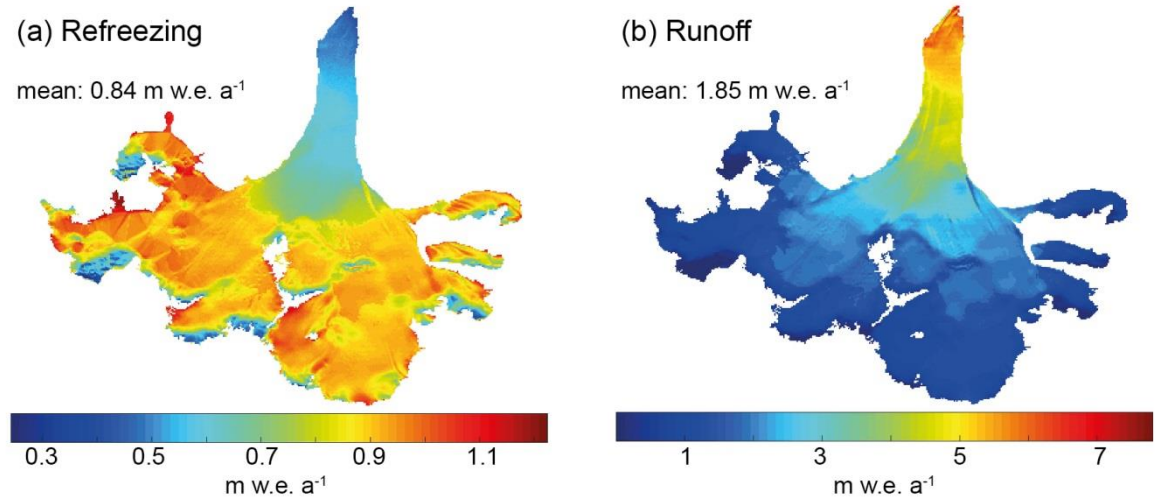


Figure 4.2: Spatial distribution of mean annual refreezing (a) and runoff (b) from November 2013 to September 2017.

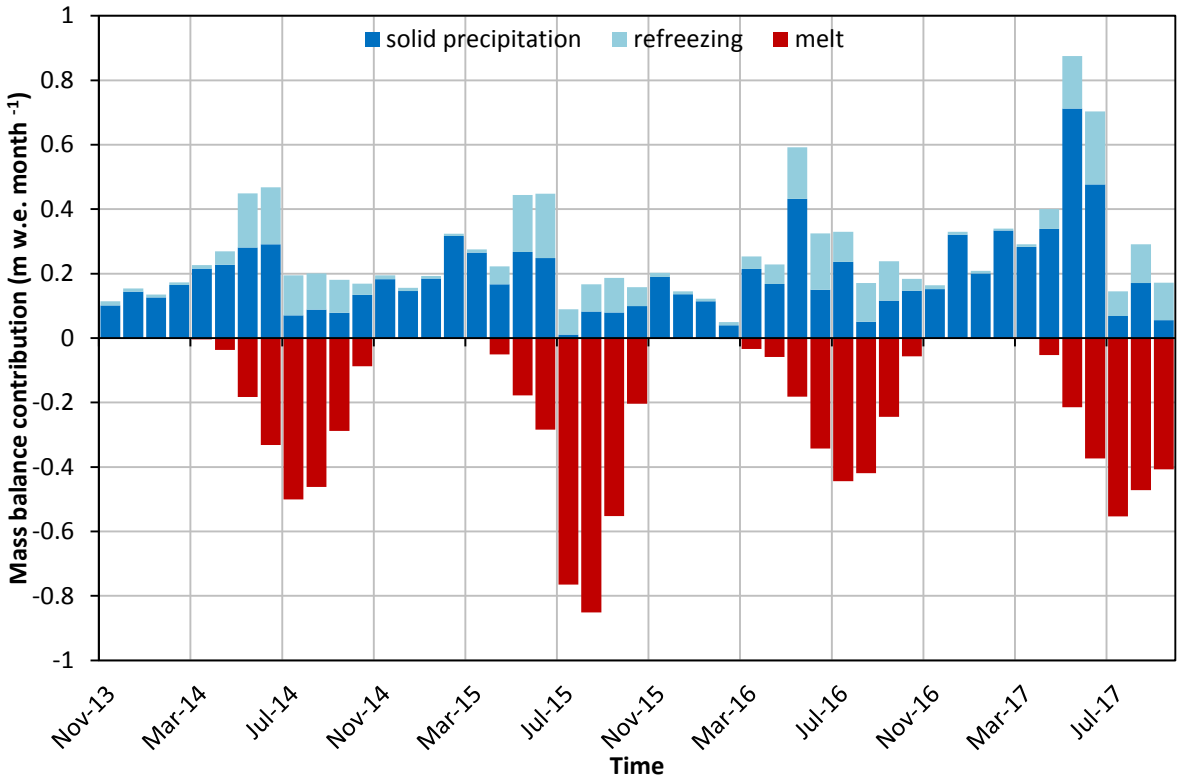


Figure 4.3: Glacier-wide mean monthly mass balance contribution of solid precipitation, refreezing and melt for the period November 2013 to September 2017.

summer mean of -0.34 m w.e. month^{-1} and winter mean of -0.02 m w.e. month^{-1}. Solid precipitation occurred throughout the year and is highest between February and June, and lowest between July and September, however there were some exceptions. Melt began every year in April and as a consequence, so did refreezing. Melt was strongest in July and August and was negligible in the winter months. Refreezing was most effective at the start of summer (April, May and June), and occurred as long as there was melt.

Figure 4.4 compares the fraction of precipitation that occurs as snowfall and rainfall, with the mean monthly air temperature for Abramov. From 2013 to 2017, it was simulated that 85.4 % of precipitation occurred in the form of snow; with rain making up the remaining 14.6 %. Snowfall accounted for 99.7 % of winter precipitation and 71.6 % of summer precipitation; and rain accounted for 0.3 % of winter precipitation and 28.4 % of summer precipitation. When compared with the monthly mean air temperature, snowfall was the dominant precipitation type (>85 %) when the mean air temperature was roughly +1.7 ºC and below; however, there were a few exceptions. The fraction of rainfall was highest (> 75 %) when mean monthly air temperatures were approximately greater than 5 ºC; which only occurred twice (July 2015 and 2017) for the period 2013-2017.

Figure 3.7 in Section 3.6 presented the results from the calibration process where stake measurements were used to constrain the precipitation correction factor and altitudinal precipitation gradient. The model results indicated a bias of +0.46 m w.e. as the model over estimates mass balance, especially for the period 2016-2017. The Mean Absolute Error (MAE) was 0.63 m w.e. and the Root Mean Squared Error (RMSE) was 0.72 m w.e. These errors were largely associated with the simulated mass balance being too positive in the accumulation area for 2014-2017 combined with the exceptionally positive 2016-2017 hydrological year.

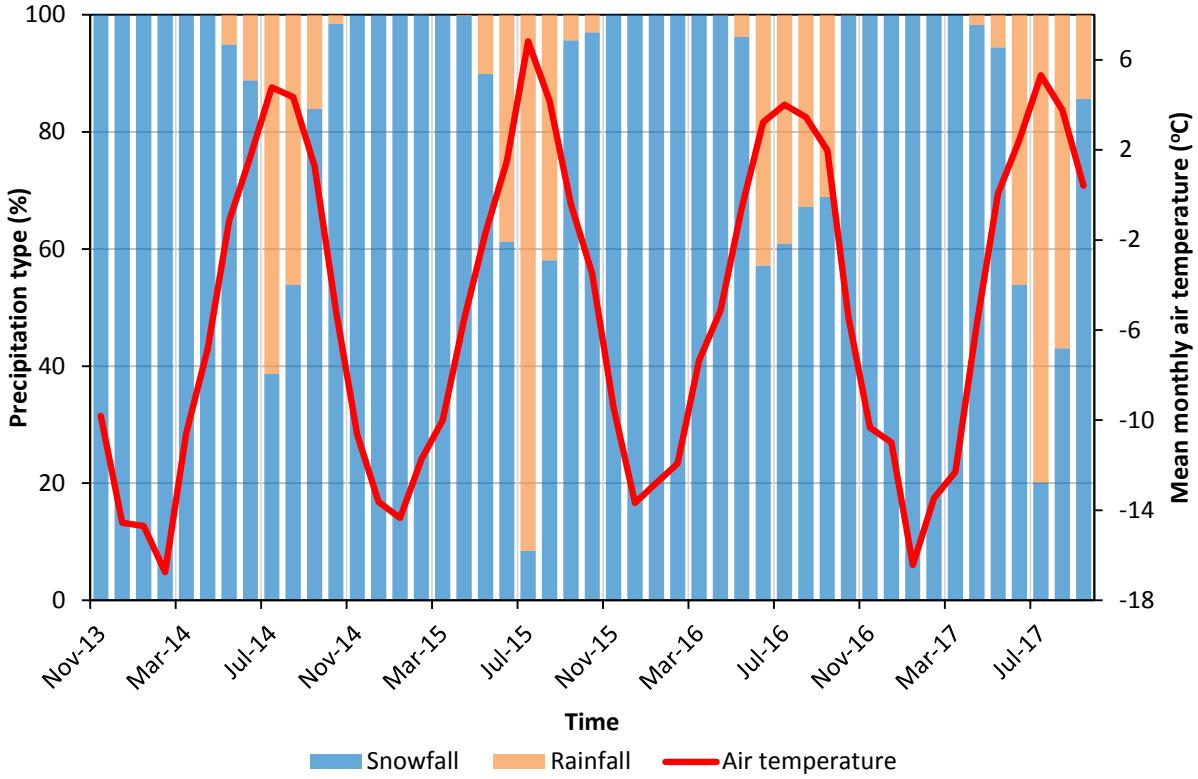


Figure 4.4: Glacier-wide comparison between the monthly fraction of snowfall and rainfall, and mean monthly air temperature for the period November 2013 to September 2017.

4.2 Energy budget

Figure 4.5 shows the spatial distribution that was simulated for the components, making up the energy budget, averaged over the period 2013-2017. Figure 4.5a displays the sum of all fluxes which represents the energy available for melting (Q_{melt}). The mean Q_{melt} was +22.85 W m^{-2} and was highest in the ablation zone and decreased with altitude. The net shortwave flux (Q_{sw}) contributed the most energy to the budget (mean: +49.22 W m^{-2}) and its spatial extent was controlled by the surface albedo, shading from the surrounding terrain, and the orientation and aspect of the terrain (Fig. 4.5b). Consequently, the highest values can be found at low elevations near the terminus (+110 W m^{-2}) and the lowest values at high elevations on north facing slopes (+15 W m^{-2}). The net longwave flux (Q_{lw}) acted as an energy sink (mean: -46 W m^{-2}) and its distribution only varied slightly with altitude (Fig. 4.5c). The most notable differences were found on the north facing slopes where the values are highest (-46 W m^{-2}) and south facing slopes where values are lowest (-62 W m^{-2}).

The sensible heat flux (Q_{sens}) made the second highest contribution to the energy budget (mean: +27.27 W m^{-2}) after Q_{sw} (Fig. 4.5d). Q_{sens} was highest at the terminus and on north facing slopes (+37 W m^{-2}); however, it generally decreased with altitude and was smallest on south facing slopes (+18 W m^{-2}). Conversely, the latent heat flux (Q_{lat}) removes energy available for melt but was rather small (mean: -3.66 W m^{-2}) (Fig. 5.4e). Q_{lat} was lowest at the terminus (-7 W m^{-2}) and increased with altitude. The glacier heat flux (Q_{ghf}) was positive (mean: +3.86 W m^{-2}); it was highest in the accumulation area (+3.5 to 6 W m^{-2}), and lowest in the ablation area and north facing slopes at high elevation (+1 W m^{-2}) (Fig. 4.5f).

Figure 4.6 plots the mean monthly surface energy balance components, illustrating the temporal changes associated with the summer (April to September) and winter (October to March) months for 2013-2017. Q_{sw} was the most dominant flux, and was highest during the summer (mean: +72 W m^{-2}) and lowest in winter (mean: +25.29 W m^{-2}) when the glacier was covered in fresh snow; thereby increasing the albedo. Q_{sens} was the second largest flux, however, in comparison there was minimal difference between summer (mean: +25.66 W m^{-2}) and winter (mean: +28.33 W m^{-2}). Finally, Q_{ghf} was the smallest of energy inputs, and was highest in summer (mean: +5.51 W m^{-2}) when melt begins to infiltrate the snowpack and refreezes releasing latent heat, and lowest in winter (mean: +2.13 W m^{-2}). The largest energy sink was Q_{lw}, with only a small variation between summer (mean: -55.05 W m^{-2}) and winter (mean: -51.90 W m^{-2}). Another energy sink was Q_{lat} which was strongest in the summer (mean: -5.58 W m^{-2}) and weakest in the winter (-1.75 W m^{-2}). Using Eq. 3.7 to calculate the sum of fluxes, a net input of energy means the surface temperature of the glacier is calculated to be above melting point; therefore the surface is set to 0°C and the excess energy is used to calculate Q_{melt}. Excess energy from the glacier-wide surface energy balance was highest in summer (mean: +43 W m^{-2}) and lowest during winter (mean: +2 W m^{-2}).

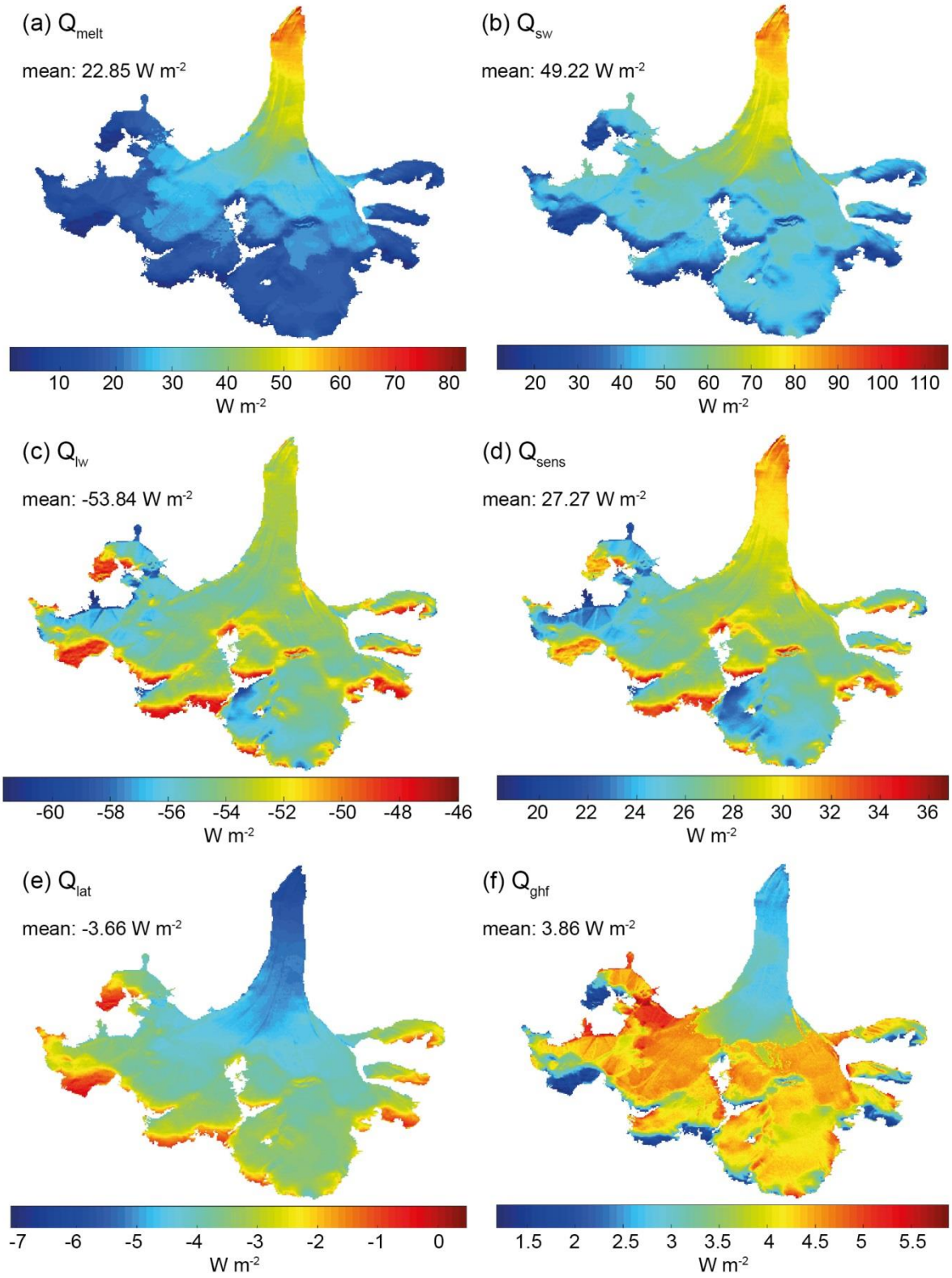


Figure 4.5: Spatial distribution of (a) melt energy (Q_{melt}), (b) net shortwave radiation (Q_{sw}), (c) net longwave radiation (Q_{lw}), (d) sensible heat flux (Q_{sens}), (e) latent heat flux (Q_{lat}), and (f) glacier heat flux (Q_{ghf}) averaged over the period 2013-2017.

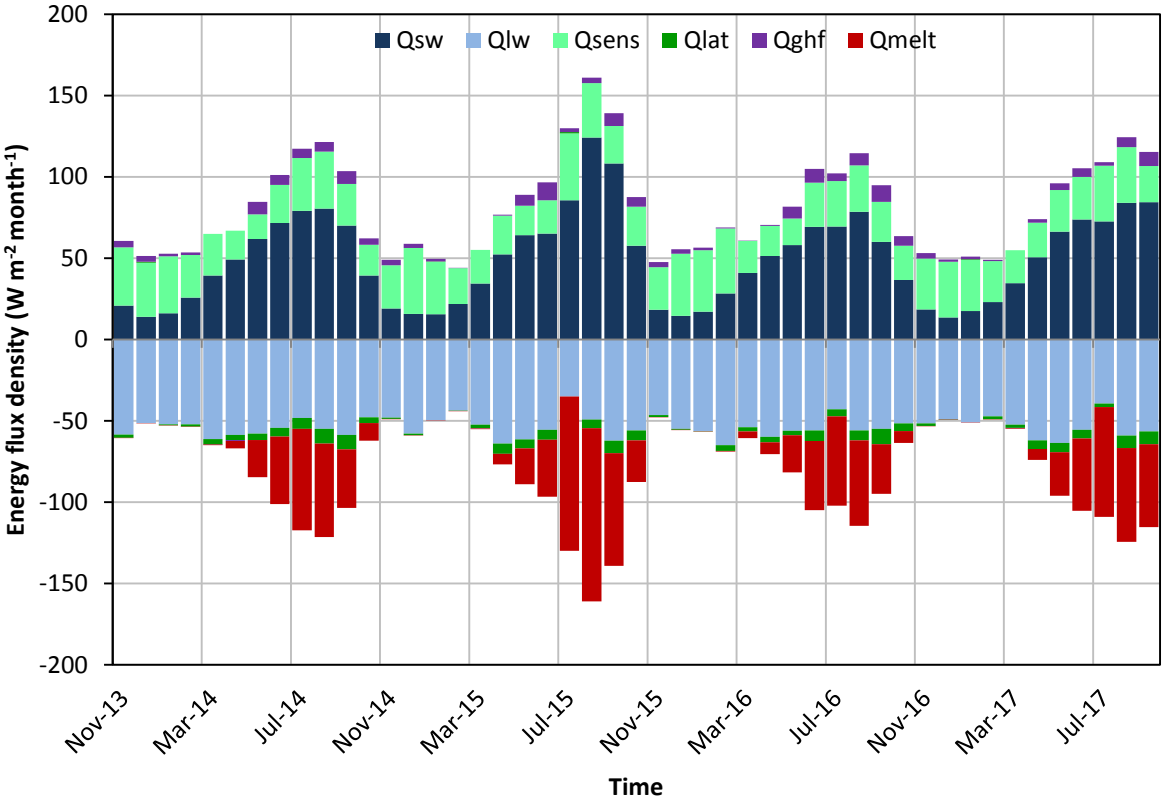


Figure 4.6: Glacier-wide mean monthly surface energy components for the period November 2013 to September 2017.

4.3 Subsurface variables

Figures 4.7a.l, b.1 and 4.1a.2, b.2 present the density and temperature evolution for the model run at the two ice core sites (C1 and C2). Both sites are located in the accumulation zone where the firn pack is present (Fig. 3.1). Figure 4.7a (1 and 2) corresponds to the location of ice core C1 situated 4238 m a.s.l.; and Figure 4.7b (1 and 2) corresponds to the location of ice core C2 located at 4385 m a.s.l. At both sites, their specific mass balance increased with snowfall events and decreased with summer melt.

At site C1, there was a net balance of approximately +13 m of snow from 2013-20174 (Fig. 4.7a.1). Generally, refreezing occurred close to the surface when melt started (i.e. April) causing rapid densification within the snowpack. As summer progressed, snowfall continued to add to the specific mass balance. Simultaneously, melt rates increased and melt water percolated deeper into the winter snowpack and firn before refreezing; increasing the overall density of the snowpack. The specific balance reached its peak (i.e. winter balance) in May-June before ablation removes mass from the glacier surface. With the start of the accumulation season, the density below the current year's summer surface began to increase with depth. Figure 4.6a.2 illustrates the temperature evolution near the glacier surface for the same time period. During winter, there was a strong temperature gradient between the air temperature (glacier-wide mean: -10.73 °C) and the temperate glacier surface (0 °C); causing the transfer of heat away from the surface and its cooling. The cold air temperatures penetrated to a depth of roughly 5 m below the surface by the end of winter; after which the refreezing of melt water caused the temperature to rise.

At site C2, there was a net balance of roughly +19 m of snow from 2013-2017; being situated at a higher elevation than C1 means it received more snowfall because of the altitudinal precipitation gradient (Fig. 4.7b.1). The seasonal process of refreezing followed a similar development to that described for ice core C1; however, there was more densification near to the surface. Figure 4.7b.2 displays the subsurface temperature evolution at C2 which behaved in a similar way to C1.

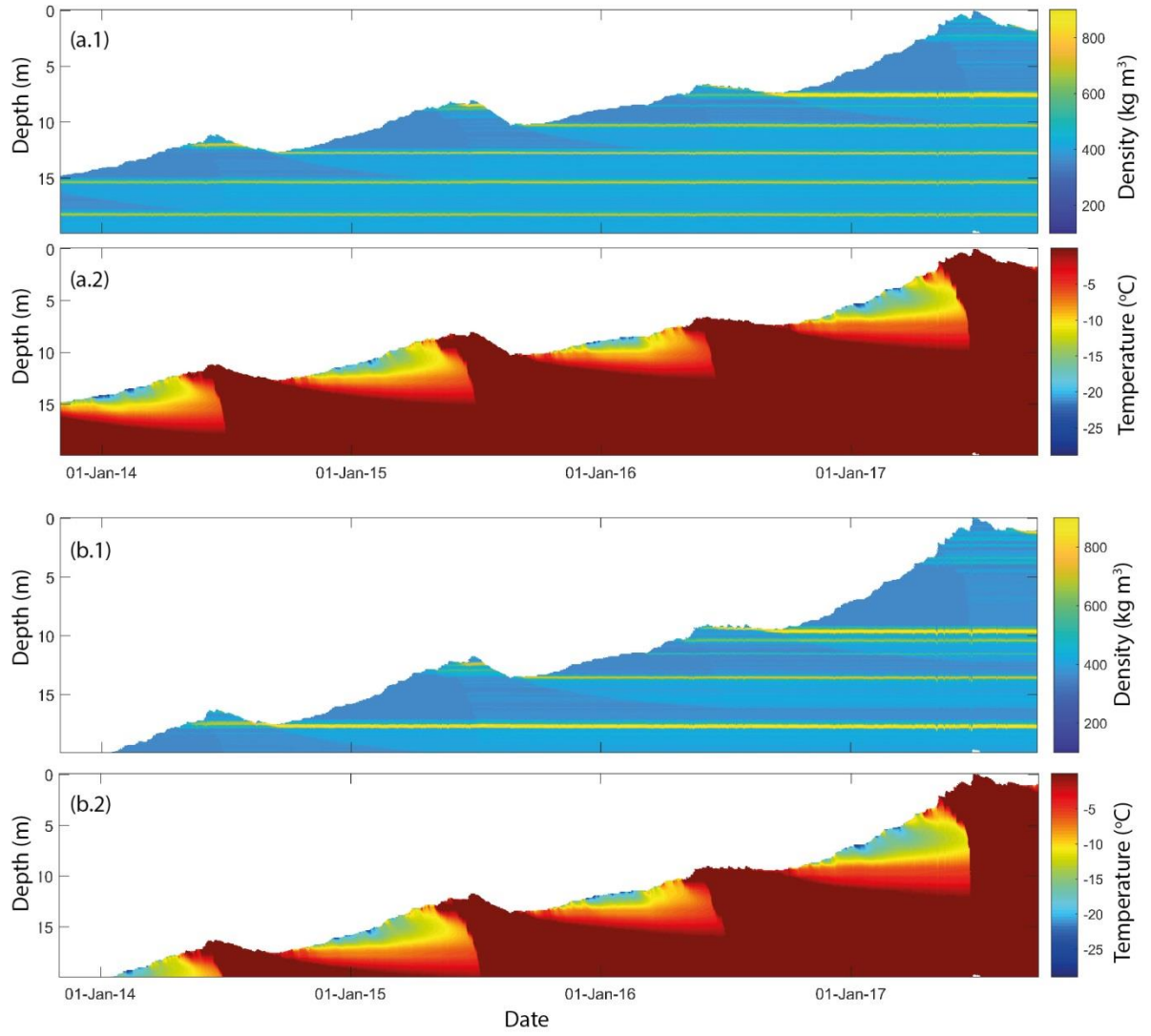


Figure 4.7: Subsurface densities and temperature evolution at the location of ice cores C1 (a) and C2 (b) for 2014-2017.

A final comparison between the modelled (M1 and M2) and observed (C1 and C2) density profiles was made (Figure 4.8). The ice cores were collected during a winter expedition in January 2018; as a result the modelled density profiles were output for January 2017. Only the top 15 m of the modelled profiles where compared with the ice cores; below this depth subsurface properties were a result of the initialisation process (Section 3.7). C1 was characterised by four large ice lenses between 5-12 m and 2 smaller ones between 2-4 m depth. Density increased with depth; however, it decreased between two ice lenses located at approximately 5.5 and 7.5 m. On the contrary, the corresponding modelled profile only indicates 2 ice lenses at approximately 2.5 and 7.8 m respectively which were related to the summer surface. There were spikes in density that are also related to summer surfaces but these did not form ice lenses in the model. Additionally there is no apparent densification with

depth. C2 has numerous ice lenses throughout, with three notably larger lenses at roughly 9, 13.5 and 16 m depth. M2 also has three distinguishable ice lenses at 3, 11 and 15 m depth, and like M1, does not show any clear densification with depth.

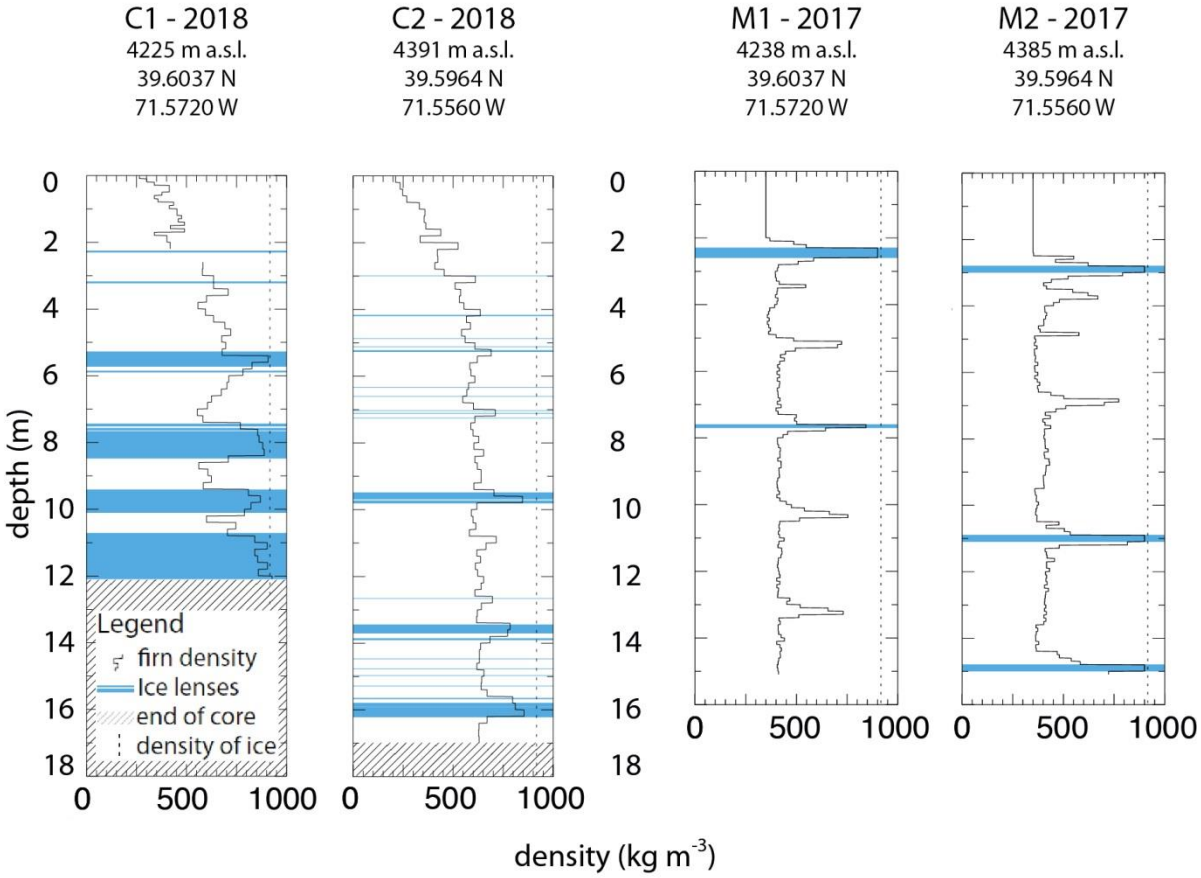


Figure 4.8: Comparison between ice core density profiles at C1 and C2, and the output of the snow model at the same locations labelled M1 and M2.

Chapter 5

Discussion and conclusion

A distributed surface energy balance model was coupled to a snow model and applied to Abramov glacier. Contrary to many remote locations, we are in a unique position as an extraordinary amount of *in-situ* measurements exist from 1967-1999 for this glacier. After a brief interruption, a yearly monitoring programme was re-established in 2011; and included the installation of an automatic weather station (AWS). As such, this master's thesis aimed to explore the suitability of the AWS data for the application of the coupled model. In this section, the results from the coupled model for the years 2013 to 2017 (Chapter 4) are discussed and analysed using literature on Abramov and similar studies where energy balance models were applied.

5.1 Mass balance

Glaciological mass balance calculations for Abramov date back to 1968 due to the extensive monitoring programme. From 1971-1994, several publications reported a predominantly negative mass balance trend; with a mass balance of approximately -0.65±0.12 m w.e. a^{-1} (Dyurgerov 2002; Glazirin et al. 1993; Kamnyansky 2001; Pertziger 1996; WGMS 2005). More recently, Barandun et al. (2015) found a mass balance of -0.51±0.17 m w.e. a^{-1} for 1998-2011, and an overall mass balance of -0.44±0.10 m w.e. a^{-1} for 1968-2014. From 2011-2016, the mass balance was approximately -0.41 m w.e. a^{-1}; however, there was a positive balance (+0.171±0.30 m w.e. a^{-1}) for 2014-2015 (Hoelzle et al. 2017).Overall, the simulated mass balance results were higher than indicated by previous studies and positive overall for 2014-2017 (+0.94 m w.e. a^{-1}). However, the simulated mass balance for 2014-2015 (+0.02 m w.e. a^{-1}) falls within the range reported by Hoelzle et al. (2017) for the same period (+0.171±0.30 m w.e. a^{-1}).

Two major components that affect the mass balance are precipitation and air temperature, with the latter directly influencing the amount of snowfall and the melt rates. The summer months of 2015 (i.e. June, July & August) were characterised by a mean air temperature of 4.2 °C; which was 0.4-0.6 °C warmer than the same period for 2016 and 2017 (Fig. 4.4). Consequently, the fraction of rainfall for the same period in 2015 was 57.4 % and only 38.2 % in 2016; however, it was higher (60.9 %) for 2017. A lack of snowfall between July and August 2015 meant that the albedo diminished from 0.82 in June to 0.46 in August (Fig. 5.1a) and the monthly melt rates increased from 0.28 m w.e. in May to 0.85 m w.e. in July (Fig. 4.3); whereas regular snowfall events kept the glacier-wide albedo above 0.68 during the summer of 2016 (Fig. 5.1b) and melt rates reached a maximum of 0.44 m w.e. for July (Fig. 4.3). Regular glacier-wide snowfall events during the summer considerably reduce the amount of mass loss from ablation process; as was the case for 2016 (Fig. 5.1)

Further analysis of the mass balance results for the ablation area were similar (-7 to -6 m w.e. a^{-1}) for the period 2014-2017 (Fig. 4.1); this would indicate that summer snowfall events were more influential at higher elevations. The coupled model linearly extrapolates the air temperature over the entire glacier using a lapse rate of -5 °C km^{-1} and due to elevation range (3600 to 5000 m a.s.l.) most rainfall events coincide with snowfall events (Fig. 5.1); which most probably occur at higher altitudes where air temperatures are colder. Barandun et al. (2015) applied a lapse rate of -4.8 °C km^{-1} that could have a marginal difference on the accumulation rates at higher elevations.

The simulated precipitation did not correspond with the literature. Kislov (1982) reported that 80 % of annual precipitation occurred as winter accumulation and overall precipitation gradient of 2.44 mm m^{-1} in the past. However, modelled precipitation suggested that 61 % occurred in summer and of that, 69 % was snowfall (Fig. 4.4), and a precipitation gradient of 3.41 mm m^{-1}. Furthermore, simulated precipitation at approximately 3600 and 4200 m a.s.l. was 876 and 2920 mm a^{-1} respectively; whilst historically, Kislov (1982) reported it to be only 246 and 1055 mm a^{-1}. This indicates that precipitation, specifically its spatial and temporal distribution, is associated with a large uncertainty, and could result and account for discrepancies in the coupled model outputs. This is supported by the comparisons with the ablation stakes, as the simulated mass balance was higher in areas where measured mass balance was positive and above 4200 m a.s.l. (Fig. 3.7).

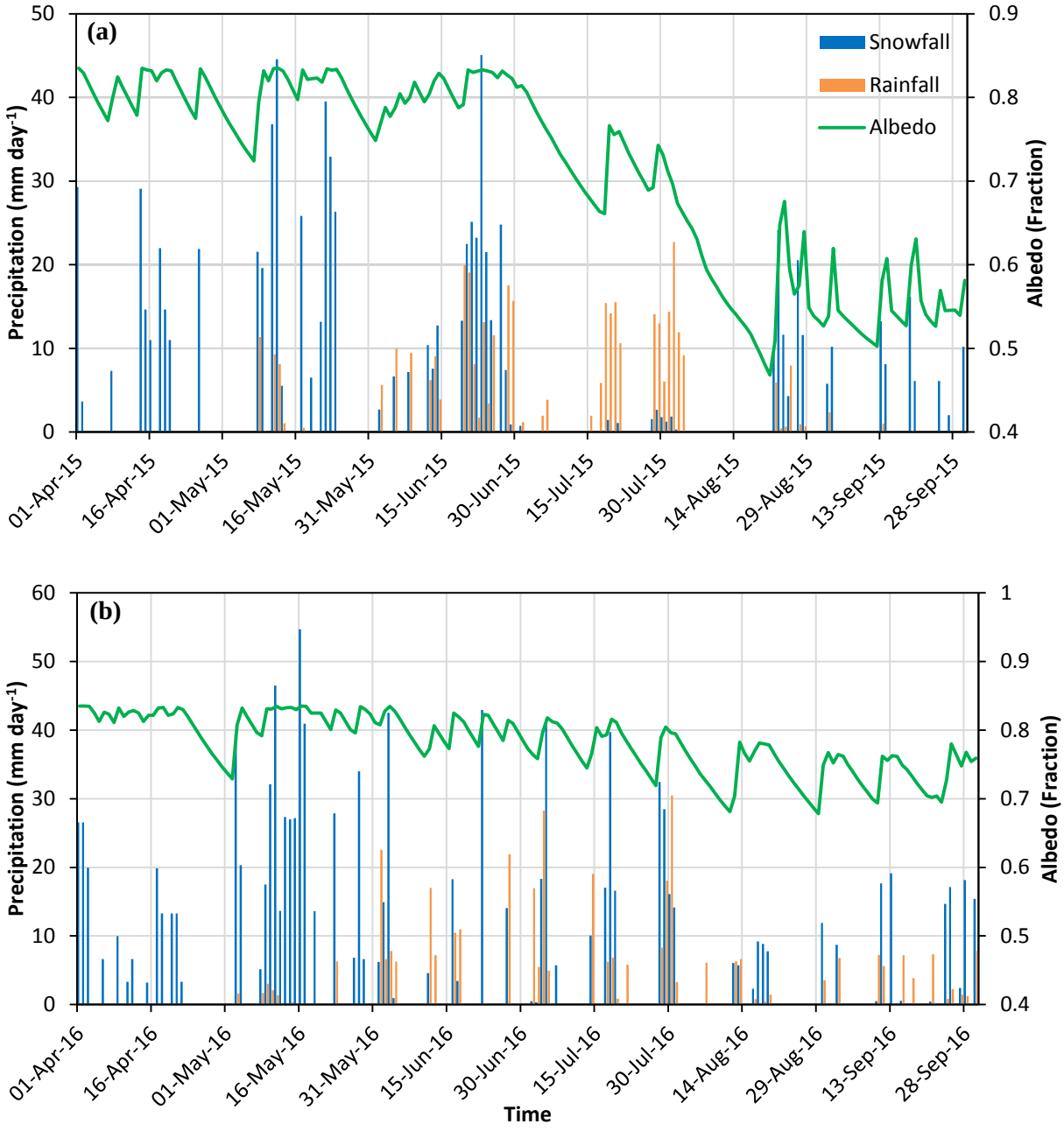


Figure 5.1: Time-series of snowfall, rainfall and albedo for the summer (i.e. April to September) of 2015 (a) and 2016 (b).

Uncertainties with precipitation were due to the lack of *in-situ* or nearby measurements to validate the ERA-Interim reanalysis data. More importantly, the way that the precipitation data was assigned to model timesteps was rudimentary (Section 3.2.4), as monthly precipitation was equally distributed over a specific cloud fraction (> 0.7). The cloud fraction (Fig. 3.3d) defined the temporal distribution of precipitation. It should also be noted that there was no sinusoidal pattern of relative humidity that would normally be associated with the different seasons (Appendix D, Fig. D1). The identification of these uncertainties are important to understanding the unrealistic distribution, duration and intensity of precipitation events; which would have resulted in the overestimation of mass balance. A consequence of the higher precipitation rates was a simulated ELA of 4100 m a.s.l. for 2014-2017 (Fig. 4.1a). This is lower than past data (4260 m a.s.l.) published by Kamnyansky (2001) and the 4207 m a.s.l. calculated by Hoelzle et al. (2017) for 2011-2016.

According to Suslov et al. (1980), the analysis of the firn pits indicated that melt water freezes within the first four annual layers, and ranged from 0.16 to 0.27 m w.e. a^{-1} at the upper firn pit in the 1970s (Fig. 3.2a). Barandun et al. (2015) simulated refreezing to be slightly higher by approximately 0.03 m w.e. a^{-1} at the same locations, and the contribution of annual internal accumulation to be approximately 20 % of the total mass balance in the accumulation area. The coupled model indicates that glacier wide refreezing was 0.83 m w.e. a^{-1}; accounting for 31 % of surface meltwater (2.16 m w.e. a^{-1}) and rainfall (0.48 m w.e. a^{-1}) that infiltrated the snow and firn layers. The coupled model produced higher refreezing rates than the literature; possibly as a result of high accumulation rates which produced deeper snow and firn layers; increasing the retention potential of percolating water as irreducible water.

Although the modelled mass balance did not compare well to *in-situ* measurements and past studies; it provides valuable insight into the different accumulation and ablation processes. Comparisons have allowed for the identification of model parameters (e.g. precipitation) which require further analyses and calibration to produce more realistic mass balance results.

5.2 Energy budget

In order to compare the results from the energy balance model (Section 4.2), analyses were done using literature from Morteratsch glacier (Klok & Oerlemans 2002) and Zhadang glacier (Huintjes et al. 2015) (Table 5.1). In both studies, a distributed energy balance model was applied and their results can be used interpret and validate the coupled model output; however, differences between glaciers and, regional and local climates do influence the surface energy balance. Additionally, both studies present their findings in different formats; as a result the spatial distribution of fluxes was only compared with Morteratsch, while temporal variations were compared with both.

The energy balance results (Section 4.2) were in general accordance with the literature. The spatial distribution of net shortwave radiation (Q_{sw}), net longwave radiation (Q_{lw}), and sensible (Q_{sens}) and latent heat (Q_{lat}) fluxes were compared with similar plots for Morteratsch glacier. The Q_{sw} indicates similar pattern, as it was highest at low elevations and decreased with altitude; but also increased at higher elevations on south facing slopes at both glaciers. The values and range of Q_{sw} was higher at Abramov (10 to 120 Wm^{-2}) compared to Morteratsch (0 to 65 W m^{-2}). Reasons for such a difference can be that Abramov is situated at a higher elevation, thereby reducing the effect of diffusivity and transmissivity of the sky resulting in higher values for incoming shortwave radiation. Additionally, Abramov's lower snow and ice albedo reduces the amount of reflected shortwave radiation, especially

in the ablation area; resulting in a larger difference between incoming and reflected shortwave radiation.

Table 5.1: Summary of characteristics for Abramov, Morteratsch, and Zhadang glacier.

Description	Abramov glacier	Morteratsch glacier	Zhadang glacier
Location	Chong-Alay District, Kyrgyzstan	Pontresina, Switzerland	Baingoin, Nagqu, Tibet, China
Co-ordinates	39°38'55"N 71°35'09"E	46°24' N 08°02' E	30°28.57' N 90°38.71' E
Orientation	North	North	North-west
Elevation range (m a.s.l.)	3600-5000	2000-4000	5553-5947
Surface area (km^2)	24	17.15	~2
Glacier type	Temperate	Temperate	Polythermal
Albedo of snow (Fraction)	0.835	0.9	0.9
Albedo of firn (Fraction)	0.55	0.53	0.55
Albedo of ice (Fraction)	0.25	0.34	0.3
Accumulation season	Winter	Winter	Summer
Ablation season	Summer	Summer	Summer
Study	This study	Klok and Oerlemans (2002)	Huintjes et al. (2015)

At Morteratsch, Q_{lw} displayed a distinct altitudinal pattern that ranges from -30 W m^{-2} at the terminus to -50 W m^{-2} in the accumulation area. Whereas, Q_{lw} ranged from -52 W m^{-2} at the terminus to -70 W m^{-2} on south facing slopes or -46 W m^{-2} on north facing slopes in the accumulation area at Abramov (Fig. 4.5c). In the coupled model Q_{lw} was calculated using air temperature, cloud cover and vapour pressure (calculated from humidity); with the latter two possibly being a source of uncertainty. Nevertheless higher values on north facing slopes at Abramov could result from lower air and surface temperatures due to a lack of incoming shortwave radiation (50 W m^{-2}) when compared to south facing slopes (300 W m^{-2}). The colder surface temperatures (mean: -15 °C) would reduce the amount of emitted longwave radiation and increase Q_{lw} on north facing slopes.

The turbulent heat fluxes ($Q_{sens} + Q_{lat}$) share a similar elevation gradient as Morteratsch, with the highest values near the terminus (28 W m^{-2}), and the lowest at high elevations on south facing slopes (14 W m^{-2}) (Fig. 5.2). However, contrary to Morteratsch and similarly to Q_{lw}, the turbulent fluxes were higher on north facing slopes (34 W m^{-2}) (Fig. 5.2). A possible reason for higher Q_{sens} (Fig. 4.5d) was a higher temperature difference between the air (mean: -9 °C) and surface (mean: -15 °C) temperatures causing glacier winds to develop, the generation of turbulence, and transfer of sensible heat to the glacier surface (Appendix C). Q_{lat} was predominantly negative over the glacier (mean: -3.66 W m^{-2}) indicating the presence of sublimation and evaporation caused by a negative vapour pressure gradient (Fig. 4.5e). On north facing slopes, Q_{lat} ranged between -1 to 0.5 W m^{-2}, meaning that the vapour pressure gradient was closer to zero and even positive; resulting in re-sublimation or condensation at the glacier surface. The calculations of Q_{sens} (Eq. 3.25) and Q_{lat} (Eq. 3.26) required the input of the background turbulent exchange coefficient (C_b), whilst the latter was also influenced by the vapour pressure of the atmosphere and saturated vapour pressure of the surface which were calculated using relative humidity. The C_b was adopted from Van Pelt et al. (2012) were it was calibrated for a glacier in Svalbard and therefore may not be representative of the environment at Abramov. Again, there is some uncertainty with the measured relative humidity and its extrapolation.

A comparison of the temporal variations of the energy fluxes can be made with Morteratsch and Zhadang glacier. For Morteratsch, Q_{sw} was highest from April to October; whereas, Q_{sw} was highest from September to February for Zhadang. At Abramov, Q_{sw} was more comparable to Morteratsch as they both experience a summer ablation season. Glacier-wide incoming shortwave radiation (S_{in}) reaches a maximum of 350 W m^{-2} during August and September at Abramov (Fig. 5.3); and a maximum of approximately 330 W m^{-2} for June and July at Morteratsch's terminus. The amount of reflected solar radiation (S_{out}) is dependent on the albedo and instead of observing a decrease in S_{out} as the albedo declines over the summer months as was the case for Morteratsch, regular snowfall events prevents the albedo from declining and ensures a higher S_{out} (Fig. 5.1 & 5.3).

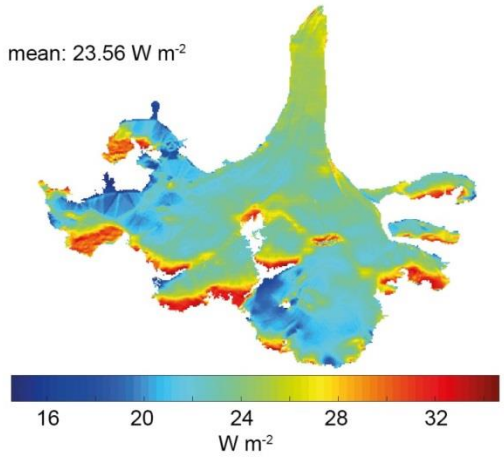


Figure 5.2: Spatial distribution of the sensible plus latent heat flux averaged over the period 2013-2017.

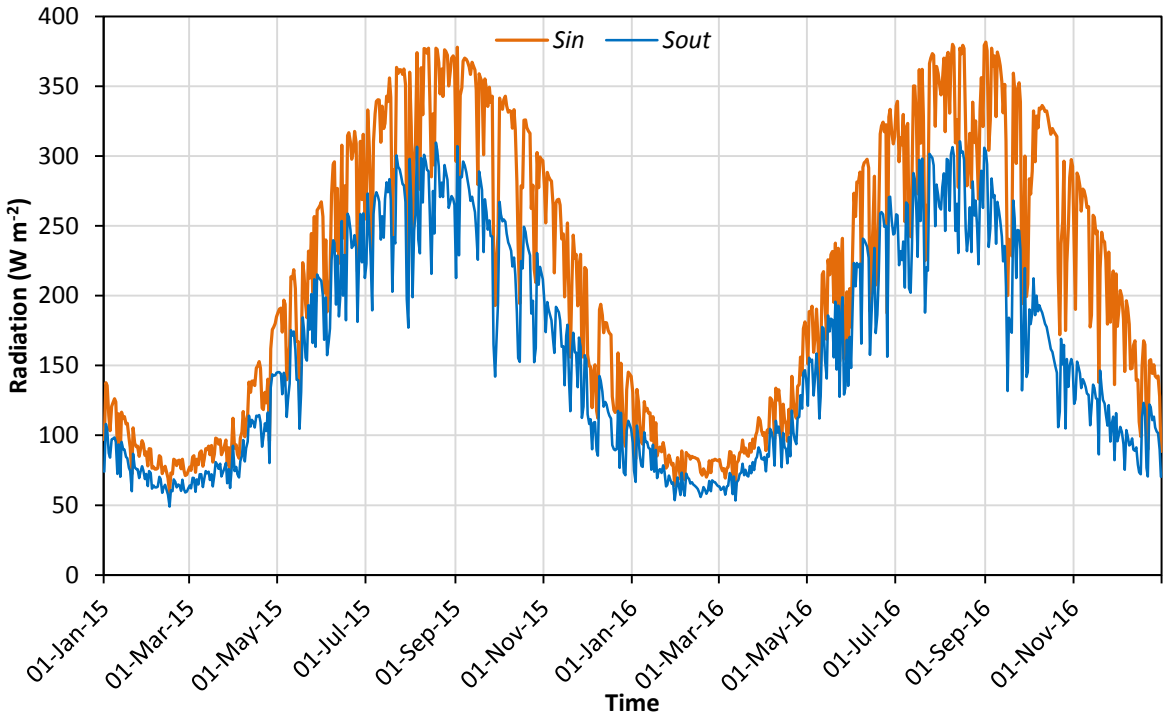


Figure 5.3: Time series glacier-wide simulated daily mean fluxes of incoming and reflected shortwave radiation for 2015 and 2016.

The standard deviation of simulated Q_{lw} was 6.3 W m^{-2} for 2013-2017 at Abramov (Fig. 4.6). This was smaller than the deviation of 33 W m^{-2} between the summer and winter months at Zhadang. The large deviation at Zhadang can be attributed to the polythermal properties of the glacier (i.e. lower levels of emitted longwave radiation (L_{out})), and a higher level of humidity and cloud cover over the summer months; while winter months were predominantly cloud free. This would suggest that the difference between cloud cover in summer and winter was relatively small at Abramov. The relatively consistent cloud fraction combined with the temperate glacier means that for most of the year the Q_{lw} remains stable on Abramov.

The Q_{sens} was 28 and 21 W m^{-2} for summer and winter months at Zhadang; which was similar to the values of 28 and 25 W m^{-2} modelled for Abramov (Fig. 4.6). This would suggest that the temperature difference between the atmosphere and glacier surface is similar. While Q_{lat} was -20 and -49 W m^{-2} compared to the -5 and -1 W m^{-2} for summer and winter at Abramov (Fig. 4.6). Zhadang experienced higher levels of sublimation in winter, possibly related to a negative vapour pressure gradient that was much higher than Abramov's due to environmental differences. Additionally, the summer value was lower than the winter value for Q_{lat} at Abramov; whereas the opposite occurred at Zhadang. The difference between summer (mean: 0.57) and winter (mean: 0.56) relative humidity would have resulted in a smaller difference between the seasons for Q_{lat}, as well as, smaller values due to the relatively moist atmosphere.

5.3 Subsurface

In its current configuration, the coupled model does not adequately represent the subsurface process at Abramov glacier. A comparison between modelled and measured density profiles indicated that there were a lack of ice layers and more importantly, negligible densification with depth in the modelled profiles (Fig. 4.8).

The formation and frequency of ice layers by refreezing was dependent on the input of meltwater from the surface and rain, and the subsurface temperature and density. It would seem that once the cold content had dissipated, infiltrating water passed quickly through the less dense snow and firn packs (Fig. 4.7). As a consequence, refreezing of percolating water was minimal and was not in accordance with Suslov et al. (1980) who reported that melt water refreezes within the first four annual layers. Higher densities at depth would reduce the rate of infiltration and favour refreezing.

An important process in glacier formation is the transformation of snow to ice (i.e. densification) described by Herron and Langway (1980). However, the modelled subsurface density profiles indicated no such densification which can be seen in the ice cores (Fig. 4.8). The reason for this lies with how Ligtenberg et al. (2011) modified the gravitational densification rate ($G(\rho, T)$) (Eq. 3.34) to include the dependence of C on the accumulation rate (b) (Eq. 3.35). High accumulation rates at M1 (2044 mm w.e. a^{-1}) and M2 (3212 mm w.e. a^{-1}) equate to extremely small values for $C(b)$ which reduces the $G(\rho, T)$. A comparison of the equations used to calculate $C(b)$ in this study with Van Pelt et al. (2012) and Ligtenberg et al. (2011) can be done using b for density profiles M1 and M2 (Table 5.2). Using the parameterization from Van Pelt et al. (2012), the results for $C(b)$ at M1 and M2 were negligible. The results for $C(b)$ were higher using the setup from Ligtenberg et al. (2011) where $\rho < 550\, kg\, m^{-3}$; however, they were also small or negative where $\rho \geq 550\, kg\, m^{-3}$. The configuration used in this study was similar to Ligtenberg et al. (2011) but correction factors of 0.07 and 0.03 were applied for the separate density calculations. The effect of the correction factors drastically reduces the value for $C(b)$. The relationship between high accumulation rates and low or

negative values for $C(b)$ were noted by Ligtenberg et al. (2011) for sites in the Antarctic Peninsula, and therefore they imposed a minimum value of 0.25 for $C(b)$ where accumulation rates exceeded a mean annual accumulation of 1400 mm a^{-1}. If this were to be applied to Abramov, any accumulation and densification above approximately 3950 m a.s.l. would have a value of 0.25 for $C(b)$; which in reality would probably not be characteristic of the glacier subsurface. Thus calibration of $C(b)$ would be required to improve the modelled subsurface results and can be done by comparing modelled and observed depths of where ρ equals 550 and 830 kg m^{-3} (Ligtenberg et al. 2011). It should be noted, however, that precipitation would need to be calibrated first to ensure realistic accumulation rates.

Table 5.2: Comparison of equations used by Van Pelt et al.(2012), Ligtenberg et al. (2011) and this study to calculate the variable $C(b)$ used in the equation for gravitational densification rate $G(\rho, T)$ for density profiles M1 and M2. Mean annual accumulation rates (b) at M1 and M2 were 2044 and 3212 mm w.e. a^{-1} respectively.

Study	Equation configuration for $C(b)$	M1	M2
Van Pelt et al.(2012)	$0.0991 - 0.0103\ log(b), \rho\ < 550\ kg\ m^{-3}$ $0.0701 - 0.0086\ log(b)\ , \rho\ \geq 550\ kg\ m^{-3}$	0.021 0.005	0.014 0.001
Ligtenberg et al. (2011)	$1.453 - 0.151\ log(b), \rho\ < 550\ kg\ m^{-3}$ $2.336 - 0.293\ log(b)\ , \rho\ \geq 550\ kg\ m^{-3}$	0.302 0.103	0.234 -0.029
This study	$0.07 \times (1.4151 - 0.147)\ log(b)), \rho\ < 550\ kg\ m^{-3}$ $0.03 \times (2.335 - 0.288)\ log(b))\ , \rho\ \geq 550\ kg\ m^{-3}$	0.021 0.004	0.016 0.0002
Adjustment for high accumulation rates (Ligtenberg et al. 2011)	$1.453 - 0.151\ log(b),\ 0.25, \rho\ < 550\ kg\ m^{-3}$ $2.336 - 0.293\ log(b),\ 0.25\ , \rho\ \geq 550\ kg\ m^{-3}$	0.25 0.25	0.25 0.25

5.4 Limitations and recommendations

The main limitations to this study involved the meteorological input variables, calibration and initialisation of the coupled model. These themes require further analyses in order to produce a more realistic model output.

A closer look at the meteorological input variables indicates further processing and information was required. There was a lack of temporal variation for the measured relative humidity which is expected to have some form of seasonal difference as was the case in Huintjes et al. (2015) and past measurements at Abramov (Appendix D, Fig. D1). Cloud cover was simulated from measured relative humidity and incoming shortwave radiation; with the later having a stronger influence on the result. Nevertheless, simulated cloud cover and measured relative humidity had a positive correlation of 0.75. As relative humidity and cloud cover were used in the coupled model; specifically for the calculation of incoming shortwave and longwave radiation, and the sensible heat flux; uncertainty was added to these parameters. A possible solution would be to compare the measured relative humidity at the AWS with the relative humidity derived from ERA-Interim reanalysis data or use the reanalysis data in the coupled model. The latter should produce a temporal variation where relative humidity and

precipitation are similar because reanalysis precipitation is based on temperature as well as humidity data. Additionally, a closer analysis of measured incoming shortwave radiation should be done, as this variable had the largest influence in the calculation of cloud cover (Section 3.2.3).

The current setup of determining precipitation events at 3-hourly timesteps from monthly precipitation sums was deemed inadequate (Section 3.2.4). The process does not take into account precipitation duration or intensity; instead, an equal amount of precipitation was assigned to cloud fractions of 0.7 or greater for each month depending on the monthly sum. Additionally, the uncertainty attached to cloud cover can affect the temporal distribution during a month. A solution would be to extract precipitation at a higher temporal resolution from ERA-Interim reanalysis data to match the 3-hourly model timesteps. It should be noted that there exists a level of uncertainty for reanalysis data.

Further calibration of the parameters in Table 3.3 is required to better represent the environment at Abramov. Currently, several parameters taken from Van Pelt et al. (2012) are more applicable for a glacier in Svalbard and can be further calibrated. By comparing modelled and observed incoming shortwave radiation under clear-sky conditions the aerosol transmissivity constant (k) can be tuned (Van Pelt et al. 2012). Furthermore, the relationship between the cloud factor (T_{cl}) and cloud cover (n) can be determined using cloud observation as described by Greuell et al. (1997). The observations can then be linked to the ratio of measured and computed clear-sky radiation in order to better constrain the equation for the transmission coefficient for cloud cover (Eq. 3.18). Incoming longwave radiation can be better calibrated by changing the constants cloud emissivity constant (ε_{cl}) and the constant b used in the equations 3.22 and 3.23. Both ε_{cl} and b are calibrated using the process described in Section 3.6 which requires incoming longwave radiation measurements. The Abramov AWS measures incoming long wave radiation and although it contains numerous data gaps and errors, it should be possible to compile enough data to calibrate ε_{cl} and b. Precipitation additionally requires further calibration as the current correction factor and altitudinal gradient result in higher glacier-wide precipitation rates and a steep altitudinal gradient of 3.44 mm m^{-1}. Kislov (1982) noted a difference of +2.14 mm m^{-1} between summer and winter precipitation gradients and due to these large difference it may be sensible to include a summer and winter precipitation altitudinal gradient in the model calculations.

Simulated and observed density profiles did not agree; one of the main reasons for this was the modelled profiles lacked densification with depth. This was caused by high accumulation rates used to calculate $C(b)$ in the calculation of gravitational densification (Section 5.2). Refinement of this could be done using ice cores. This, however, would require drilling down to a depth where density reaches 830 kg m^{-3}; which could prove difficult for Abramov.

Lastly, it is important to consider the time period selected for the coupled model. The analysis steps followed for selecting suitable meteorological data, as described in Section 3.2.1, resulted in a reduced dataset only covering the period November 2013 to September 2017. The restricted timeframe of the meteorological input, reduced from the raw dataset spanning August 2011 to December 2017, could be insufficient for model initialisation (Section 3.7); however, at presence it's significance is not clear. It is possible that the initialisation is more influenced by the unusually high accumulation rates.

5.5 Conclusion

The aims of this study were to determine if sufficient data could be compiled to run an existing coupled distributed energy balance and snow model for Abramov glacier. And then, to compare the model output for glacier-wide mass balance, energy budget, and subsurface density profiles with literature and *in-situ* measurements. The current application of the coupled model was the first of its kind for Abramov as was applied for the period November 2013 to September 2014.

Compilation of climate variables (i.e. air temperature, pressure, humidity, cloudiness, and precipitation) proved challenging (Section 3.2). Air temperature, pressure and relative humidity measurements from the AWS contained numerous data gaps and errors; with the result being a continuous dataset with a relatively short temporal extent. The cloud cover fraction had to be calculated using the AWS parameters as well as the measured incoming shortwave radiation. While the monthly precipitation data was acquired from ERA-Interim reanalysis and assigned to time intervals of a specific cloud fraction.

Overall, the distributed energy balance model was able to account for spatial variability of the fluxes; furthermore, the results were within physically possible means, and comparable with similar studies (Klok & Oerlemans 2002; Huintjes et al. 2015). However, there were some discrepancies when comparing the temporal distribution and altitudinal differences.

On the other hand, the subsurface snow model did not perform well when comparing modelled and measured density profiles. This was caused by the high accumulation rates for which the densification equation calculated negligible densification with depth. Further tuning of this equation is required to improve the results of the subsurface.

The final results from the coupled model run revealed the mass balance to be positive for the entire period (+0.94 m w.e. a^{-1}) which is contradictory to the negative trends estimated in past studies (Barandun et al. 2015; Dyurgerov 2002; Glazirin et al. 1993; Hoelzle et al. 2017; Kamnyansky 2001; Pertziger 1996; WGMS 2005). Even taking into account the uncertainty of these past estimates, it cannot be overlooked that they all report a negative trend. The model simulated the predominant precipitation type to be snowfall (85 %); this ensured a higher glacier-wide albedo (0.78) and reduced melt rates during the summer months which contributed to the overall positive mass balance. The temporal distribution of precipitation combined with cloud cover and relative humidity were identified as possible reason for the positive mass balance trend.

Overall, this master's thesis provided a foundation for the application of a coupled model for Abramov glacier. Moreover, it identified numerous input and model parameters where further analyses and calibration was required. Initial results indicate the potential for applying such a complex model in order to better understand the surface and subsurface processes at Abramov and how they evolve in the global warming trend.

References

Arthern, R.J. et al., 2010. In situ measurements of Antarctic snow compaction compared with predictions of models. *Journal of Geophysical Research*, 115(3), pp.1–12.

Atwater, M.A. & Ball, J.T., 1981. A surface solar radiation model for cloudy atmospheres. *Monthly weather review*, 109, pp.878–888.

Atwater, M.A. & Brown, P.S., 1974. Numerical computations of the latitudinal variation of solar radiation for an atmosphere of varying opacity. *Journal of Applied Meteorology*, 13, pp.289–297.

Barandun, M. et al., 2015. Re-analysis of seasonal mass balance at Abramov glacier 1968-2014. *Journal of Glaciology*, 61(230), pp.1103–1117.

Benn, D.I. et al., 2005. Reconstruction of equilibrium-line altitudes for tropical and sub-tropical glaciers. *Quaternary International*, 138–139, pp.8–21.

Bernauer, T. & Siegfried, T., 2012. Climate change and international water conflict in Central Asia. *Journal of Peace Research*, 49(1), pp.227–239.

Berrisford, P. et al., 2011. Atmospheric conservation properties in ERA-Interim. *Quarterly Journal of the Royal Meteorological Society*, 137(659), pp.1381–1399.

Bougamont, M., Bamber, J.L. & Greuell, W., 2005. A surface mass balance model for the Greenland Ice Sheet. *Journal of Geophysical Research*, 110(4), pp.1–13.

Christianson, K. et al., 2015. Dynamic perennial firn aquifer on an Arctic glacier. *Geophysical Research Letters*, 42(5), pp.1418–1426.

Cogley, J.G. et al., 2011. *Glossary of glacier mass balance and related terms*, Paris.

Cuffey, K.M. & Paterson, W.S.B., 2010. *The physics of glaciers* 4th Editio., Elsevier Science & Technology. Available at: http://linkinghub.elsevier.com/retrieve/pii/0016718571900868.

Davies, J.A. & McKay, D.C., 1989. Evaluation of selected models for estimating solar radiation on horizontal surfaces. *Solar Energy*, 43(3), pp.153–168.

Dee, D.P. et al., 2011. The ERA-Interim reanalysis: configuration and performance of the data assimilation system. *Quarterly Journal of the Royal Meteorological Society*, 137(656), pp.553–597.

Denzinger, F., 2018. *Structure from Motion using historical aerial images to analyse changes in surface elevation and volume on Abramov Glacier, Kyrgyzstan*. University of Zurich, Switzerland.

Dozier, J. & Frew, J., 1990. Rapid calculation of terrain parameters for radiation modeling from digital elevation data. *IEEE Transactions on Geoscience and Remote Sensing*, 28(5), pp.963–969.

Dyurgerov, M., 2002. Glacier mass balance and regime: data of measurements and analysis (Occasional Paper 55).

Eischeid, J.K. et al., 1995. The quality control of long-term climatological data using objective data analysis. *Journal of Applied Meteorology*, 34, pp.2787–2795.

Farinotti, D. et al., 2015. Substantial glacier mass loss in the Tien Shan over the past 50 years. *Nature Geoscience*, 8, pp.716–722.

Glazirin, G., Kamnyansky, G. & Pertziger, F., 1993. *Regime of Abramov Glacier*, Leningrad, Russia: Hydrometeo Publishing.

Greuell, W., Knap, W.H. & Smeets, P.C., 1997. Elevational changes in meteorological variables along a midlatitude glacier during summer. *Journal of Geophysical Research: Atmospheres*, 102(D22), pp.25941–25954. Available at: http://doi.wiley.com/10.1029/97JD02083.

Greuell, W. & Konzelmann, T., 1994. Numerical modelling of the energy balance and the englacial temperature of the Greenland Ice Sheet. Calculations for the ETH-Camp location (West Greenland, 1155 m a.s.l.). *Global and Planetary Change*, 9, pp.91–114.

Herron, M.M. & Langway, C.C., 1980. Firn densification: an empirical model. *Journal of Glaciology*, 25(93), pp.373–385.

Hoelzle, M. et al., 2017. Re-establishing glacier monitoring in Kyrgyzstan and Uzbekistan, Central Asia. *Geoscientific Instrumentation, Methods and Data Systems*, 6(2), pp.397–418.

Hooke, R.L., 2005. *Principles of glacier mechanics* Second Edi., Cambridge, UK: Cambridge University Press.

Houghton, H.G., 1954. On the annual heat balance of the Northern Hemisphere. *Journal of Meteorology*, 11, pp.1–9.

Huintjes, E. et al., 2015. Evaluation of a coupled snow and energy balance model for Zhadang glacier, Tibetan Plateau, using glaciological measurements and time-lapse photography. *Arctic, Antarctic, and Alpine Research*, 47(3), pp.573–590. Available at: http://www.bioone.org/doi/10.1657/AAAR0014-073.

IPCC, 2013. *Climate change 2013: The physical science basis. Contribution of Working Group I to the Fifth Assessment Report of the Intergovernmental Panel on Climate Change* T. F. Stocker et al., eds., United Kingdom and New York, NY, USA, 1535 pp: Cambridge University Press.

Iqbal, M., 1983. *Introduction to Solar Radiation*, Academic Press.

Kamnyansky, G., 2001. Abramov Glacier mass-balance observations resume (1967–1998). *Proc. SANIGMI*, 161(242), pp.122–131.

Kislov, B. V., 1982. *Formirovanie i reshin firnovo-ledjanoy tolshi gornogo lednika*.

Klok, E.J. & Oerlemans, J., 2002. Model study of the spatial distribution of the energy and mass balance of Morteratschgletscher, Switzerland. *Journal of Glaciology*, 48(163), pp.505–518.

Konzelmann, T. et al., 1994. Parameterization of global and longwave incoming radiation for the Greenland Ice Sheet. *Global and Planetary Change*, 9(1–2), pp.143–164.

Ligtenberg, S.R.M., Helsen, M.M. & Van Den Broeke, M.R., 2011. An improved semi-empirical model for the densification of Antarctic firn. *Cryosphere*, 5(4), pp.809–819.

Machguth, H. et al., 2008. The Cryosphere Exploring uncertainty in glacier mass balance modelling with Monte Carlo simulation. *The Cryosphere*, 2, pp.191–204.

McDonald, J.E., 1960. Direct absorption of solar radiation by atmospheric water vapor. *Journal of Meteorology*, 17, pp.319–328.

Meyers, T.P. & Dale, R.F., 1983. Predicting Daily Insolation with Hourly Cloud Height and Coverage. *Journal of Climate and Applied Meteorology*, 22(4), pp.537–545. Available at: http://journals.ametsoc.org/doi/abs/10.1175/1520-0450(1983)022%3C0537:PDIWHC%3E2.0.CO;2.

Oerlemans, J., 1992. Climate sensitivity of glaciers in southern Norway: application of an energy-balance model to Nigardsbreen, Hellstugubreen and Alfotbreen. *Journal of Glaciology*, 38(129), pp.223–232.

Oerlemans, J. & Grisogono, B., 2002. Glacier winds and parameterisation of the related surface heat fluxes. *Tellus*, 54A(5), pp.440–452.

Oerlemans, J. & Knap, W.H., 1998. A 1 year record of global radiation and albedo in the ablation zone of Morteratschgletscher , Switzerland. *Journal of Glaciology*, 44(147), pp.231–238.

Van Pelt, W.J.J. et al., 2013. An iterative inverse method to estimate basal topography and initialize ice flow models. *The Cryosphere*, 7(3), pp.987–1006.

Van Pelt, W.J.J. et al., 2014. Inverse estimation of snow accumulation variability along a snow radar transect on Nordenskioldbreen, Svalbard. *Journal of Geophysical Research: Earth Surface*, 119, pp.816–835.

Van Pelt, W.J.J. et al., 2012. Simulating melt, runoff and refreezing on Nordenskiöldbreen, Svalbard, using a coupled snow and energy balance model. *The Cryosphere*, 6, pp.641–659.

Van Pelt, W.J.J. & Kohler, J., 2015. Modelling the long-term mass balance and firn evolution of glaciers around Kongsfjorden, Svalbard. *Journal of Glaciology*, 61(228), pp.731–744.

Van Pelt, W.J.J., Pohjola, V.A. & Reijmer, C.H., 2016. The changing impact of snow conditions and refreezing on the mass balance of an idealized Svalbard glacier. *Frontiers in Earth Science*, 4(102), p.Article 102.

Pertziger, F., 1996. *Abramov Glacier Data Reference Book: Climate, Runoff, Mass Balance*, Munich: Munich Technical University.

Pfeffer, W.T. & Humphrey, N.F., 1996. Deterntination of timing and location of water movement and ice-layer formatation by temperature measurements in sub-freezing snow. *Journal of Glaciology*, 42(141), pp.292–304.

Reijmer, C.H. & Hock, R., 2008. Internal accumulation on Storglaciaren, Sweden, in a multi-layer snow model coupled to a distributed energy- and mass-balance model. *Journal of Glaciology*, 54(184), pp.61–72.

Schneider, T. & Jansson, P., 2004. Internal accumulation in firn and its significance for the mass balance of Storglaciären, Sweden. *Journal of Glaciology*, 50(168), pp.25–34.

Schöne, T. et al., 2013. A new permanent multi-parameter monitoring network in Central Asian high mountains - from measurements to data bases. *Geoscientific Instrumentation, Methods and Data Systems*, 2(1), pp.97–111. Available at: http://www.geosci-instrum-method-data-syst.net/2/97/2013/.

Siegfried, T. et al., 2012. Will climate change exacerbate water stress in Central Asia? *Climatic Change*, 112, pp.881–899.

Smith, W.L., 1966. Note on the Relationship Between Total Precipitable Water and Surface Dew Point. *Journal of Applied Meteorology*, 5(5), pp.726–727. Available at: http://journals.ametsoc.org/doi/abs/10.1175/1520-0450%281966%29005%3C0726%3ANOTRBT%3E2.0.CO%3B2.

Sorg, A. et al., 2012. Climate change imapcts on glaciers and runoff in Central Asia. *Nature Climate Change*, 2, pp.725–731.

Sturm, M. et al., 1997. The thermal conductivity of seasonal snow. *Journal of Glaciology*, 43(143), pp.26–41.

Suslov, B., Akbarov, A. & Yemelyanov, J., 1980. Abramov glacier.

Vega, C.P. et al., 2016. A synthetic ice core approach to estimate ion relocation in an ice field site experiencing periodical melt: A case study on Lomonosovfonna, Svalbard. *The Cryosphere*, 10(3), pp.961–976.

WGMS, 2005. *Fluctuations of glaciers 1995-2000 (Vol. VIII)*, Zurich, Switzerland.

WGMS, 1996. *Glacier Mass Balance Bulletin No. 4*, Zurich.

Wilks, D.S., 2011. *Statistical methods in the atmospheric sciences* 3rd Editio., Academic Press.

Yen, Y., 1981. *Review of thermal properties of snow, ice and sea ice*, Available at: http://www.dtic.mil/dtic/tr/fulltext/u2/a103734.pdf.

Appendix A

Meteorological data processing

Table A1: Summary of original dataset, identification and removal of outliers, final dataset, and interpolated intervals for the meteorological data.

Detail	Air temperature	Barometric air pressure	Relative humidity	Shortwave radiation (Incoming)
Original timeframe	28/08/2011-01/12/2017	28/08/2011-01/12/2017	28/08/2011-01/12/2017	28/08/2011-01/12/2017
Measured units	Celsius (°C)	Hectopascals (hPa)	%	Watts per square metre (W m^{-2})
Converted units	Kelvin (K)	Pascal (Pa)	-	-
Interval (minutes)	5	5	5	5
Number of measurements	445943	446141	445941	445863
Number of missing measurements	212725	212527	212727	212805
Total number of outliers identified and removed	1100	4719	9	-
Outliers identified using IQR	37	197	9	-
Outliers identified using moving mean	413	782	-	-
Outliers identified manually	650	3740	-	-
Manually removed data (Dates)	21-24 Jun 2014	23-26 May 2013 15-17 Sep 2013 20-24 Jun 2014 24-26 Sep 2014 11-14 May 2016 03-06 Jun 2016 24-25 Jun 2016 24-26 Jun 2017	-	-
Upper threshold	-	-	100	-
Lower threshold	-	-	0	0
Final dataset timeframe	01/11/2013-30/09/2017	01/11/2013-30/09/2017	01/11/2013-30/09/2017	01/11/2013-30/09/2017
Interval (hours)	3	3	3	3
Number of intervals	11433	11433	11433	11433
Total number of interpolated intervals	60	156	42	44

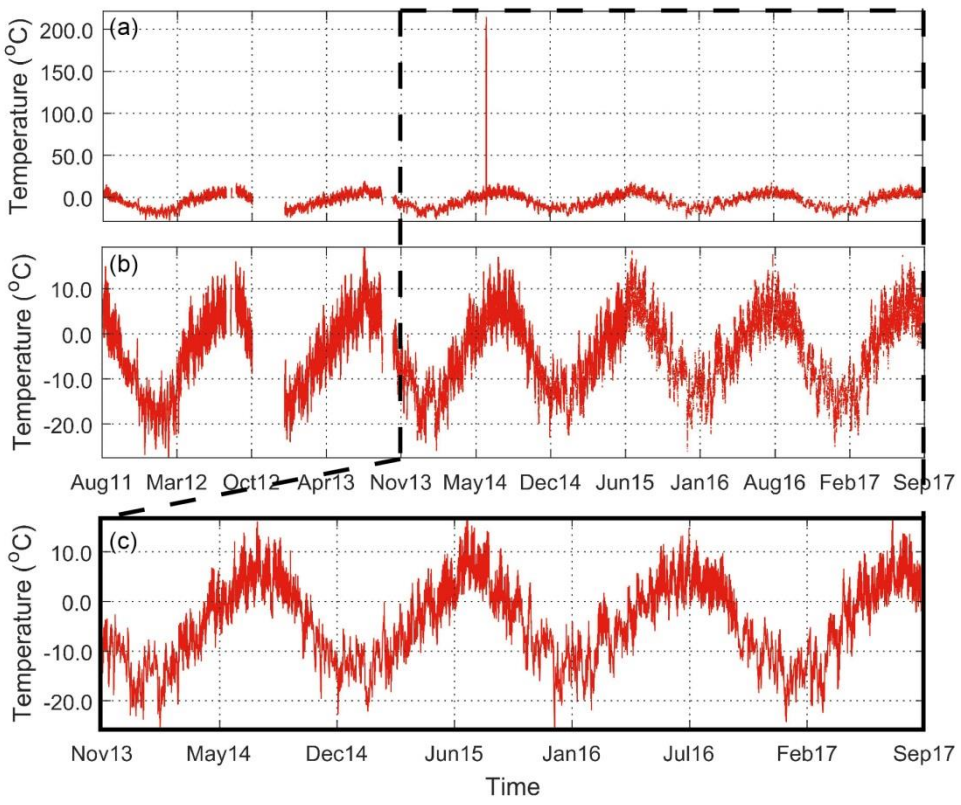


Figure A1: Time series of the original dataset (a), filtered dataset (b), and final dataset (c) for temperature.

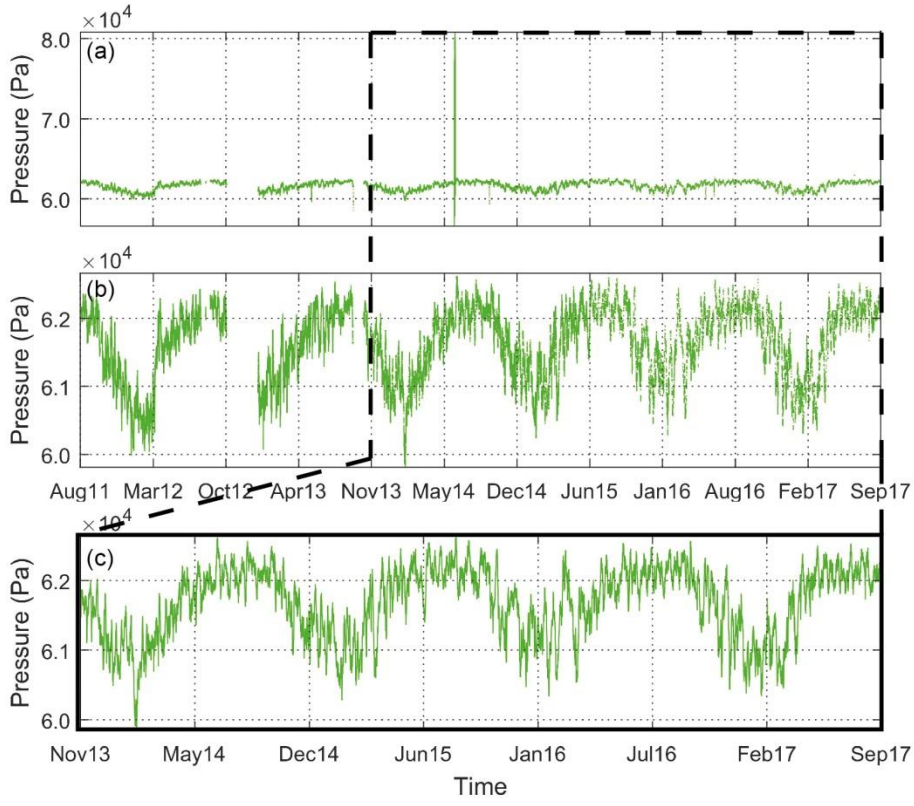


Figure A2: Time series of the original dataset (a), filtered dataset (b), and final dataset (c) for barometric air pressure.

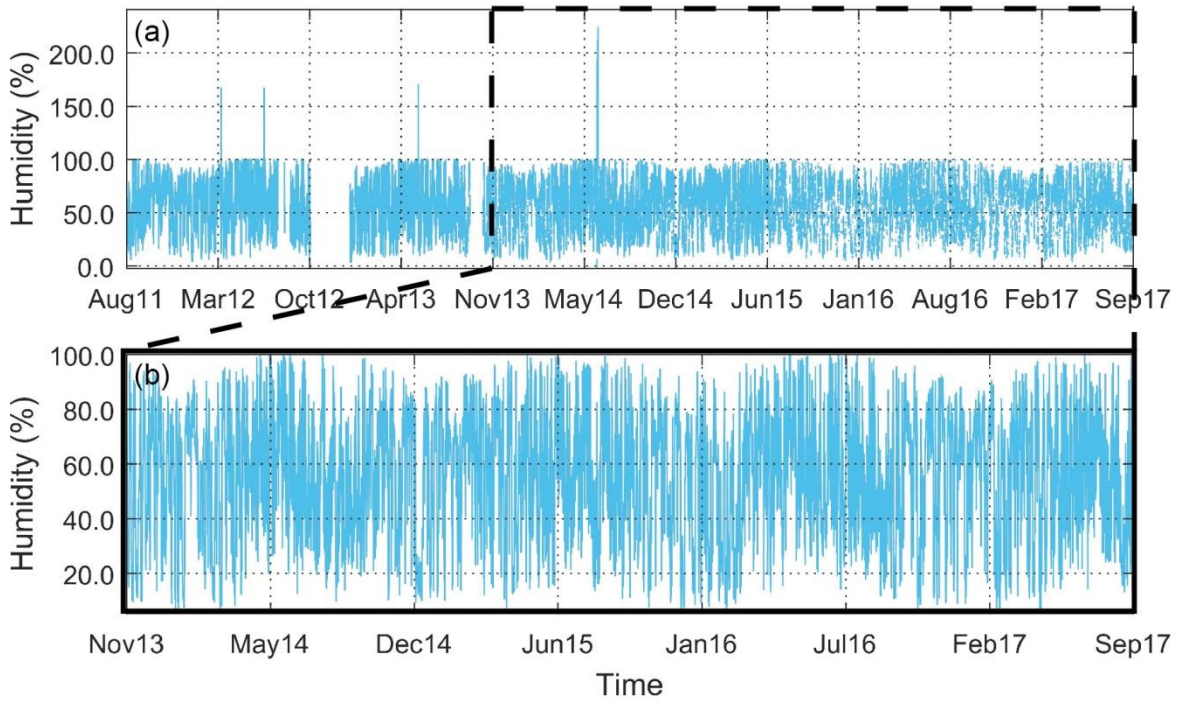


Figure A3: Time series of the original dataset (a), and final dataset (b) for relative humidity. Note: No filtering was utilised, however, and upper and lower threshold was applied.

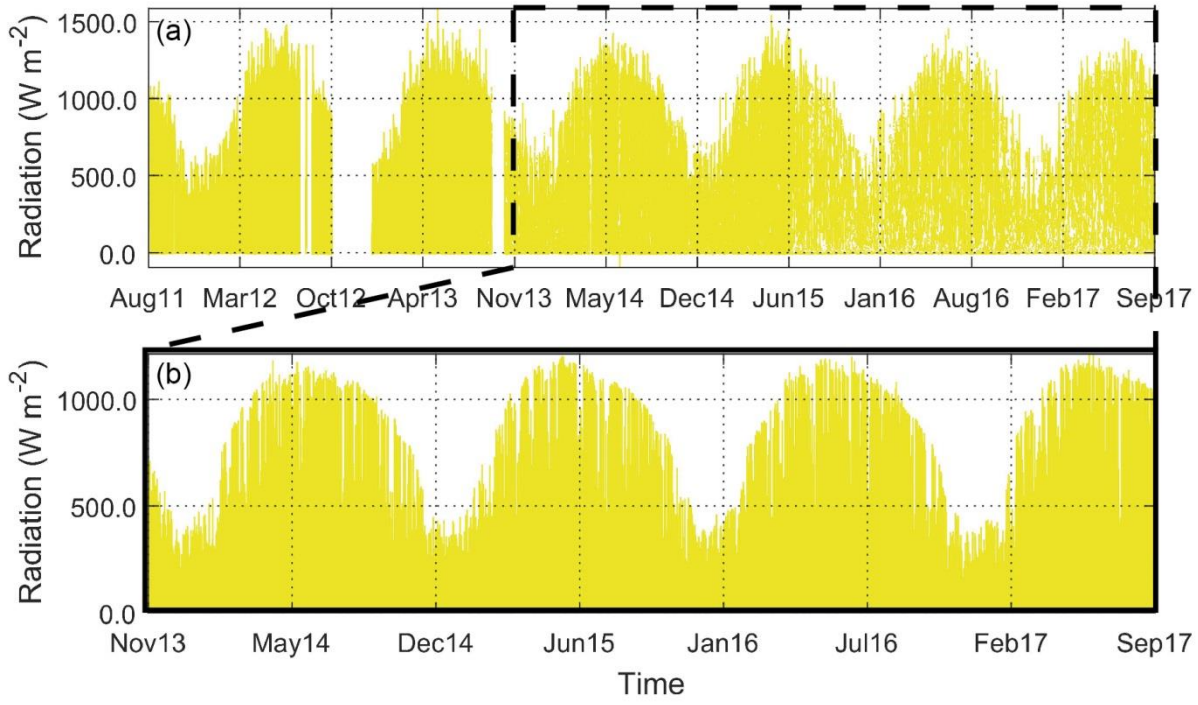


Figure A4: Time series of the original dataset (a), and final dataset (b) for incoming shortwave radiation used for simulating the cloud fraction. Note: No filtering was utilised, however, a lower threshold was applied.

Appendix B

Calibration results

Table B1: Parameter settings and statistical results for the calibration process. Results were calculated from the modelled and observed mass balance at stake sites.

Run no.	Initial parameters				Results			
	Precipitation gradient	Precipitation correction	Albedo of ice	Lapse rate ($x10^{-3}$)	BIAS	AME	RMSE	R^2
1	0.002	1.00	0.40	-0.006	1.94	1.97	2.14	0.89
2	0.002	1.05	0.40	-0.006	1.79	1.82	1.99	0.89
3	0.002	1.20	0.40	-0.006	1.41	1.44	1.60	0.88
4	0.002	1.20	0.40	-0.006	1.12	1.17	1.34	0.90
5	0.002	1.20	0.25	-0.006	2.16	2.21	2.53	0.90
6	0.002	2.50	0.25	-0.006	-0.54	0.74	0.86	0.90
7	0.002	2.35	0.25	-0.006	-0.40	0.66	0.77	0.91
8	0.002	2.35	0.25	-0.006	-0.39	0.66	0.75	0.71
9	0.002	2.20	0.25	-0.006	-0.18	0.61	0.71	0.77
10	0.0015	2.20	0.25	-0.006	-0.31	0.62	0.71	0.70
11	0.0015	2.10	0.25	-0.006	-0.17	0.57	0.67	0.76
12	0.0015	1.95	0.25	-0.006	0.10	0.54	0.66	0.81
13	0.0015	1.85	0.25	-0.006	0.25	0.57	0.72	0.83
14	0.0015	1.75	0.25	-0.006	0.43	0.67	0.86	0.82
15	0.001	1.75	0.25	-0.006	0.25	0.54	0.70	0.82
16	0.001	1.45	0.25	-0.006	0.91	0.98	1.22	0.85
17	0.001	1.45	0.25	-0.006	0.94	0.97	1.11	0.86
18	0.001	1.30	0.25	-0.006	1.17	1.19	1.32	0.86
19	0.001	1.80	0.25	-0.006	0.68	0.74	0.88	0.87
20	0.001	1.95	0.25	-0.006	0.21	0.46	0.57	0.84
21	0.001	1.95	0.25	-0.006	-0.02	0.54	0.65	0.89
22	0.001	1.95	0.25	-0.006	-0.18	0.47	0.58	0.79
23	0.001	1.95	0.25	-0.005	-0.46	0.71	0.88	0.67
24	0.001	1.60	0.25	-0.005	-0.01	0.47	0.58	0.82
25	0.001	1.50	0.25	-0.005	0.13	0.49	0.58	0.83
26	0.0015	1.50	0.25	-0.005	0.22	0.46	0.55	0.86
27	0.0015	1.50	0.25	-0.005	0.99	1.01	1.15	0.86
28	0.0016	1.50	0.25	-0.005	1.04	1.07	1.19	0.86
29	0.0016	1.55	0.25	-0.005	0.96	0.99	1.12	0.86
30	0.0016	1.80	0.25	-0.005	0.61	0.68	0.83	0.92
31	0.0016	1.80	0.25	-0.005	0.64	0.70	0.86	0.84
32	0.0019	1.80	0.25	-0.005	0.73	0.77	0.92	0.85
33	0.0023	1.95	0.25	-0.005	0.62	0.69	0.83	0.83
33	0.0025	1.97	0.25	-0.005	0.64	0.71	0.85	0.83
34	0.0028	1.97	0.25	-0.005	0.72	0.80	0.92	0.84
35	0.0029	1.99	0.25	-0.005	0.72	0.81	0.93	0.85
36	0.003	2.03	0.25	-0.005	0.68	0.79	0.89	0.85
37	0.00318	2.10	0.25	-0.005	0.62	0.75	0.84	0.85

38	0.00315	2.20	0.25	-0.005	0.41	0.62	0.71	0.84
39	0.00314	2.20	0.25	-0.005	0.41	0.62	0.71	0.84
40	0.00313	2.20	0.25	-0.005	0.40	0.61	0.70	0.84

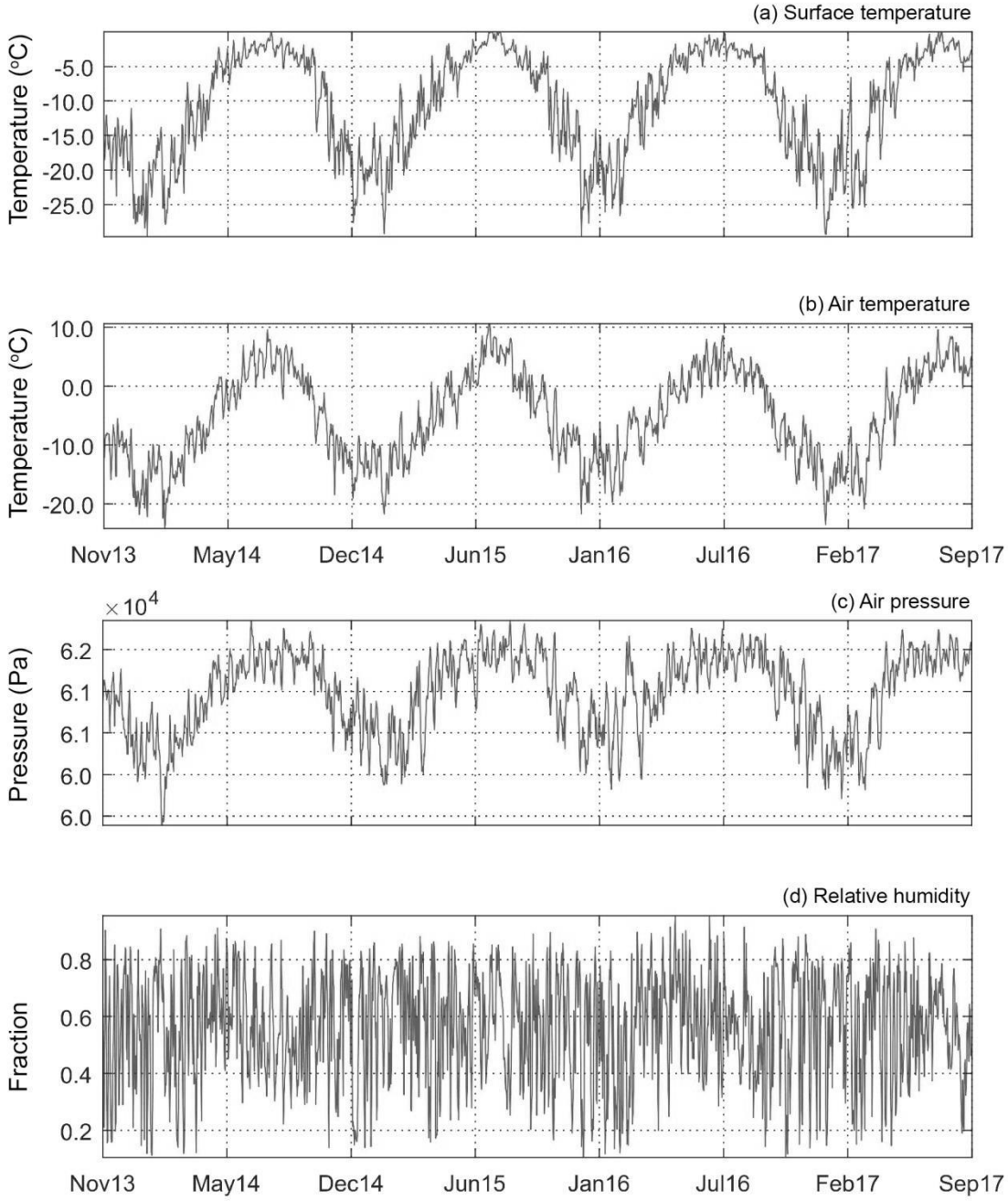
Appendix C

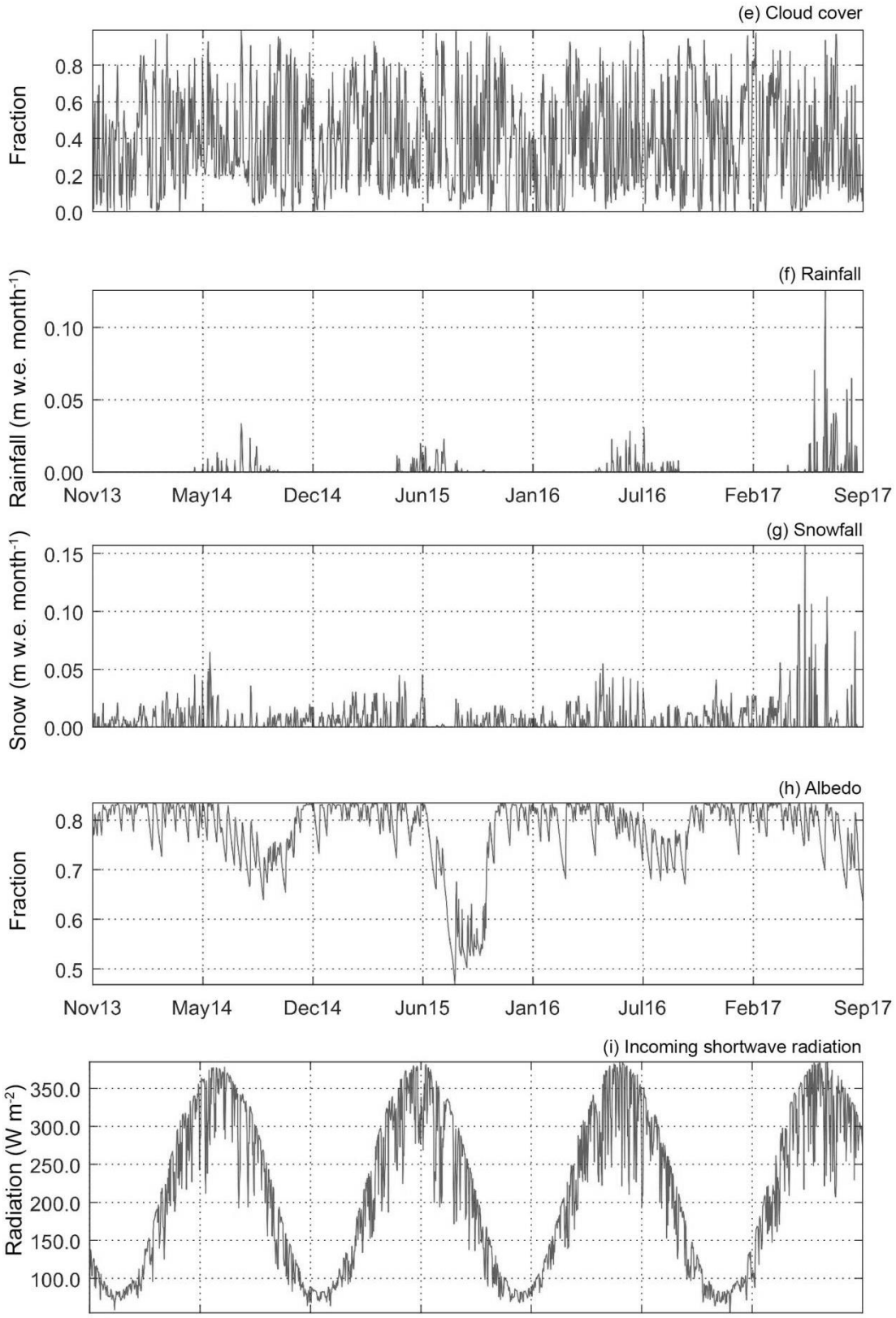
Results from the model run

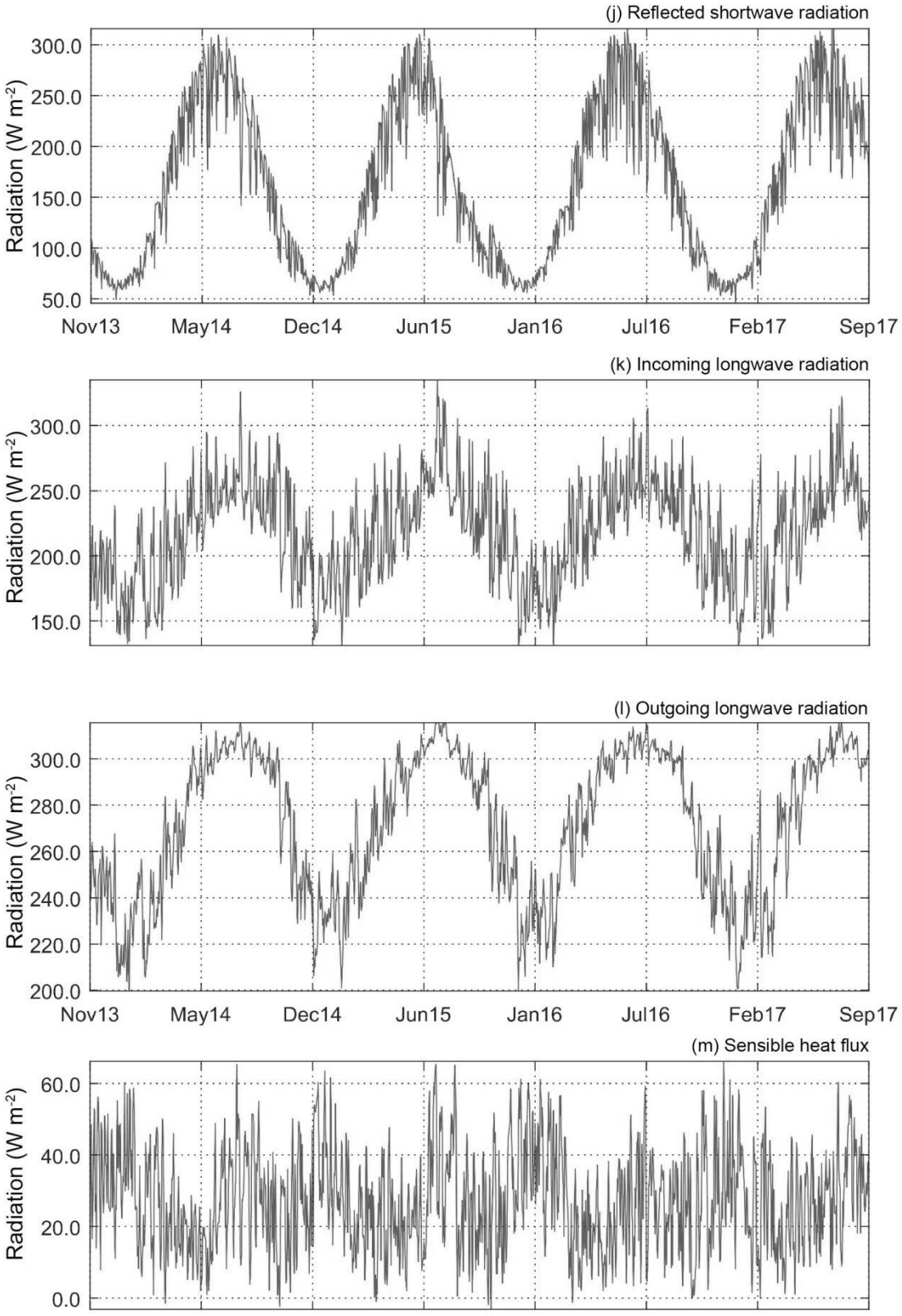
Table C1: Glacier-wide means of selected coupled model outputs for the entire period (Nov-2013 to Sep-2017), hydrological years (Oct-2014 to Sep-2017), summer, and winter.

Variable	Unit	Model mean (Nov-2013 to Sep-2017)	Hydrological mean (Oct-2014 to Sep-2017	Summer mean	Winter mean
Surface temperature	°C	-10.31	-10.11	-4.30	-15.95
Air temperature	°C	-5.05	-4.86	0.93	-10.73
Air pressure	Pa	60991.21	61017.87	61314.00	60705.35
Relative humidity	Fraction	0.56	0.57	0.57	0.56
Cloud cover	Fraction	0.39	0.39	0.37	0.41
Rainfall	m w.e. $month^{-1}$	0.041	0.047	0.081	0.0003
Snowfall	m w.e. $month^{-1}$	0.193	0.204	0.189	0.209
Melt	m w.e. $month^{-1}$	0.184	0.190	0.344	0.219
Refreezing	m w.e. $month^{-1}$	0.070	0.069	0.123	0.017
Runoff	m w.e. $month^{-1}$	0.154	0.166	0.278	0.028
Incoming shortwave radiation	W m^{-2}	211.58	209.58	296.74	123.22
Reflected shortwave radiation	W m^{-2}	-162.35	-160.00	-224.64	-97.28
Incoming longwave radiation	W m^{-2}	218.54	219.76	241.76	197.46
Outgoing longwave radiation	W m^{-2}	-272.38	-273.16	-296.81	-249.36
Sensible heat flux	W m^{-2}	27.27	27.12	25.66	28.32

Latent heat flux	W m^{-2}	-3.66	-3.56	-5.58	-1.75
Subsurface heat flux	W m^{-2}	3.85	3.83	5.51	2.13
Albedo	Fraction	0.78	0.77	0.75	0.80




(e) Cloud cover
Fraction
0.0
0.2
0.4
0.6
0.8
(f) Rainfall
Rainfall (m w.e. month-1)
0.00
0.05
0.10
(g) Snowfall
Snow (m w.e. month-1)
0.00
0.05
0.10
0.15
(h) Albedo
Fraction
0.5
0.6
0.7
0.8
Nov13
May14
Dec14
Jun15
Jan16
Jul16
Feb17
Sep17
(i) Incoming shortwave radiation
Radiation (W m-2)
100.0
150.0
200.0
250.0
300.0
350.0


(j) Reflected shortwave radiation
Radiation (W m-2)
300.0
250.0
200.0
150.0
100.0
50.0
Nov13
May14
Dec14
Jun15
Jan16
Jul16
Feb17
Sep17
(k) Incoming longwave radiation
Radiation (W m-2)
300.0
250.0
200.0
150.0
(l) Outgoing longwave radiation
Radiation (W m-2)
300.0
280.0
260.0
240.0
220.0
200.0
Nov13
May14
Dec14
Jun15
Jan16
Jul16
Feb17
Sep17
(m) Sensible heat flux
Radiation (W m-2)
60.0
40.0
20.0
0.0

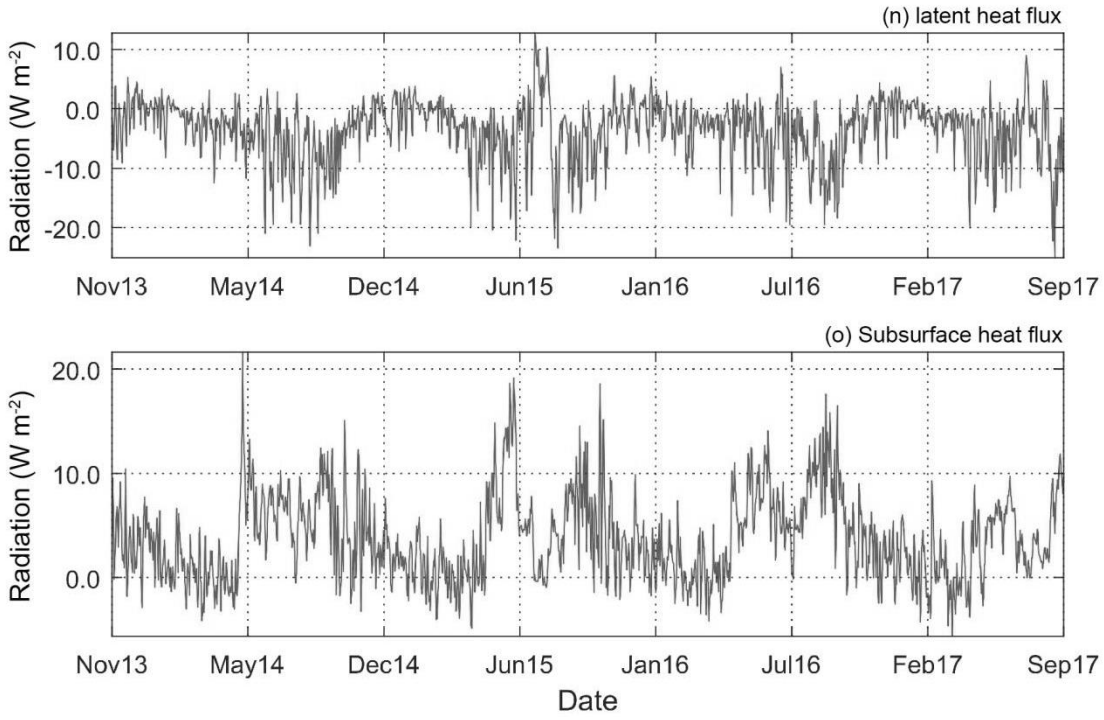
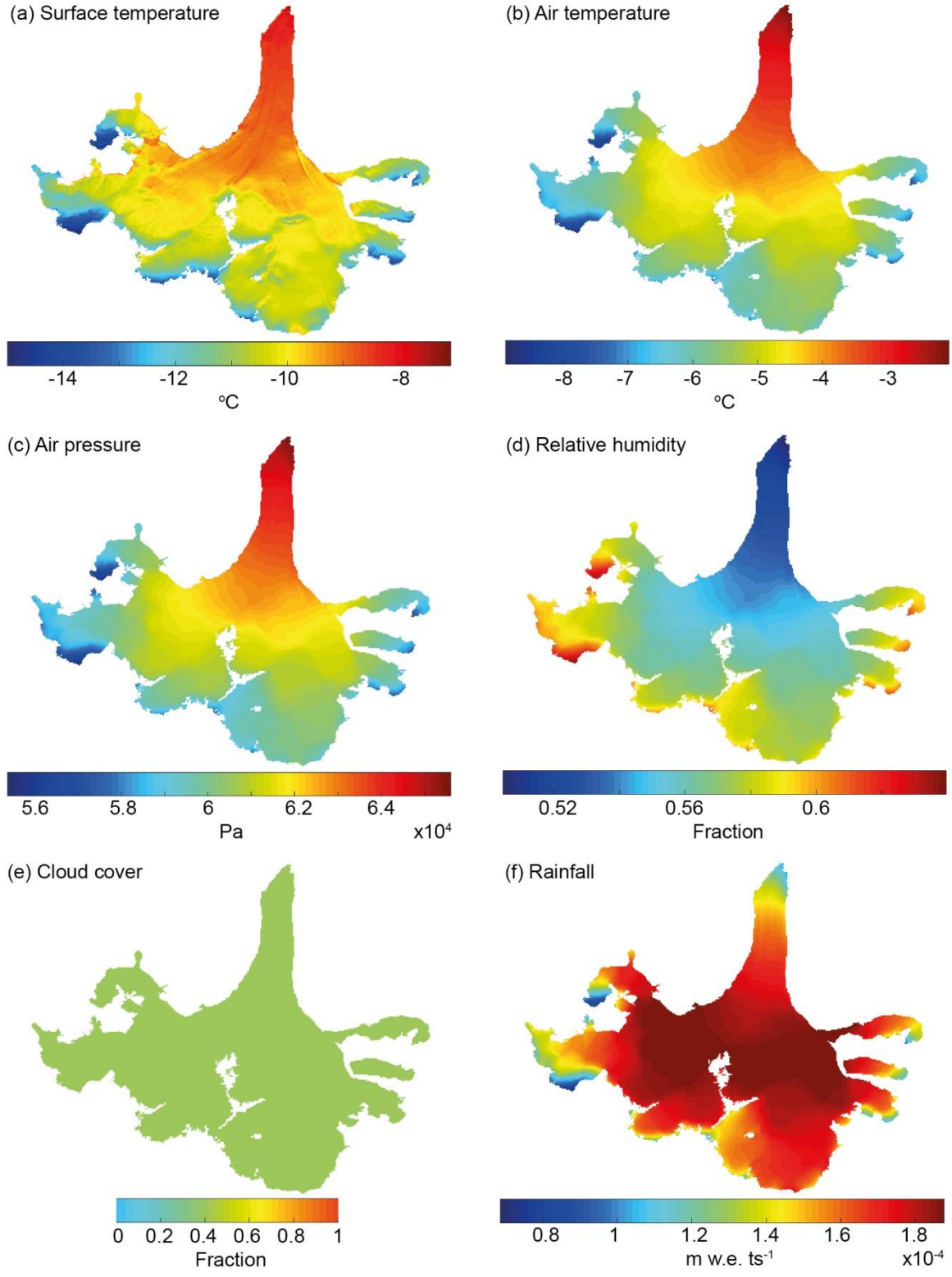


Figure C1: Time-series of glacier-wide simulated surface temperature (a), air temperature (b), air pressure (c), relative humidity (d), cloud cover (e), rainfall (f), snowfall (g), albedo (h), incoming shortwave radiation (i), reflected shortwave radiation (j), incoming longwave radiation (k), outgoing longwave radiation (l), sensible heat flux (m), latent heat flux (n), and subsurface heat flux (o) for the period 2013-2014.


(a) Surface temperature
-14
-12
-10
-8
°C
(b) Air temperature
-8
-7
-6
-5
-4
-3
°C
(c) Air pressure
5.6
5.8
6
6.2
6.4
Pa
x10⁴
(d) Relative humidity
0.52
0.56
0.6
Fraction
(e) Cloud cover
0
0.2
0.4
0.6
0.8
1
Fraction
(f) Rainfall
0.8
1
1.2
1.4
1.6
1.8
m w.e. ts⁻¹
x10⁻⁴

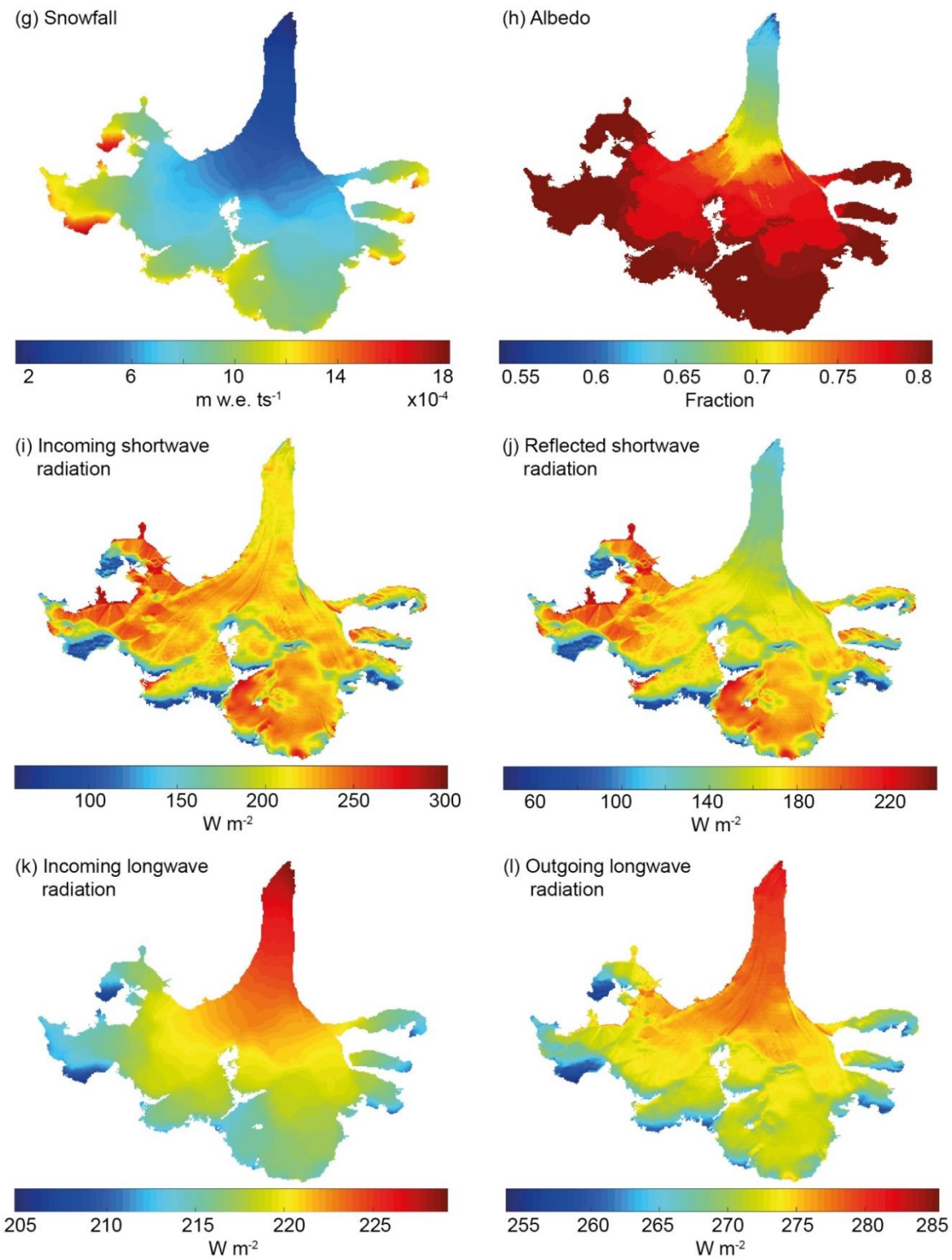


Figure C2: Spatial distribution of surface temperature (a), air temperature (b), air pressure (c), relative humidity (d), cloud cover (e), rainfall (f), snowfall (g), albedo (h), incoming shortwave radiation (i), reflected shortwave radiation (j), incoming longwave radiation (k), and outgoing longwave radiation (l) for the period 2013-2014.

Appendix D

Historical measurements for Abramov

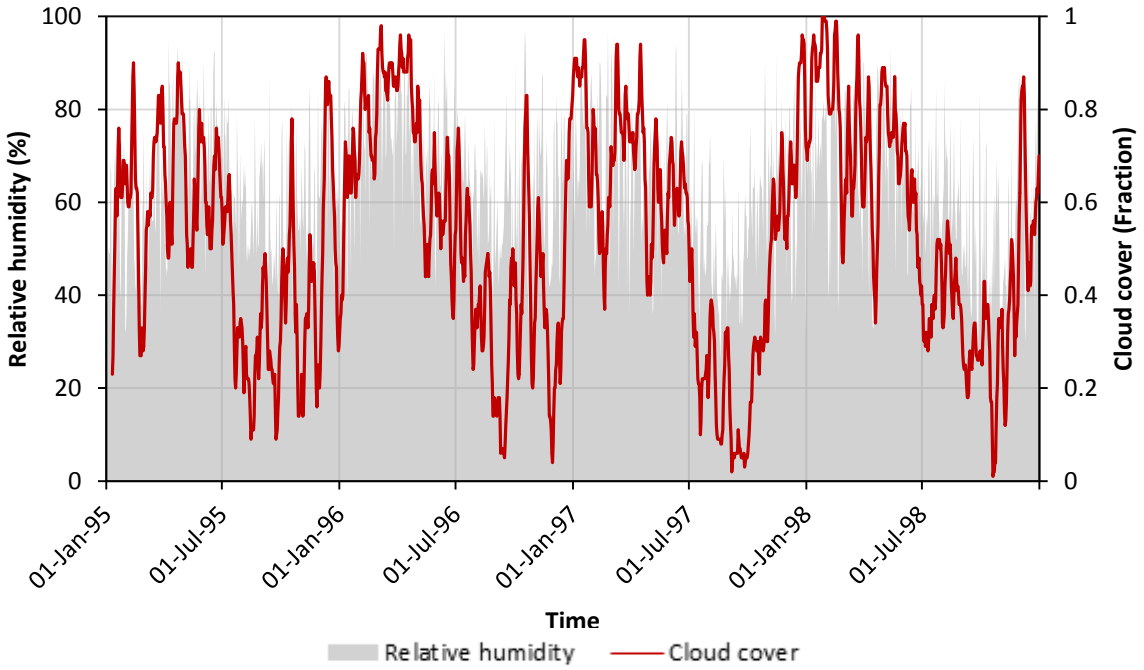


Figure D1: Time series of relative humidity and cloud cover for 1995-1998. Source: Pertziger (1996) and Pertziger (pers. comms.)